In situ diagnostics for the study of carbon nanotube growth mechanism by floating catalyst chemical vapor deposition for advanced composite applications

A DISSERTATION PRESENTED
BY
ANTHONY DICHIARA

FOR THE DEGREE OF
DOCTOR OF PHILOSOPHY

IN THE SUBJECT OF
ENGINEERING AND MATERIALS SCIENCE

ECOLE CENTRALE PARIS
PARIS, FRANCE

NOVEMBER 2012

Thesis advisors
Jinbo Bai, Laurent Zimmer

Author
Anthony Dichiara

In situ diagnostics for the study of carbon nanotube growth mechanism by floating catalyst chemical vapor deposition for advanced composite applications

Abstract

In the vast field of nanoscience and nanotechnology, carbon nanotubes (CNTs) are of particular interest because of their unique structure which provides them outstanding properties. While the number of CNT-based applications as well as the amount of CNTs produced are increasing year by year, it is essential to understand the mechanisms governing the formation of these nanomaterials to control their structure and organization, maximize the yields, reduce the health and environmental risks and improve the performance of the underlying materials and components. Among the listed synthesis techniques, the aerosol-assisted chemical vapor deposition (CVD) process developed in the laboratory MSSMat allows continuous growth of multi-walled CNTs (MWNTs) on various substrates by the simultaneous injection of carbon feedstock(s) (xylene and/or acetylene) and catalytic precursor (ferrocene) in a reactor heated up to a temperature ranging between 400 and 1000°C.

The aim of this study was to analyse the different stages of the CNT formation from the first precursor injection until the growth

termination. By the mean of a new experimental approach involving several *in situ* diagnostics coupled with numerical models, we were able to follow the evolution of the different products and reagents during the synthesis under various thermodynamic and chemical conditions.

Hence, after investigating the spatial evolution of the droplets formed in the injection, the nanoparticle germination and nucleation in the gas phase has been studied by time resolved laser-induced incandescence (TRL2I) and laser-induced breakdown spectroscopy (LIBS). A relationship between the size of the particles and the CNTs has been highlighted. Moreover, the chemical reactions during the synthesis were analyzed by mass spectrometry (MS) and gas phase chromatography (GPC). Different reaction pathways have thus been identified depending on the carbon source(s) used, while the effect of hydrogen on the CNT growth, either accelerating or inhibiting based on the CVD conditions, was studied. The substrates' roles were then examined by comparing the growth and morphology of the CNTs obtained on various surfaces such as quartz plates, carbon fibers or micro-particles of alumina, silicon carbide, titanium carbide and graphene. The catalytic effect of some substrates or mixtures of substrates on the CNT growth has also been highlighted, as well as the importance of the substrate's surface/volume ratio on the CNT mass yields. Furthermore, the CNT growth kinetics have been

studied and different mechanisms inducing catalyst deactivation and subsequently growth termination were identified. Finally, the different as-synthesized nanostructures originated from the hybridization of CNTs with other materials were used to prepare high-performance multi-functional composites. The electrical, thermal and mechanical properties of these materials have been examined.

Keywords: carbon nanotube, floating catalyst chemical vapor deposition, *in situ* diagnostics, CNT hybridization, nanoparticle, nucleation and growth mechanisms, composite materials.

Graphical abstract: CNT growth mechanism by floating CVD.

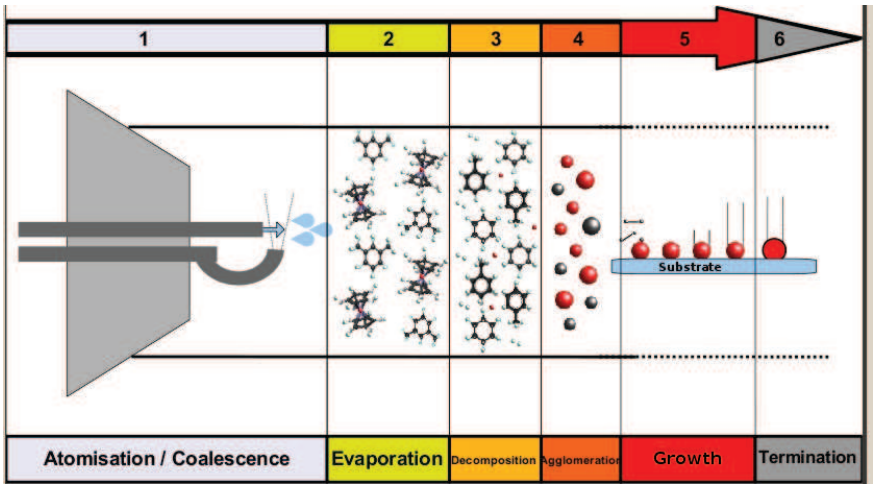

Contents

1 Introduction **1**

1.1 Carbon nanotube history 1

1.2 Carbon nanotube structure 6

1.3 Carbon nanotube applications 9

1.4 Carbon nanotube synthesis routes 21

1.5 Progress in CNT growth mechanism 29

1.6 Summary 45

2 Experimental procedure **47**

2.1 CNT growth by aerosol-assisted CVD 47

2.2 *Ex situ* characterization methods 55

2.3 *In situ* characterization methods 57

2.4 Summary 74

3 Catalyst nanoparticle nucleation **77**

3.1 The very first stage of the synthesis 78
3.2 How to control the nanoparticle size? 90
3.3 Relations with the CNT growth 94
3.4 Summary 100

4 Chemical reactions in the gas phase **101**
4.1 Modelisation and *in situ* investigations 101
4.2 Influence of hydrogen 108
4.3 Influence of carbon source(s) 111
4.4 CNT growth mechanism 114
4.5 Summary 116

5 Hidden role of the substrate **119**
5.1 The important role of the substrate 119
5.2 Synergistic effect on CNT growth 127
5.3 Summary 135

6 The CNT growth stage **137**
6.1 Evidence of a base growth mechanism 137
6.2 A pseudo *in situ* parametric study 139
6.3 CNT Growth kinetics 145
6.4 Lengthening and thickening method 158
6.5 Summary 169

7 Conclusions **173**

7.1 Summary 173

7.2 Discussion and future works 175

7.3 Last but not least 179

References **186**

Listing of figures

1.1.1 Electronic configuration of a carbon atom 2
1.1.2 Electron microscopy images of soot and carbon black . . 2
1.1.3 Schematic of the graphitic structure 3
1.1.4 Schematic of the diamond structure. 4
1.1.5 Schematic of different fullerene molecules 5
1.1.6 Electron microscopy images of carbon nanotubes 6
1.2.1 Images of SWNT and MWNT 7
1.2.2 Zigzag, armchair and chiral nanotubes 8
1.2.3 Various CNT configurations 9
1.3.1 SEM images of PVDF/CNTs-GN composites 10
1.3.2 Frequency dependence of AC conductivity 12
1.3.3 Thermal stability of different composites 14
1.3.4 Strain-stress curves of different composites 16
1.3.5 Schematic of the reinforcement dispersion in composites . 18

1.3.6 *In situ* resistance change as function of strain 20
1.3.7 Cyclic loading with resistance response 21
1.4.1 Schematic of the CNT growth by arc discharge 22
1.4.2 Schematic of the CNT growth by laser ablation 24
1.4.3 Schematic of the CNT growth by flame combustion . . . 25
1.4.4 Schematic of the CNT growth by electrolysis 26
1.4.5 Schematic of the CNT growth in a solar reactor 27
1.4.6 Schematic of the CNT growth by CVD 27
1.4.7 Schematic of the CNT growth by floating catalyst CVD. 29
1.5.1 Schematic diagram of the particle-wire-tube mechanism . 30
1.5.2 SEM image of a CNT array grown by floating CVD . . . 33
1.5.3 Schematic of the open-ended tip growth model 35
1.5.4 CNT formation from 3 different catalysts 36
1.5.5 TEM images of Ni nanoparticles 41
1.5.6 Step site on the surface of Co particle 42
1.5.7 *In situ* observations of catalyst during CNT growth . . . 44
1.5.8 Schematic of the screw dislocation-like model 44

2.1.1 Image of the spray injection system 49
2.1.2 Microscopy images of injected droplets 50
2.1.3 Droplet diameter distribution at 2 cm after the injector . 51
2.1.4 Temperature profiles along the reactor 52
2.1.5 Schematic of the CNT growth by liquid injection CVD. . 53
2.1.6 Residence time in the isothermal zone 54

2.2.1 Observations of CNT-multilayers on µ-Al_2O_3 56

2.3.1 Energy balance in a particle after heating by a laser . . . 60

2.3.2 Schematic of the overall TRLII system. 64

2.3.3 Typical *in situ* TRLII signals 66

2.3.4 Fe emission spectrum 68

2.3.5 Effect of the incident angle on LIBS 70

2.3.6 Typical *in situ* LIBS signals 71

2.3.7 Iron/carbon ratio determined by LIBS 72

2.3.8 LIBS intrusive effect on CNT growth 72

2.3.9 Typical LIBS and LII spectra 73

3.1.1 Droplet size distributions in the reactor 79

3.1.2 Different mechanisms for nanoparticle formation 80

3.1.3 CNT arrays for 0.005 g/mL of ferrocene/xylene 82

3.1.4 CNT diameter distributions with concentration 83

3.1.5 Schematic of the CVD reactor 84

3.1.6 Real-time evolution of nanoparticle size 85

3.1.7 Relation between TRLII and LIBS results 86

3.1.8 CNT diameter distribution with concentration 87

3.1.9 CNT diameter with catalyst concentration 88

3.1.10 CNT arrays for 0.005 g/mL of ferrocene/xylene 89

3.1.11 Relation between TRLII and LIBS results 90

3.2.1 Taguchi matrix design and results 92

3.2.2 Taguchi response graphs 93

3.2.3 Representative TRLII signals 95

3.3.1 Electron microscopy images and diameter distribution . . 96

3.3.2 CNT diameter as a function of particle size 97

3.3.3 Nanoparticles encapsulated inside CNT core 98

3.3.4 Carbon solubility as a function of particle size 99

4.1.1 Schematic of the numerical CVD reactor 105

4.1.2 Velocity field and 2D temperature profiles 106

4.1.3 Experimental and theoretical gas phase reactions with H_2 107

4.2.1 *In situ* mass spectrometry and gas phase chromatography 108

4.2.2 Experimental and theoretical gas phase reactions 109

4.2.3 *In situ* mass spectrometry of ferrocene at 550°C 110

4.3.1 Concentrations of C_5H_6 in the CVD gas phase 113

4.3.2 SEM images of CNTs grown from ferrocene pyrolysis . . 113

4.4.1 Concentrations of Fe atoms in the CVD gas phase 115

4.4.2 Schematic of the nanoparticle formation in floating CVD 116

5.1.1 CNT grown on quartz plate and µ-TiC 120

5.1.2 CNT growth on T700GC-12K carbon fibers 121

5.1.3 Raman spectra of GNs, CNTs and CNT-GN 122

5.1.4 SEM images of CNT-GN hybrids 124

5.1.5 SEM images of CNT-µ-Al_2O_3 and CNT-µ-SiC 125

5.1.6 Clean quartz tube after 10 min synthesis 126

5.2.1 Evolution of the CNT mass yield 129

5.2.2 Evolution of the CNT length and diameter 131

5.2.3 CNT density on µ-SiC 133

5.2.4 SEM images of CNTs on µ-Al_2O_3 and µ-SiC 134

5.2.5 Dielectric permittivity of composites 135

6.1.1 SEM images of CNT mutlilayers 139

6.1.2 CNTs grown inside µ-Al_2O_3 140

6.2.1 Pseudo-*in situ* study of the temperature 142

6.2.2 Pseudo-*in situ* study of the catalyst concentration 143

6.2.3 Raman spectra of CNTs with various Fe/C 144

6.2.4 New CNT-µ-Al_2O_3 hybrid structure 145

6.3.1 CNT growth chronology on µ-Al_2O_3 146

6.3.2 Arrhenius plot and order of reaction 148

6.3.3 Time dependent CNT growth 149

6.3.4 Schematic of the feedstock diffusion in CNT arrays . . . 150

6.3.5 Schematic of the Otswald ripening mechanism 153

6.3.6 SEM images of CNT grown on µ-Al_2O_3 155

6.3.7 Mass spectra of samples (a), (b) and (c) 156

6.3.8 Carbon encaspulated catalyst particle 158

6.3.9 Two injections lead to three CNT layers 159

6.4.1 CNT thickening by concentric graphene 161

6.4.2 CNT diameter as a function of the deposition time . . . 162

6.4.3 DTG curves of CNT arrays 163

6.4.4 Selected area electron diffraction patterns 164

6.4.5 HRTEM micrographs of thicken CNTs 164
6.4.6 Raman spectra of thicken CNTs 165
6.4.7 Number of C atoms for CNT thickening 168
6.4.8 *In situ* mass spectrometry analysis 169
6.4.9 Schematic of graphene deposition on CNTs 170

7.3.1 TEM image showing CNTs within a cell nucleus 180
7.3.2 Images of mice treated with CNTs 181
7.3.3 CNT/µ-Al_2O_3 hybrids after ultrasonication 182
7.3.4 Comparison between sea urchin and CNT/µ-Al_2O_3. . . . 183
7.3.5 Influence of the ultrasonic power on CNT/µ-Al_2O_3 . . . 184
7.3.6 CNT/shell/µ-Al_2O_3 after ultrasonication 185

Listing of Abbreviations

AFM	Atomic Force Microscopy
CNF	Carbon NanoFibers
CNT	Carbon NanoTubes
CVD	Chemical Vapor Deposition
GN	Graphene Nanosheet
GPC	Gas Phase Chromatography
HRTEM	High Resolution Transmission Electron Microscopy
LIF	Laser Induced Fluorescence
L2I	Laser Induced Incandescence
LIBS	Laser Induced Breakdown Spectroscopy
MS	Mass Spectrometry
MWNT	Multi Wall Carbon NanoTubes
NP	NanoParticle
PVDF	Poly(VinyliDene Fluoride)
TEM	Transmission Electron Microscopy
TRL2I	Time Resolved Laser Induced Incandescence
SAED	Selected Area Electron Diffraction
SEM	Scanning Electron Microscopy
SWNT	Single Wall Carbon NanoTubes

Dedicated to my wife Emma,
my mother Odile,
my father Benito,
and my brother Adrien.

Acknowledgments

There is a lot of people that I would like to thank for helping me in different ways during these three years spent at Ecole Centrale Paris. It would not have been possible to write this doctoral thesis without the support of the kind people around me, to only some of whom it is possible to give particular mention here.

First, I would like to thank my two PhD supervisors for the opportunity they gave me to work on this interesting topic: Jinbo BAI for his support, patience and advices and Laurent ZIMMER for sharing his wide scientific knowledge that has been invaluable on both an academic and personal level. I remember when we started to setup our *in situ* experiment. We purchased lasers, electronics and optics to build the first laser-based diagnostic in the lab MSSMat. We assembled the different equipments, solved the numerous issues and adapted the whole CVD reactor for the *in situ* analysis of CNT growth. It was an intense and rewarding experience.

I would like to acknowledge the financial, academic and technical support of the doctoral school of Ecole Centrale Paris (ED287) and all its staff.

I am very grateful my PhD thesis jury members, especially to the two reporters Annick LOISEAU and Pham-Huu CUONG for reviewing my dissertation. It was my honor and a great pleasure to listen to their valuable suggestions.

I am indebited to all the members of the lab MSSMat and its director, Hachmi BEN DHIA, for their kindness, availability and welcoming. I enjoyed the constructive conversations with Bertrand DAVID, Guillaume PUEL, Anne-Sophie MOURONVAL, Ann LENAIG, Sylviane BOURGEOIS and so on... I appreciated chatting with Nadege, Fleur, Farida, Martine, Sokona, Nicolas, Thomas, Francis, Daniel, Denis, Phillipe and I am also thankful for their kind help. I must add Franoise GARNIER, Paul HAGHI-ASHTIANI and Gilbert LEGAL for their precious help about SEM, TEM and all other technical issues, respectively. I spent the most of my time working in the "Nano Team" and I enjoyed it. I learned a lot working with Delong, Johan, Jinkai, Weikang, Jing and also with those who continue their carrier elsewhere like Maxime, Michael, Hassan, Jerome, Youssef, Hande, Youqin, Jing or Weilong. I wish you the best.

I have learned the process of self-reflecting, thinking, analyzing, and researching with many other people during my PhD. I would like to thank Frederique LAURENT-NEGRE, Franois DOISNEAU, Tapish AGARWAL, Theodore PROVIDAKIS from the lab EM2C and Pascale GEMEINER, Pierre-Eymeric JANOLIN and Thierry MARTIN from the lab SPMS.

I am also very grateful to the people from the Experimental Activity "Environmental Processes". It was a pleasure working with you, Arsene ISAMBERT, Mohamed RAKIB, Arnaud BUCH, Barbara MALINOWSKA, Philippe VIERS, Carole GARNIER and Helene

SANTIGNY. You helped me to develop my skills in teaching a course which I was not particularly familiar with. It gave me confidence for the rest of my teaching carrier.

Last, but by no means least, I would like to thank my dear wife Emma for her personal support and great patience at all times. My parents and brother have given me their unequivocal support throughout, as always, for which my mere expression of thanks likewise does not suffice.

There's plenty of room at the bottom

Richard Feynman

1 Introduction

1.1 Carbon nanotube history

Carbon is one of the natural element to the origin of life, both animal and vegetal. It is a very abundant element on Earth, accounting for 0.2 wt.% which corresponds to the 19^{th} most present element on Earth. Its ability to bind to other atoms (carbon or other kinds) to form chains or complex cycles makes it one of the most studied element of history. His numerous compounds have even led to the creation of a particular scientific field: the Organic Chemistry. The carbon atom is a chemical element of the acrystalliferous family possessing 6 electrons and whose molar mass is 12.0107 g.mol^{-1}. Four of its electrons belong to the Valence band as illustrated in Fig. 1.1.1.

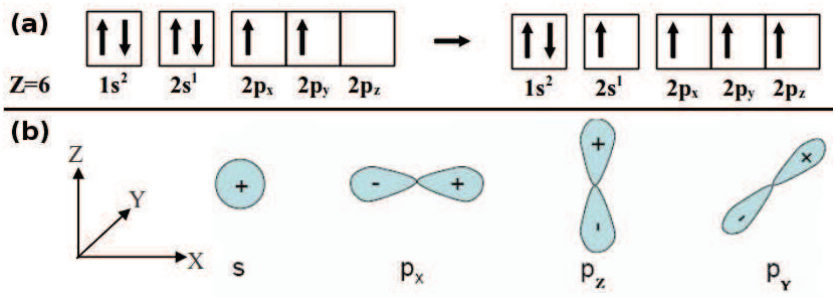

Figure 1.1.1: Electronic configuration of a carbon atom (a) and representation of its atomic orbitals (b).

Therefore, the carbon atom is tetravalent, i.e. it has four valence electrons that can potentially participate in covalent chemical bonds. These links allow the assembly of carbon atoms together. These crystalline assemblies are commonly called the allotropes of carbon. Until 1985, apart from several amorphous forms depicted in Fig. 1.1.2 (carbon black, soot, coke...) [121] [185], only two stable carbon allotropes were known: graphite, which is actually an assembly of graphene sheets stacked together, and diamond (cf. below).

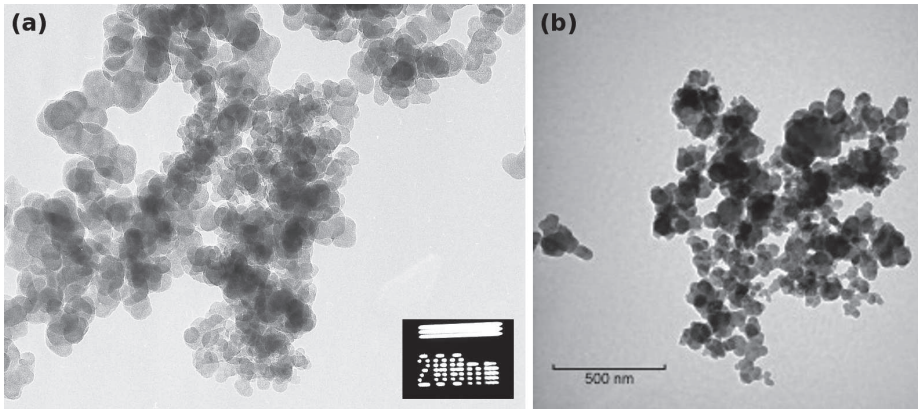

Figure 1.1.2: Electron microscopy images of soot [121] (a) and carbon black [185] (b).

The variety of allotropic forms of carbon exhibiting different physical properties can be explained by the different possible hybridization states of carbon. Indeed, in the case of the graphite structure represented Fig. 1.1.3, connections are formed between a carbon atom and its three nearest neighbors by means of the atomic orbitals 2s, $2p_x$ and $2p_y$. This arrangement involving a s orbital and two p orbitals is a sp^2 hybridization. These three orbitals are oriented on the same plane with an angle of 120°to minimize the repulsions, giving rise to a two-dimensional triangular structure allowing carbon atoms to combine their orbital hybridized with each other to form a honeycomb structure. Such a single plane is called graphene, while the stack of these planes in a hexagonal close-packed structure is called graphite. The graphene sheets are linked together by the van der Waals interactions.

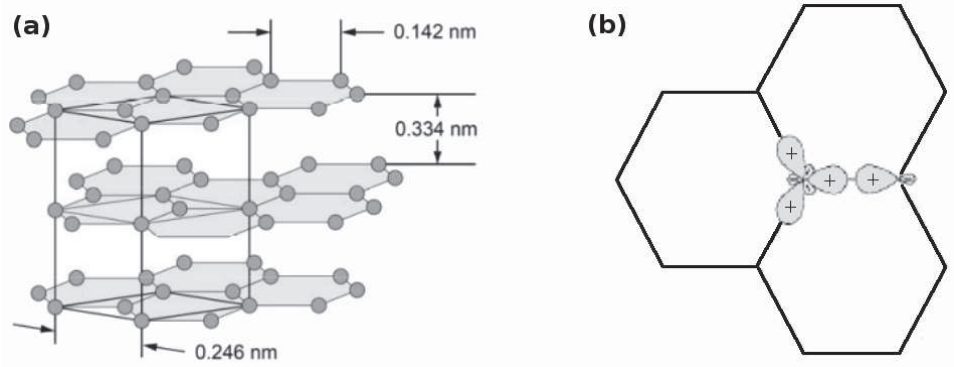

Figure 1.1.3: Schematic of the graphitic structure (a) and representation of the atomic orbitals (b).

In contrary, the carbon atoms of the diamond structure, described Fig. 1.1.4, have tetrahedral bonds with their four nearest neighbors using their orbitals s, p_x, p_y and p_z. In this case, the pooling of s orbital and three p orbitals is a sp^3 hybridization. These orbitals

are self-oriented with a 109.5°angle between each other, forming a tetragonal arrangement. Diamond is known to be the hardest material with good thermal conductivity, while graphite is brittle and has good electrical conductivity.

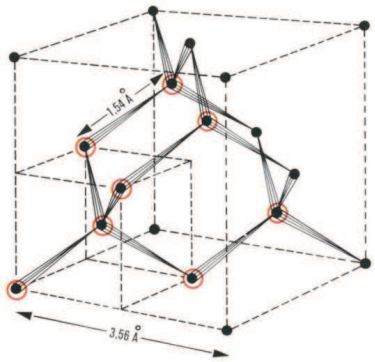

Figure 1.1.4: Schematic of the diamond structure.

In 1985, Kroto, Curl and Smalley discovered the fullerene molecules [84]. Initially, a fullerene is a molecule composed of 60 carbon atoms (C_{60}) forming pentagons, separated from each other by hexagons. The C_{60} molecule is in fact the most stable fullerenes, but other structures (C_{70}, C_{540} ...) with different shapes such as sphere, ellipsoid, ring or tube, also belong to this family (see Fig. 1.1.5).

Another metastable and low crystallizable allotrope of carbon based on sp^2 hybridization has also been discovered couple of years ago. This structure called carbyne was actually discovered in 1960 by Russian scientists at the Russian Academy of Sciences from a derivative of acetylene [48]. The carbyne consists in a linear arrangement of carbon atoms to form small molecular chains based on the combination between the 2s orbital and one 2p orbitals (either p_x or p_y or p_z).

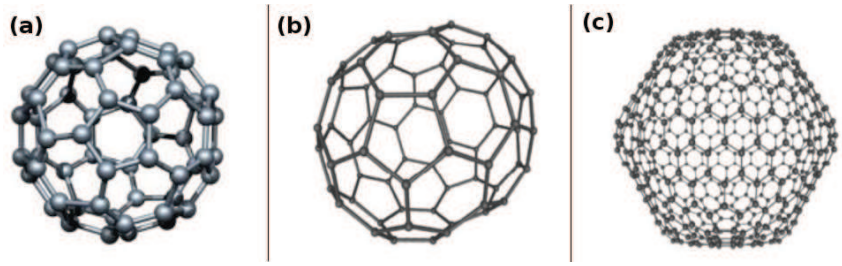

Figure 1.1.5: Schematic of different fullerene molecules: C_{60} (a), C_{70} (b) and C_{540} (c).

As announced above, carbon nanotubes are also part of the fullerene family. Their discovery is often attributed to Sumio Iijima, who identified the nanotube structure in 1991 in a by-product of the fullerene synthesis by arc discharge (see Fig. 1.1.6c) [68]. However, the nanotube story goes back few decades ago with the onset of technological advances in electron microscopy. Hence, in the 1950s, Radushkevich and Lukyanovich published images of carbon tubes about 50 nanometers in diameter (see Fig. 1.1.6a) [138]. Then in the 1970s, research on carbon fibers and their manufacture have spurred a wide interest for aerospace applications. In 1974, Morinobu Endo, a PhD student in the laboratory of Agnes Oberlin in Orleans (France) working on the synthesis of carbon fiber from benzene decomposition, identified similar tubular structures to that which will be later called "carbon nanotubes" (see Fig. 1.1.6b) [127]. It means that carbon nanotubes were actually produced and observed far before 1991. That time they were defined by the terms "hollow core" or "central tube". Finally, in 1991, Sumio Iijima published in the journal Nature [68] some transmission electron microscopy images of carbon products consisting of several concentric graphene sheets wrapped as a nano-cylinder. Therefore, such structure will be called "multiwalled carbon nanotubes" (MWNT). Two years later, in 1993, tubes formed with a

singlelayer of graphene, which will be called singlewalled nanotubes (SWNT) were synthesized simultaneously in the U.S. and in Japan by arc discharge [12] [69]. Although the first discovery of carbon nanotubes still remains an open question [119], their elaborations, characterizations and applications have always attracted the largest interest over the world as depicted by the increasing number of publications and patents in the field.

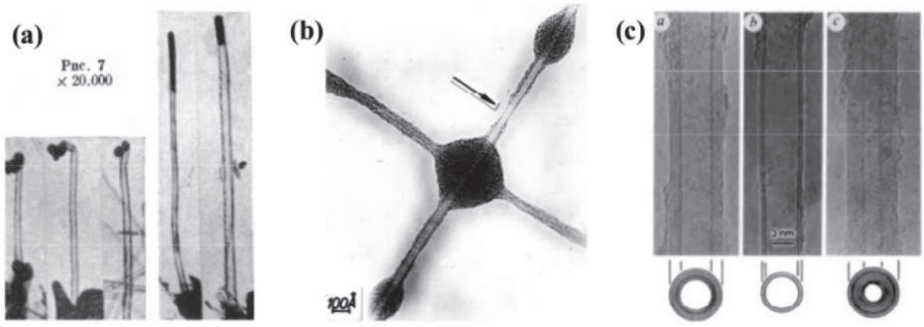

Figure 1.1.6: Electron microscopy images of carbon nanotubes observed by Radushkevich [138] (a), Endo [127] (b) and Iijima [68] (c).

1.2 Carbon nanotube structure

Another convenient way to classify the carbon allotropes previously described is in terms of their dimensions. Indeed, diamond and graphite form 3D macroscopic structures, graphene (composed of a single sheet of graphite) form a 2D structure, CNTs are examples of 1D nanostructures, while fullerenes are finally 0D systems.

The CNT structure is a winding of a graphene sheet around itself. Electron microscopy observations show that the tubes can be either open at their ends or closed by the half of a C_{60} molecule. The carbon

nanotubes can be divided into two categories (see Fig. 1.2.1): the singlewalled ones (SWNTs), consisting of the winding of a single graphene sheet (see Fig. 1.2.1a) and the multiwalled ones (MWNTs), which are formed of several concentric tubes of different diameters (see Fig. 1.2.1b).

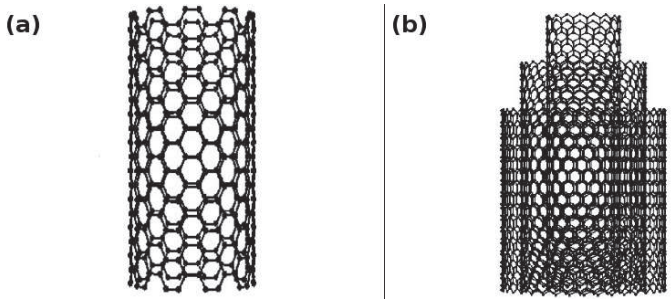

Figure 1.2.1: Images of individual singlewalled carbon nanotube (SWNT) (a) and multiwalled carbon nanotube (MWNT) (b).

.

In general, the SWNT diameter is ranging from 0.5 to 5 nm, while the MWNT diameter is larger than few nm and can reach up to several hundreds nm. For MWNTs, inter-plane distance between two layers is about 3.4 Å, which is roughly equivalent to the distance between two graphene sheets in graphite. In both case the CNT length can vary from several hundreds nm to few mm, providing a huge aspect ratio to the structure. Furthermore, the graphene sheets can wrap with an infinity of different ways, corresponding to an infinite number of angles between one edge of the sheet and a line connecting two edges, as illustrated later in Fig. 1.2.3. The geometry of a nanotube is thus determined by its diameter as well as this angle, called helicity. Regarding to the symmetry of the hexagonal lattice, the helicity is actually ranging from 0 to 30°, allowing the classification of all the possible configurations into three categories called *armchair, zigzag*

and *chiral*, as depicted in Fig. 1.2.2.

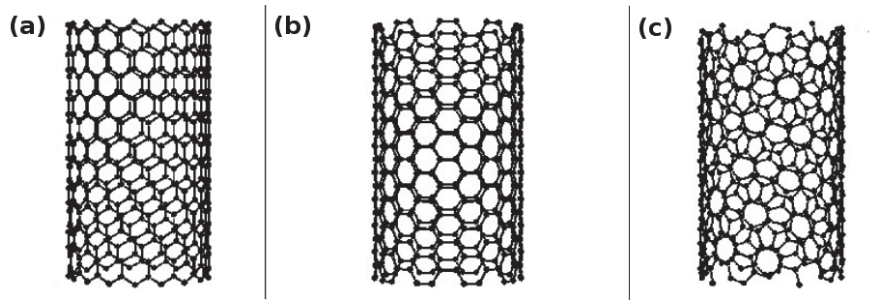

Figure 1.2.2: Images of zigzag ($\theta = 0°$) (a), armchair ($\theta = 30°$) (b) and chiral ($0° < \theta < 30°$) (c) carbon nanotubes.

The vectors $\vec{a_1}$ and $\vec{a_2}$ shown in Fig. 1.2.3 define the lattice of the graphene network. The entire network can be reconstructed by simple translations using different combinations of these two vectors. There are two atoms per unit cell. The chiral vector, $\vec{C_h}$, defined by the linear combination of the vectors $\vec{a_1}$ and $\vec{a_2}$, is orthogonal to the tube axis as indicated by the following equation

$$\vec{C_h} = n \cdot \vec{a_1} + m \cdot \vec{a_2}$$

where (n,m) are the Hamada indices. Moreover, the chiral vector is directly correlated to the nanotube radius by the following relation:

$$||\vec{C_h}|| = 2 \cdot \pi \cdot r$$

The chiral vector as well as the helicity is closely related to the winding of the graphene sheet. Therefore, by "tuning" the Hamada indices, we can change the helicity and vice versa, and thus recover the three winding categories described earlier, as depicted in Fig. 1.2.3.

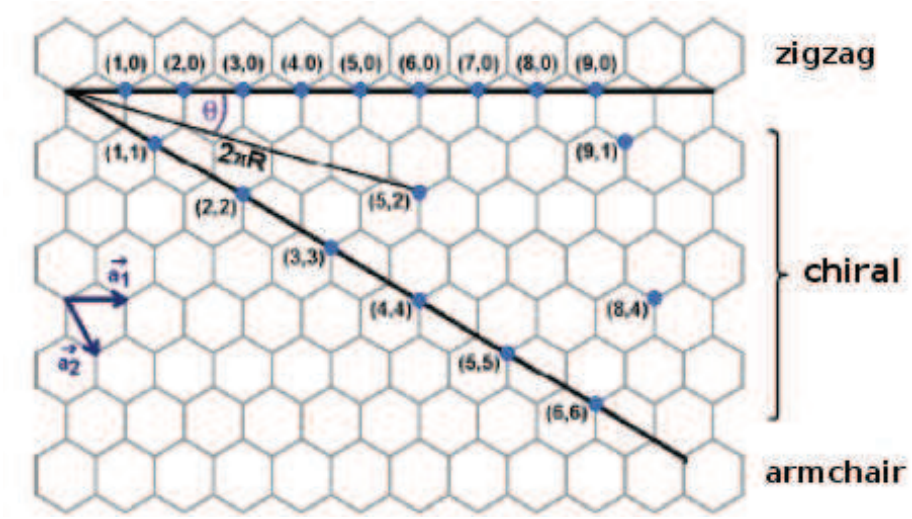

Figure 1.2.3: Various CNT configurations as a function of the Hamada indices (n,m).

1.3 Carbon nanotube applications: the example of advanced multifunctional composites

Owing to their outstanding electrical, thermal, and mechanical properties due to their unique anisotropic structures, both graphene nanosheets (GNs) and carbon nanotubes (CNTs) have been extensively studied for exploring their various applications in material science, such as energy-storage materials [43], or polymer composites [184]. However, the final dispersion state of the nanofillers (CNTs or GNs) within the matrix results from a competition between van der Waals interactions among the nanofillers and the viscous forces acting within the polymer matrix. Low viscosity facilitates dispersion during film processing but also promotes the re-agglomeration of the nanofillers. On the other hand, high viscosity will prevent re-agglomeration after casting but make processing more difficult. One way to overcome this issue would be to control the viscosity of the polymer to get an

optimized dispersion state, as suggested by Aguilar et al. [1]. Another way consists of a promising combination of the 2D GN and 1D CNT into 3D nanocarbon hybrid materials to avoid the re-agglomeration by reducing van der Waals interactions among GNs or CNTs. Such hybrid structures were incorporated into polyvinylidene fluoride (PVDF) and epoxy to prepared composites, as illustrated in Fig. 1.3.1. The electrical, thermal and mechanical properties were investigated in details by comparison with other reinforcements.

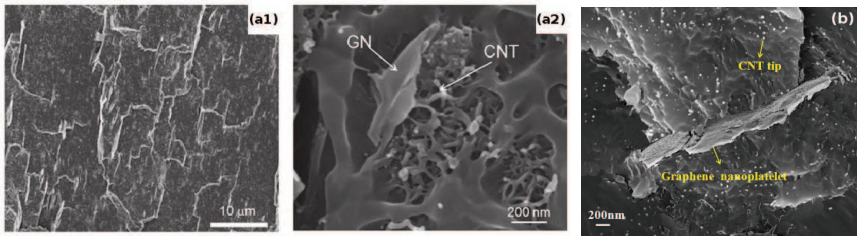

Figure 1.3.1: Cryo-fractured electron microscopy images of the PVDF composites prepared by an extrusion-casting method (a1,a2) and the epoxy composites produced by a three-roll mill technique (b) [32].

1.3.1 Electrical properties

Figure 1.3.2 presents the frequency dependence of the AC conductivity of different PVDF composites, measured at room temperature. The composites with GNs or CNTs alone do not show any obvious improvement in the conductivity relative to the PVDF matrix, especially at low frequencies. The exhibited typical dielectric behavior indicates the absence of conductive path in the composites, which may largely ascribe to the formation of filler clusters. In this case, the conductivity is mainly determined by the polarization effects and electron motion in the polymer matrix, which is highly dependent on the frequency [50]. However, with the same amount of CNT-GN

hybrids, a synergistic effect occurs and the conductivity at 0.1 Hz enhances significantly by more than 7 orders of magnitude (from $1.3 \cdot 10^{-11}$ to $1.6 \cdot 10^{-4} S \cdot m^{-1}$). In addition, the CNT-GN/PVDF composites exhibit a DC conductivity behavior in the frequency range from 10^{-1} to 10^{4} Hz, since their conductivity does not change with the frequency. Such DC characteristic in the low frequency range may be induced by few percolating paths formed through the polymer matrix. The synergistic effect on enhancing the conductivity could be well understood based on the following characteristic of this new type of CNT-GN hybrid. First, the unique structure of hybrids favors the dispersion of CNTs in polymer matrix. With the help of GN scaffold, it is much easier to disperse CNTs using traditional mixing method by avoiding re-aggregation. For instance, Fig. 1.3.1 depicts SEM micrographs of cryo-fractured surfaces of CNT-GN/PVDF composites with 6.6 wt.% hybrids. It can be observed that the hybrids can be evenly dispersed in the polymer matrix, as indicated by the GN edges (bright lines) shown in the low-magnification SEM image (see Fig. 1.3.1a). The GNs are prone to be arranged as parallel plates, which is possibly induced by the shear flow during the melt-extrusion. The 3D hybrid structures are well retained in the polymer matrix after being blended with PVDF, which can be confirmed by a high-magnification image (see Fig. 1.3.1b). The CNTs perpendicular to the surface of GNs could potentially create electrical connections between the parallel neighboring GN platelets, thus give rise to a more effective conductive network. Second, CNTs on the GNs could effectively prevent the restacking of GNs and improve effective interface in composites, providing numerous tunneling sites for electron transport. Third, vertically aligned state of CNTs may serve as bridges to connect neighboring GNs, which is much favorable to form conductive networks and hence largely enhance the conductivity of the composites. To verify the synergistic effect above mentioned, a CNT and GN mixture

with the same CNT/GN mass ratio with hybrids is incorporated into PVDF matrix. Though the mechanically mixed filler could induce about 1 order of magnitude increase in conductivity in the whole frequency range, the resultant composite still exhibits an insulating rather than conductive nature. The mixed GN and CNT fillers fail to form a 3D conductive networking due to the lack of effective linkage to one another at the examined filler content. Therefore, the unique 3D architecture of the CNT-GN hybrid is much reasonable to be invoked as being responsible for the significant synergistic effect between GN and CNT on reinforcing the conductivity of the polymer composites.

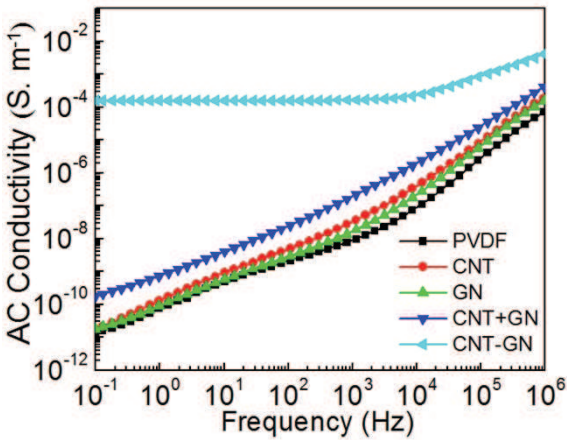

Figure 1.3.2: The frequency dependence of AC conductivity of PVDF matrix and its different composites with 6.6 wt% fillers (CNT-GN hybrid, CNT+GN mixture, GNs and CNTs) [32].

1.3.2 Thermal stability

Figure 1.3.3a illustrates TGA curves, showing that the addition of various fillers decreases the onset temperature for mass loss upon heating. The mass loss is due to the decomposition of the PVDF

matrix. The decomposition starting temperatures of different composites reinforced with 1D (i.e. CNTs), 2D (i.e. GNs) and 3D (i.e. CNT-GN hybrids) fillers can be obtained from the intersection of the tangents of each curve. The thermal stability of the neat PVDF (464°C) decreases with the addition of GNs (413°C), while it slightly increases when a similar content of CNTs are filled in the polymer matrix (467°C). The addition of CNT-GN hybrids or mixtures show balanced decomposition starting temperatures of 449°C and 439°C, respectively, which are between the composites reinforced by GNs and the ones reinforced by CNTs. It should be emphasized that the remnant catalyst particles in the CVD grown CNTs may hasten the polymer decomposition, so the composites thermal stability can be further improved by the use of purified fillers. Figure 1.3.3b shows that the melting temperature would be not significantly affected by the filler structure. Indeed, the melting temperatures of the different composites and the neat PVDF matrix vary from 169 to 172°C. This may indicate that the crystal size, which is expected to be influenced by the fillers' surface area, is actually independent of the reinforcement structures used. No other melting peaks can be identified, suggesting the absence of transcrystalline layers between the fillers and the matrix, observed by Xu et al. [178]. Moreover, the enthalpy of melting for all reinforced composites decreases compared to the pure polymer, which is evidenced by the decreased DSC peak areas with the addition of the different fillers. This may suggest that the addition of fillers reduces the degree of crystallinity. Therefore, the lower enthalpy values for the composites should be the result of the competition between the nucleating effect and restricting effect of the fillers on PVDF. Similar phenomenon has been reported for different polymer matrix composites filled with inorganic fillers such as clay [164] and metal particles [18]. Although the nucleating effect of the carbon-based fillers can lead to a higher crystallinity in PVDF matrix, the presence

of these fillers can restrict the motion of PVDF molecular chains. The nucleus generated on the filler surfaces grow under the restricting condition, which will lead to imperfect crystals and defects and thus reduce the composite thermal stability.

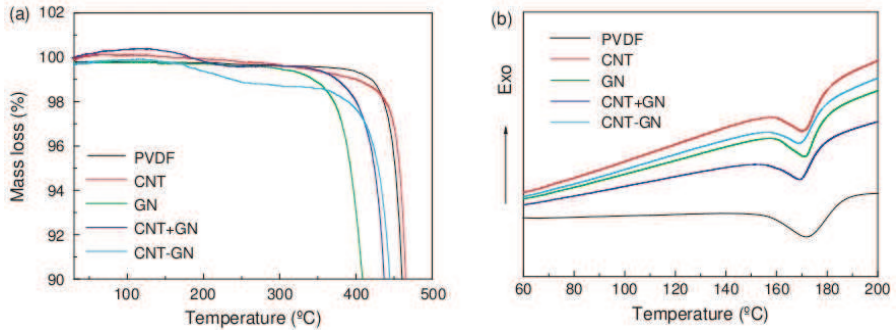

Figure 1.3.3: The (a) TGA and (b) DSC curves of PVDF and its different composites with 6.6 wt% fillers (CNT-GN hybrid, CNT+GN mixture, GNs and CNTs) [32].

1.3.3 Mechanical properties

Figure 1.3.4 illustrates the typical stress-strain response of the epoxy composites with the same concentration (0.5 wt.%) of CNTs, GNs, CNT+GN mixture and CNT-GN hybrids under quasi-static tensile loading. Introducing a small amount of fillers, the mechanical behavior of the composites apparently shows an enhancing trend compared to that of baseline epoxy. The elastic modulus and ultimate tensile strength (UTS) of the composite based on CNT-GN hybrids are dramatically increased compared to that of the composites with the other fillers. The experimental results of the tensile properties of baseline epoxy and the composites are summarized in Fig. 1.3.4b-d. The tensile modulus of the CNT-GN/epoxy composite is up to 3 GPa and shows 40 % increase compared to that of the pristine epoxy.

However, there are very moderate enhancements of the tensile modulus in the CNTs/epoxy (8 %), GNs/epoxy (5 %) and CNT+GN/epoxy (14 %) composites. The variation tendency of the tensile strength in the composites is similar to that of tensile modulus. The tensile strength of the CNT-GN/epoxy composite also acquires significant enhancement (+36 %) compared to other kinds of composites. The lower improvement of the tensile modulus and strength in the epoxy composites with CNTs, GNs or CNT+GN may be attributed to the waviness of pristine CNTs and the stacking behavior of the GNs (see schematics Fig. 1.3.5) arising from their large aspect ratio and van der Waals force. Moreover, the slippage of the overlapped GNs is also considered to appear during tensile loading. It is well known that a high degree of load transfer from the reinforcement to the matrix is an important issue for the improvement of elastic modulus and strength. Nevertheless, the factors above may restrain the stress transfer and thus the reinforcement efficiency will be limited. Besides the tensile modulus and strength, the fracture strain of the baseline epoxy and composites is shown in Fig. 1.3.4d. Unlike the composites based on CNTs, GNs or CNT+GN mixture, the fracture strain of CNT-GN/epoxy composites is almost the same as that of neat epoxy. In case of poor dispersion of the fillers, the formation of nano or micro flaws results in local stress concentration in the matrix. The brittleness and ultimate failure of the composites is probably caused by those voids and defects resulted from the agglomeration of the GNs and CNTs. On the basis of the experimental results and analysis mentioned above, we infer that CNT-GN/epoxy composite demonstrates better stiffness as well as toughness than the other kinds of composites.

Because the reinforcement effect is a complex issue involving load transfer, stress concentration and defect distribution, some

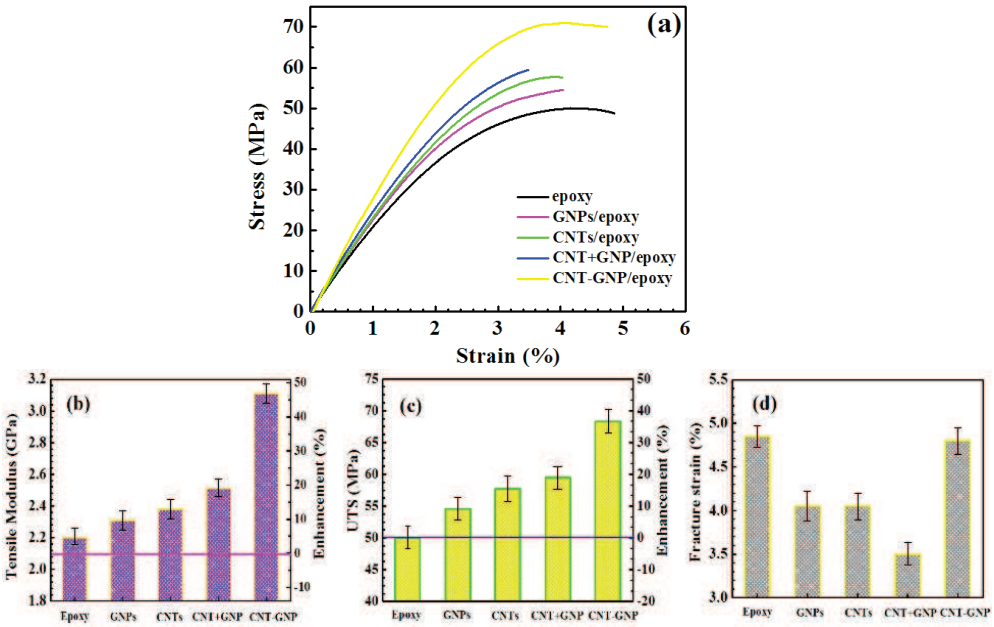

Figure 1.3.4: Tensile properties of baseline epoxy and the epoxy composites with 0.5 wt.% reinforcements (a) Typical strain-stress curves; (b) Tensile modulus; (c) Tensile strength; (d) Fracture strain.

explanations concerning CNT-GN hybrids with unique architecture is proposed to reveal their underlying reinforcing mechanism. First, the perfectly dispersed CNTs grown on GNs could not only form highly uniform networks of CNTs but also inhibit the stacking and aggregation of GNs (see Fig. 1.3.5). This three-dimensional hybrid structure leads to large surface contact and strong molecular coupling between the CNTs and the epoxy matrix. It is possible that an excellent interfacial interaction between CNT networks and surrounding polymer matrix plays an important role on the effective stress transfer in the composites. Furthermore, the aligned CNTs can be viewed to retain in the matrix at their actual lengths instead of curly state for optimizing their reinforcement efficiency. Second, the uniform dispersion of the CNTs and GNs does not lead to the formation of

flaws, which is important for stress transfer between the reinforcements and the matrix. Third, the orientation of the CNT grown on GNs are much more difficult than the randomly orientated CNTs under low strain because of their stable junctions with graphene substrate and excellent molecular coupling with polymer chains, which can give a good explanation to the higher elastic modulus in the composites based on such architecture. It is generally accepted that CNT orientation is a key parameter for the mechanical properties of the composites. The rotation of graphene substrate and the orientation of aligned CNT bundles gradually appear with the increase of strain, which potentially leads to the rearrangement of the CNT networks. This rearrangement behavior may inhibit the rapid growth of the emerging microcracks and some mechanical energy could be dissipated during this rearrangement process. Furthermore, it probably weakens the stress concentrations to a certain extent. All of these factors may account for the increase of toughness and fracture strain in the CNT-GN/epoxy composites.

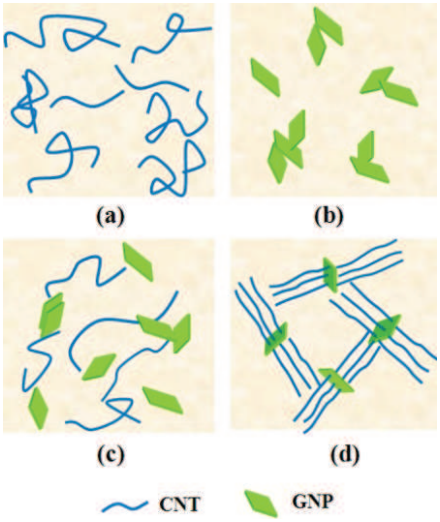

Figure 1.3.5: Schematic images of reinforcement dispersion in the epoxy composites (a) CNTs; (b) GNs; (c) CNT+GN mixture; (d) CNT-GN hybrids [96].

1.3.4 *In situ* SELF-SENSING ABILITIES

With their superior mechanical and electrical properties, carbon nanotubes (CNTs) can serve as not only the structural reinforcement but also the excellent *in situ* sensor in structural composites [95]. In this field, most previous research realized *in situ* monitoring by using electrically conductive networks of randomly orientated CNTs. When subjected to tensile stress, electrical resistance of the composites usually increased monotonically until the catastrophic failure [132]. However, it is still a challenge to identify elastic and plastic deformation of the composites via in situ electrical resistance measurement. On the other hand, it is imperative to realize this end in practical applications, because the service life and operational safety of composites can be largely extended by limiting the applied stress within the elastic region.

The resistance response of the CNT-GN/epoxy composite is tracked

in real-time when the specimens are subjected to quasi-static and incremental cyclic tensile loading. Figure 1.3.6 presents the stressstrain curve as well as the *in situ* electrical resistance change in the composite during tensile loading. The resistance monotonically increases and then begins to decrease when the strain reaches a critical value, which obviously divides the chart into two regions. In the elastic region, the elastic deformation makes the number of contact points between CNTs on different GN microplatelets decrease (see Fig. 1.3.6). As a result, the *in situ* electrical resistance increases in this region. When the plastic deformation occurs, there is reformation of the conductive networks after their break-ups, which can be explained by the electrical tunneling resulted from the closing of the µ-cracks because of Poissons contraction [81]. Besides the electrical tunneling effect, the intense movement of the polymer chain may induce the rotation of some CNT bundles grown on GNs along the stress direction. Such reorientations could reform the conductive networks in the plastic region (see Fig. 1.3.6), explaining the decrease of the electrical resistance in the plastic region.

Figure 1.3.7a shows an example of the transient stress, strain and resistance response as function of time under cyclic tensile loading. During the first three loading and unloading cycles, the transient resistance change closely followed by the response of applied stress and strain. The electrical resistance increases and decreases monotonically with the cyclic stress and strain, because the elastic deformation induces the break-up and intact reformation of the conductive network with the open and closing of microcrack during tensile loading [163]. However, slight deviation of the resistance to the strain response could be observed during the fourth cycle. Upon unloading after the fourth cycle, one can see that there is permanent resistance change with the

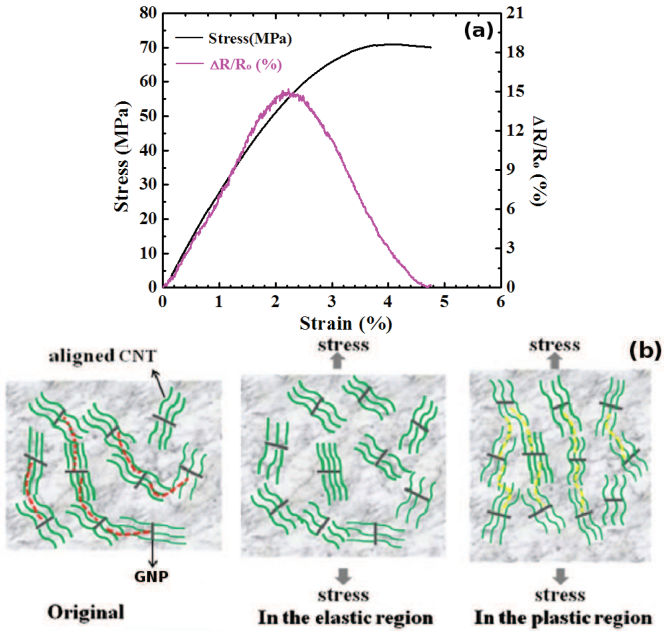

Figure 1.3.6: *In situ* resistance change and the corresponding stress as function of strain for the epoxy composite with CNT-GN hybrids under quasi-static loading (a). Schematics of the evolution of the conductive networks (b) [96].

emergence of residual strain. The permanent resistance change implies the presence of irreversible plastic deformation with accumulation of microcracking in the matrix during this cycle. Subsequent cycle shows the evident deviation of the resistance from the strain curve as well as larger permanent resistance change and residual strain. Moreover, it is found that the peak of the resistance change begins to decrease after the fourth cycle. Fig. 1.3.7b illustrates the stress and resistance response of one specimen over time undergoing cyclic loading with a progressively increasing step load. In the first fifth cycles, there is larger resistance change in the latter cycle as compared to the previous cycle upon re-loading and the resistance change is relatively stable in each cycle. The formation of new microcracks may be mainly responsible for the resistance increase in the following cycles [49]. Nevertheless,

the resistance change begins to decrease and becomes unstable from the sixth re-loading cycle. Moreover, the permanent resistance change appears in the unloaded state after the sixth cycle. Consequently, from these results it could be concluded that the specimen experiences an elastic deformation during the first fifth cycle and irreversible plastic deformation or permanent damage is initiated from the sixth cycle. The decrease of resistance change is attributed to the reformation of new conductive network induced by the continuous alignment of some flexible cross-linked chains of epoxy matrix in the plastic region.

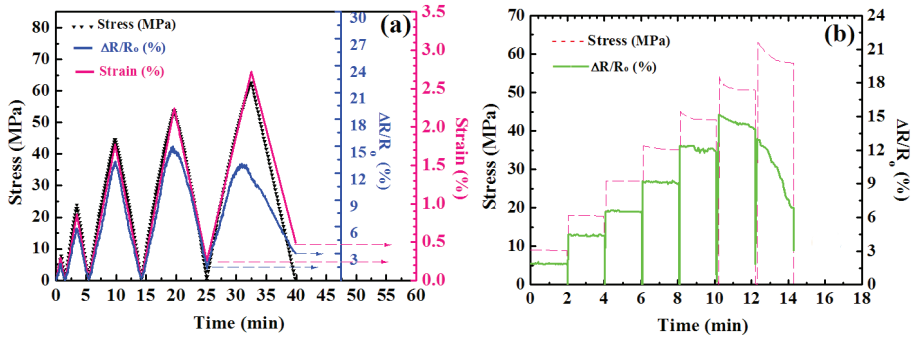

Figure 1.3.7: Cyclic loading with transient stress, strain, and resistance response as a function of time (a). Incremental cyclic loading and the corresponding resistance change for the CNT-GN/epoxy composites (b) [96].

1.4 Carbon nanotube synthesis routes

1.4.1 Arc discharge

The first highly cristalline structures recognized as CNTs were produced in bulk by the arc discharge technique usually employed for fullerene production, as reported by Iijima [68]. This process involves the passage of a direct current of about 100 A, driven by

a potential difference of approximately 20 V, through two carbon electrodes separated by about 1 mm under inert atmosphere at low pressure. A schematic representation of the apparatus is depicted in Fig. 1.4.1. The discharge vaporizes the surface of one of the electrodes, and forms a small deposit on the other one. While high purity graphite electrodes are required to synthesize MWNTs, electrodes containing metal catalysts (such as cobalt, iron or nickel) mixed to graphite powder result in a deposit containing SWNTs [69]. Producing CNTs in high yield depends on the uniformity of the plasma arc, and the temperature of the deposit forming on the carbon electrode. However, this technique produces a complex mixture of components, and requires further purification to separate the CNTs from the soot and the residual catalytic metals present in the crude product.

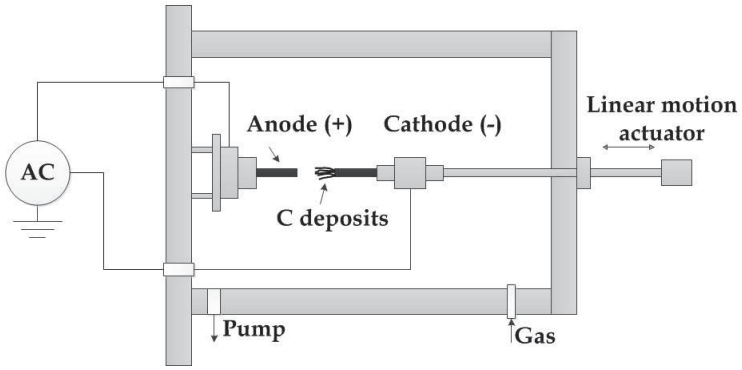

Figure 1.4.1: Schematic of the CNT growth by arc discharge [112].

Based on the general principle illustrated in Fig. 1.4.1, various types of arc discharges methods were developped. For instance, Imasaka et al. [70] reported on the intermittent arc discharge process in water producing carbon nano-onions and nanotubes. This technique permits several millisecond pulse duration which is much longer than that of typical pulsed arc method with microsecond pulse duration. The

products obtained were either a floating powder containing uniformly dispersed fine spherical particles, or a sediment composed of straight MWNTs with length in the range of 100-500 nm. Another example was reported by Lee et al. [92] who synthesized CNTs by plasma rotating arc discharge. They observed that the CNT yield was increased as the rotation speed of the anode was increased and the collector became closer to the plasma.

1.4.2 Laser ablation

Another method to grow CNTs using laser ablation was demonstrated in 1995 by Smalley's group and has prompted a lot of interest [54]. The synthesis can be carried out in a horizontal flow tube under a flow of inert gas at controlled pressure, as illustrated in Fig. 1.4.2. In this set-up the flow tube is heated to 1200°C by a tube furnace. Laser pulses enter the tube and strike a target consisting of a mixture of graphite and a metal catalyst. The initial laser vaporization pulse was followed by a second pulse, to vaporize the target more uniformly. The use of two successive laser pulses minimizes the amount of carbon deposited as soot. The second laser pulse breaks up the larger particles ablated by the first one, and feeds them into the growing nanotube structure. Then, the CNTs condense from the laser vaporization plume and are deposited on a collector outside the furnace in the cooling zone. By tuning the growth temperature, the catalyst composition, and other process parameters, the average nanotube diameter and size distribution can be varied.

Arc-discharge and laser vaporization are currently the principal methods for obtaining small quantities of high quality CNTs. However, both methods suffer from drawbacks. The first is that both methods

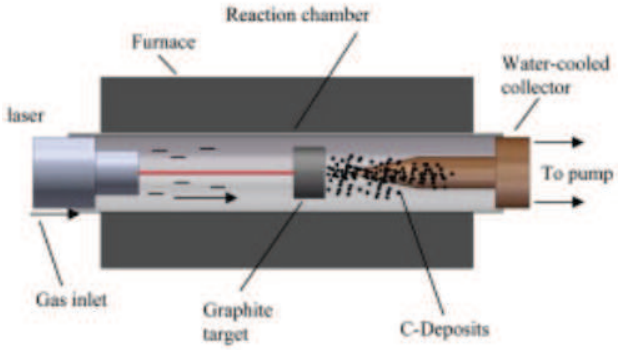

Figure 1.4.2: Schematic of the CNT growth by laser ablation [112].

involve evaporating the carbon source, so it has been unclear how to scale up production to the industrial level using these approaches. The second issue relates to the fact that vaporization methods grow CNTs in highly tangled forms, mixed with unwanted forms of carbon and/or metal species. The CNTs thus produced are difficult to manipulate and assemble for building nano-device architectures for practical applications. They require the use of complex sorting techniques that can damage the tubes.

1.4.3 Other methods

CNTs can also be produced by other less common methods like diffusion flame synthesis, electrolysis, use of solar energy, heat treatment of a polymer, or low-temperature solid pyrolysis.

In flame synthesis [167], combustion of a portion of the hydrocarbon gas (e.g. acetylene or benzene) provides the elevated temperature needed, with the remaining fuel conveniently serving as the required hydrocarbon reagent (see Fig. 1.4.3). Hence the flame constitutes an efficient source of both energy and hydrocarbon raw material.

Combustion synthesis has been shown to be scalable for high-volume commercial production [168]. Nevertheless, considering the lack of control over the CNT self-assembly location and the relatively high temperatures involved, this process is not suitable for all CNT applications, such as the CNT-based electronic devices which are believed to be one of the next major advances in the IT industry.

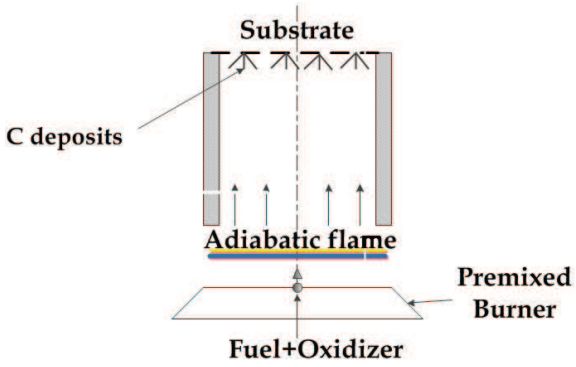

Figure 1.4.3: Schematic of the CNT growth by flame combustion [167].

The CNT synthesis by electrolysis was developed by Hsu et al. [66] in 1996. The CNTs are formed when a current is passed through two graphite electrodes immersed into molten ionic salts at temperature about 600°C, as detailled in Fig. 1.4.4. After electrolysis, the carbonaceous material is extracted by dissolving the ionic salt into distilled water. The dispersion is then separated by filtration. The as-produced material contains CNTs, carbon-encapsulated metal particles from the salt ions, amorphous carbon and carbon filaments. So far, only the generation of MWNTs has been reported, while the formation of SWNTs via electrolysis has not been observed yet. However, this route is very low cost and further studies are ongoing.

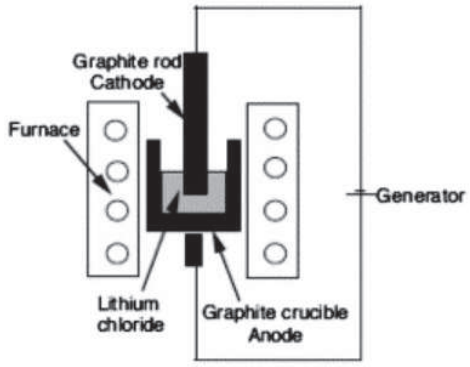

Figure 1.4.4: Schematic of the CNT growth by electrolysis [66].

Similarly as the arc discharge and the laser ablation techniques, the CNT growth in a solar reactor involves the vaporization-condensation of carbon in low-pressure inert gas atmosphere. The diffence arises from the way used to induce carbon vaporization, as shown in Fig. 1.4.5. The vaporization of carbon performed in highly concentrated sunlight has been successfully reported since 1993 for the production of fullerenes and carbon nanotubes with a 2-kW vertical solar furnace at the Odeillo Institute [90]. The solar route presents substantial advantages: (i) the target can be an insulator that allows the use of powdered mixture; (ii) the synthesis parameters (pressure, temperature, gas flow rate) can be chosen independently; and (iii) the possibility of scaling-up the reactor up to 1-MW. However, further efforts are needed to allow a good monitoring of the final CNT structures.

1.4.4 Chemical vapor deposition

Chemical Vapor Deposition (CVD) is a generic name for a group of processes that involve the deposition of solid material by chemical reactions between a gaseous precursor and a substrate. In com-

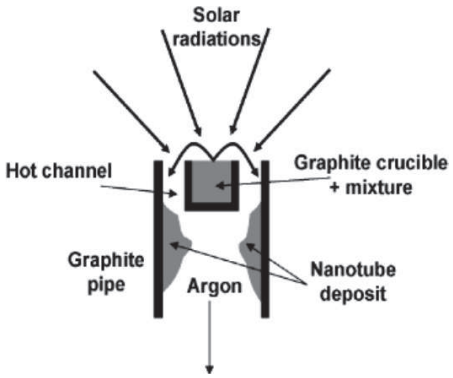

Figure 1.4.5: Schematic of the CNT growth in the solar reactor in Odeillo (France) [90].

parison with arc discharge and laser ablation, CVD is a promising method due to its upward scalability, low cost, high yield and rather low production temperature. Generally, in a CVD process, the substrate is maintained at temperature ranging between 400 and 1200°C and is exposed to the volatile precursor(s) carried by inert gases, such as nitrogen, helium or argon, as depicted in Fig. 1.4.6.

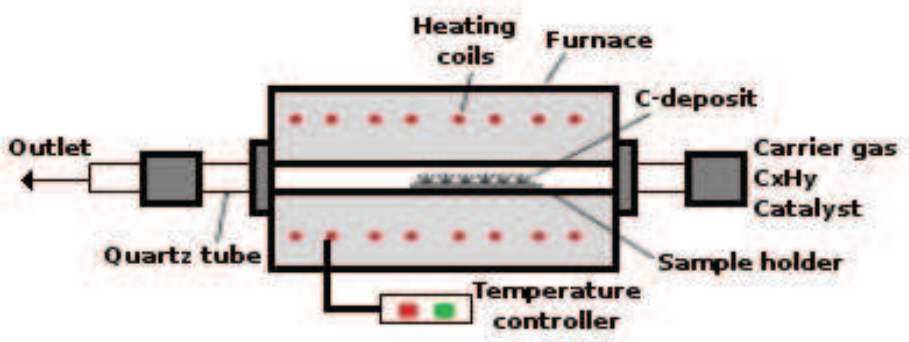

Figure 1.4.6: Schematic of the CNT growth by chemical vapor deposition [112].

For CNT growth, the CVD process consists of the pyrolysis of

hydrocarbons (e.g. methane, benzene, acetylene...) usually catalyzed by various nanoparticules (NPs). A general CVD process can be divided into four fundamental steps: (i) catalytic or pyrolytic dissociation of hydrocarbon on the catalyst surface or in the gas phase to release reactive carbonaceous species, (ii) diffusion of these reactive species on/into the catalyst, (iii) nucleation of the graphitic nuclei on the catalyst surface via intermediate phases, and (iv) further incorporation of carbon into the growing graphitic structure to elongate the tube. This is a general principle which can arise to various processes depending on how the precursors are introduced and decomposed into the reactor. For instance, to increase the precursor gas decomposition during the synthesis, the CVD process can be assisted by a plamsa. In this case, the technique is referred as plasma-assisted CVD. Another example is the water-assisted CVD, which allows rapid CNT growth for the production of high-quality, impurity-free, millimeter-long, single-walled (SWNTs) and/or multi-walled (MWNTs) CNTs [58] [59] [179]. Nevertheless, nowadays the amount of CNTs grown are typically as small as few tens of $g.m^{-2}$, which remains the major obstacle for industrial applications. One promising approach for CNT mass production consists of the floating catalyst CVD processes where flat substrates would be substituted with supports with larger surface areas, like beads [79]. While, premature termination of growth, presumably because of catalyst deactivation, is an undesirable side effect of the so-called and widely used supported catalyst CVD techniques, in a typical floating catalyst CVD process, catalyst precursors along with carbon feedstock(s) are simultaneously introduced into the reaction chamber, allowing higher yields, lower costs and continuous production abilities [27]. A general scheme of a floating catalyst CVD process is presented in Fig. 1.4.7. Although CNTs are produced in increasingly larger quantities there is still a lack of precise control over the growth process to obtain large

amount of CNTs with well-defined structures and properties. A thorough understanding of the CNT growth mechanism is therefore needed.

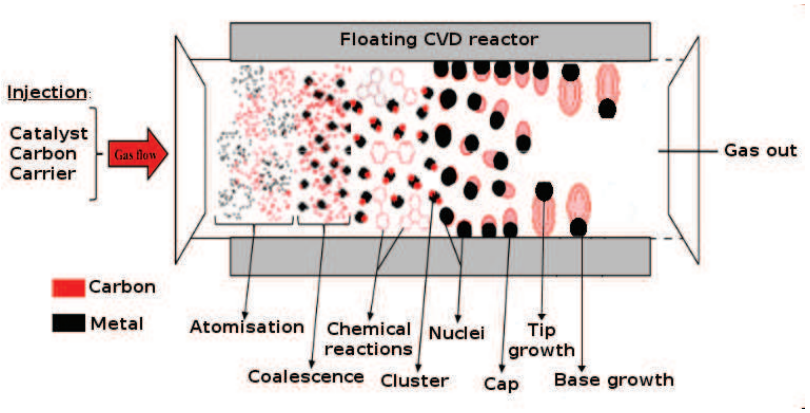

Figure 1.4.7: Schematic of the CNT growth by floating catalyst CVD.

1.5 Progress in CNT growth mechanism by floating catalyst CVD

Floating catalyst method in CVD process is nowadays commonly used since it is considered as one of the most easily scalable and economically viable technique. However, compared to supported catalyst, relatively fewer studies focused on the CNT growth mechanism by floating catalyst CVD. Even if the CNT synthesis by floating catalyst CVD also occurs on a substrate, the growth mechanisms significantly differ from the supported catalyst method. Hence, the models developed for supported catalysts can not fully explained the CNT growth by floating catalyst CVD [101].

For instance, in continuous floating catalyst CVD, the catalytic NPs formation should leastways not have precedence over carbon

deposition, the CNT growth mechanism may follow a way different from the widely accepted adsorption-diffusion-precipitation model, where the catalytic NPs should be first formed. Additionally, because more than 80% of the deposited carbon could assemble into CNT structures at a rather high carbon/metal atomic ratio, it is difficult to imagine that the dense carbon species would be gradually captured by the sparse catalytic NPs rather than immediately interact between themselves. Finally, various locations of catalyst NPs within CNTs and the specific morphologies and structures of the CNTs produced from floating CVD suggest that a direct application of the adsorption-diffusion-precipitation model is inappropriate in this case. Du et al. [36] proposed a particle-wire-tube evolution mechanism including three key steps as depicted in Fig. 1.5.1: (a) condensing gaseous carbonaceous species as nanoparticles; (b) self-assembling the nanoparticles into nanowires; and (c) emptying the nanowires into tubular structures.

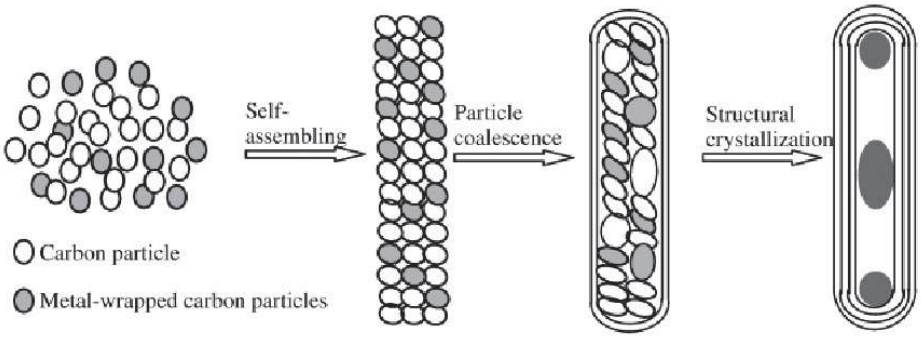

Figure 1.5.1: Schematic diagram of the proposed particle-wire-tube mechanism for nanotube evolution in floating CVD [36].

Nevertheless, this particle-wire-tube mechanism raises several questions. The first issue is why the NPs assemble in a 1D mode to form nanowires. Since the anisotropic properties of NPs are generally

responsible for their directional assembling, the authors suggest that the strong anisotropy of the NPs arises from numerous defects (such as sp^3 carbons, non-hexagonal rings, disconnected bonds...) especially at the two edges of the around-curved carbon (not graphite) layers. These defective layered structures might be kinetically stabilized by defect-defect interactions and possible catalyst-carbon conjugations, which could obstruct their closure into the isotropic graphitic particles and competitively enhance the probability of directional particle-particle interaction and assembling. The next key questions are how a nanowire transforms to a nanotube and how the hollow channel of a nanotube forms. The driving force involved in nanowire-nanotube transfomation is believed to be the structural crystallization and extension due to the relatively low stability of the carbon NPs. Under thermal annealing, they would exhibit a coalescence tendency and form more extended structures, accompanied with structural crystallization. To sum up, tiny carbon NPs would first form from a condensation of gaseous carbon species and then self-assemble into nanowires driven by an anisotropic interaction. The nanowires would finally develop into nanotubes, as a consequence of NP coalescence and structural crystallization. In this case the particle-to-wire assembly is possibly the rate-determining step, while the function of catalysts is to promote the anisotropic interactions between the NPs and the structural crystallization.

Since the catalyst roles consist in decomposing the carbon feed-stock(s) and providing a template for the nucleation of carbon patches, it is of paramount importance to monitor the different catalyst features during the CNT synthesis. However, the catalyst precursor decomposition is still unclear. The catalyst NPs being formed *in situ* in the gas phase, it becomes very difficult to accurately control their different features (i.e. morphology, chemical and physical

composition, location...). Although the use of non-metal catalyst for the continuous synthesis of CNTs was recently reported [177] (silica NPs were continuously produced from the thermal decomposition of PSS-(2-(trans-3,4-Cyclohexanediol)ethyl)-Heptaisobutyl and used as non-metal catalyst NPs while ethanol was served as both the solvent and the carbon source), solid organometallocenes, like ferrocene, cobaltocene or nickelocene are mainly used as catalyst precursors. We will therefore focus our attention on transition metal catalysts and more particularly on iron.

Theoretical studies of the thermal fragmentation of ferrocene revealed that H is released first, followed by fragments like C-H, C, C_2 or C_3, and finally Fe atom [42] [87], while the presence of individual metal atoms has not been experimentally confirmed yet. The catalyst precursor decomposition thus liberates both metal atoms and reactive carbon species, showing the difficulty to control the catalyst nature and morphology. It also raises the question of the CNT growth location: does it start from the gas-phase or from the substrate's surface? In the first case, the *in situ* formation of the CNT "embryos" formed in the gas-phase would reach and affix to the substrate and keep growing following either the tip or the root growth model. In the latter case, the as-formed suspended catalyst NPs in the gas phase being spherically shaped to minimize their surface energy would be gradually deposited on the reactor walls and substrates where the CNT nucleation and growth will occur. A recent study reported the simultaneous growth and separation of both SWNTs and MWNTs during the same CVD synthesis: the MWNTs were formed on the hot reactor walls, whereas the SWNTs were spontaneously originated in the gas phase [78]. It indicates that the early stages of the CNT growth is still under debate.

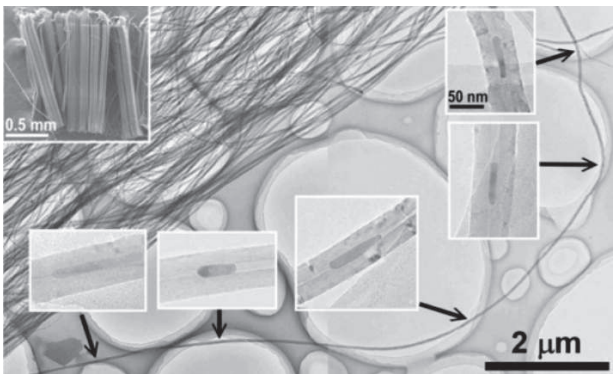

Figure 1.5.2: SEM image of a 1.5 mm array of CNTs grown by a floating catalyst CVD method. Five small TEM insets with the same magnification show catalyst particles encapsulated all along the CNT [174].

Furthermore, while it is well-admitted that one individual CNT grow from one single supported catalyst NP, it is no longer the case when the catalyst NPs are continuously provided and float in free-space. Several catalyst NPs were observed all along the CNT and at either ends of the tube [174] (see Fig. 1.5.2). This may indicate that nanotubes can grow upwards from particles that remain on the substrate and also behind particles that move away from the substrate at the growing tip of the nanotubes. In the case of supported catalysts, only one NP can be found at one of the CNT extremity depending on the growth mode (tip or root growth) [8]. How can several catalyst NPs be encapsulated in one individual CNT and what are the consequences on the growth? A first hypothesis is to consider the supported catalyst tip growth model. As the CNT lengthens, the catalyst NP will be lifted from the substrate surface. Since the end of the CNT exposed to the reacting atmosphere is filled with the catalyst NP and the opposite end remains fixed to the substrate, there is no way for additional catalyst NPs to get into the CNT. Hence, such model is not consistent with the floating catalyst mechanism.

Paradoxically, another explanation derived from this tip growth model was later proposed by Zhang et al. [186]. The tip growth process was suggested to occur open-ended, allowing new catalyst NPs to fall on the open tip. Hence, the CNT tip growth process would occur slowly without catalyst NPs on the tip, and very fast with catalyst NPs on the tip (see Fig. 1.5.3). Whereas *in situ* measurements confirmed the non linear growth rates [51], an open-ended tip growth mechanism is not energetically viable and recent studies based on shear force calculation [28], *in situ* ion beam analysis [134] and sequential feeding of two different catalyst sources (e.g. Ni and Fe) [174] unambiguously demonstrate that the CNTs from floating catalyst method grow via a base-growth mechanism. This indicates that the bottom ends of the CNTs are the active growth sites. Therefore, the catalyst NPs experience a constant encapsulation by CNTs to sustain a continuous growth. Moreover, the catalyst distribution along the CNT was found to be nearly uniform with higher concentrationsat the base and at the top of the CNTs, presumably due to the inerty of the CVD process [134].

Nevertheless, several points still remain open questions. For instance, the catalyst NP morphology, chemical and physical compositions were found to vary with its location in the CNT [80]. The high and low temperature phases of iron (γ-Fe and α-Fe) were found to be dominant inside the CNT cavities, whereas most of the residual particles at their tips were iron carbide. In addition, the catalyst NP rod shape inside the CNT cavities suggests a liquid-like or viscous state, while the presence of iron carbide induces a solid crystalline phase [89]. Besides these different points, we address below some of the most critical aspects of the CNT growth mechanism by floating catalyst CVD.

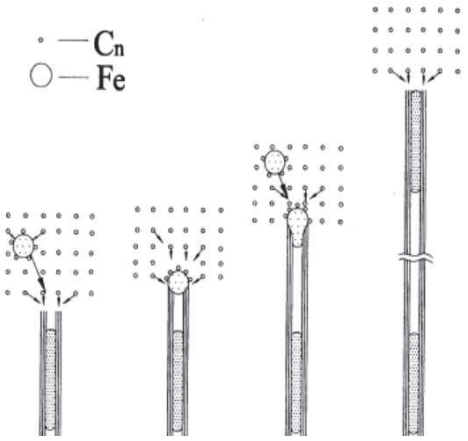

Figure 1.5.3: A proposed continuous CNT growth model based on an open-ended tip-growth mechanism [186].

1.5.1 Carbon diffusion pathways

The carbon diffusion pathway is one of the main keys of the CNT growth mechanism. It is largely determined by the carbon solubility of the catalyst NPs [182], which is itself largely influenced by the catalyst chemical composition and morphology. The transition metal catalysts possess relatively large carbon solubility. Among them, iron displays the highest one. Highly or moderately active catalysts are believed to promote carbon bulk diffusion, while catalysts with a marginal activity only allow surface diffusion of carbon atoms, as depicted in Fig. 1.5.4 [97].

For instance, catalysts with a carbon solubility ranging between 0.5 wt.% and 1.5 wt.% allow the rapid diffusion of carbon, subsequently inducing the rapid carbide formation or/and a quick graphite precipitation leading to CNT growth. In contrary, unsuccessful catalysts were

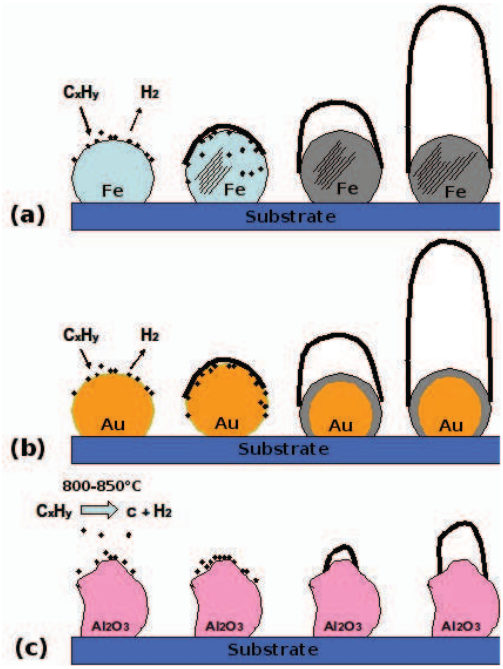

Figure 1.5.4: Four stages of CNT nucleation from three different types of catalyst are depicted. (i) Carbon precursor decomposition, (ii) carbon atom (indicated by small solid circles) adsorption and surface/bulk diffusion, (iii) carbon patch and cap (indicated by solid curved lines) nucleation, and (iv) CNT elongation. (a) For highly active transition metal catalysts, carbon bulk diffusion leads to the formation of carburized NPs (indicated by grey circles) and carbide phases (indicated by a group of slashed lines) from which CNT can nucleate. (b) For catalysts displaying a moderate activity, like some other metals, a carbon surface diffusion and the formation of a carburized shell on the NPs are proposed. (c) For non-metal catalysts, nano-protrusions on the solid and irregular-shaped NPs provide a template for the nucleation of a cap structure and further CNT elongation.

found either to have nearly zero carbon solubility, or to form stable or numerous intermediate species, making the diffusion of carbon in the catalyst and the graphite precipitation very unlikely. Therefore, the ability of a catalyst to successfully promote the growth of CNTs by CVD can be given by the following criteria. (i) There should be sufficient carbon solubility in the catalyst (1 at.%) within the

temperature range used during the synthesis. (ii) Following saturation of the catalyst, the precipitation of graphite should begin without the formation of any intermediate carbides. (iii) If carbides do form, diffusion of carbon through the solid solution and the carbides should be rapid and reach the carbon concentration needed to allow a fast graphite precipitation. Those three points were then used to look for other potential catalysts by examining the phase diagrams of a wide variety of elements as listed by Wirth et al. [173].

Table 1.5.1: Activation energy of different CVD systems using C_2H_2 as carbon feedstock.

Catalyst	Synthesis	Temperature (°C)	Activation energy (eV)	References
Fe	Floating thermal CVD	400-600	1.24	Chiang et al. [20]
Fe	Floating thermal CVD	550-625	1.22	Chiang et al. [22]
Fe	Floating thermal CVD	450-650	1.20	Dichiara et al. [31]
Fe	Thermal CVD	590-710	1.65	Liu et al. [101]
Fe	Thermal CVD	700-1000	1.52	Lee et al. [91]
Fe	PE-CVD	150-550	0.35	Hofmann et al. [65]
Fe	Surface reaction	350-470	1.86	Silcocks et al. [152]
Fe	Surface reaction	700-1000	1.25	Lee et al. [91]
Fe	Surface reaction	1050-1250	1.13	Palmer et al. [131]
Fe	Bulk diffusion	-	1.63	Smith et al. [154]
Ni	Floating thermal CVD	400-600	0.76	Chiang et al. [20]
Ni	Floating thermal CVD	550-626	0.76	Chiang et al. [22]
Ni	Floating thermal CVD	450-650	0.80	Kim et al. [82]
Ni	Thermal CVD	550-900	1.22	Ducati et al. [37]
Ni	Thermal CVD	700-1000	1.31	Kim et al. [82]
Ni	PE-CVD	150-550	0.23	Hofmann et al. [65]
Ni	Surface reaction	350-425	0.30	Mojica et al. [118]
Ni	Bulk reaction	-	1.51	Diamond et al. [30]

Furthermore, the identification of the rate-determining step is highly influenced by the carbon diffusion pathway. Most of the CNT growth by floating catalyst CVD reported in the literature assume a diffusion limited rather than a supply limited reaction. Only specific CVD conditions under low pressure and temperature [55], or ultra-long CNT growth [175] would change the balance towards a supply limit. Being a thermally activated process, the carbon diffusion into or on the surface of a catalyst particle can be described by the Arrhenius relation. In general, the activation energies for temperatures above 600°C are significantly close to the 1.6 eV energy value found for the bulk diffusion of

carbon into iron. For instance, Baker et al. [5] associated the energy of filamentary carbon growth to the activation energy of diffusion of carbon in the catalyst NP, postulating that the bulk diffusion of carbon is the rate-limiting step for CNT growth. Rodriguez-Manzo et al. [142] also added that the CNT growth mechanism is essentially the same for all the transition metal catalysts (Fe, Ni, Co and their alloys) under similar CVD conditions, as observed in the table below. Moreover, in the case of carbide phase formation during the synthesis as mentioned above, it suggests that the energy gain from the carbide formation must be large enough to overcome the energy barrier for carbon bulk diffusion. Finally, for temperatures below 600°C, the activation energy of the reaction is about 1.2 eV, indicating that both bulk and surface diffusions may contribute to the CNT growth under such conditions [139].

1.5.2 Catalyst-substrate interactions: influence on the CNT growth

The catalyst-substrate interactions can induce significant changes on the catalyst features (i.e. chemical nature, structure, morphology...) which will subsequentially influence the CNT growth mechanism and kinetics. First, molecular dynamic simulations [33] revealed that the catalyst cluster melting point dramatically raises with the increase of the catalyst-substrate adhesion, which may induce changes in the carbon diffusion pathways. The catalyst morphology and size distribution also depends on the catalyst-substrate adhesion. In general, the substrates restricting the catalyst mobility, like alumina where the presence of Fe_2^+ and Fe_3^+ detected at the interface indicates a strong interaction, provide a narrower particle size distribution, resulting in dense vertically-aligned CNTs [110]. In contrary, the substrates with high surface tensions, such as tantalum, are known to enhance the

CNT growth rate by forming a catalytic wetting layer [171]. Moreover, the strength of the catalyst-substrate interaction may help the bias formation of specific CNT chiralities by altering the dynamic structural behavior of the NP, in turn influencing the interplay between CNT and NP structures. For instance, the contact region between the NP surface and the growing CNT decreases as the catalyst-substrate interaction strength increases because capillary forces that raise the catalyst into the CNT are counteracted by the strong catalyst-substrate interaction [53]. The CNT growth modes (i.e. root or tip growth modes) can be affected as well by the adhesion between the catalyst and its support [135]. *In situ* ETEM observations show two distinct kind of CNTs, referring to either a continuous intimate contact with the substrate dominated by van der Waals forces, or a mere substrate anchoring of CNTs held afloat during growth. The last type called "flying" CNTs grow unobstructed and straight to millimeter lengths are susceptible to external forces, while the first one called "crawling" CNTs are strongly affected by substrate topography.

Furthermore, the crystallographic orientation of the exposed substrate surface was found to govern the CNT growth direction. For instance, CNTs preferentially grow at 90° on Si (100) surface, but at 60° on Si (111) surface [158]. Similarly α-plane sapphire leads to CNT growth normal to (001), while no orientation is observed on c-plane or m-plane sapphire [56]. Single-crystal MgO (001) substrate shows preferential growth of CNTs along (110) direction [107]. More recently, our group reported an orthogonal CNT growth on micro-sized alumina particles [63], proving that the grain boundary or crystalline steps of the support material play a crucial role in CNT growth and orientation.

Finally, some substrates, like clay minerals, already contain specific chemicals in their composition which can serve to promote the CNT

growth without using any additional catalyst. For instance, in the case of nontronite, the presence of iron (Fe) was used to grow CNTs by hot filament CVD [133]. Some other substrates, such as porous alumina, were found active enough to allow catalyst-free CNT growth [160].

1.5.3 CNT NUCLEATION SITES

The formation of step edges on catalyst surface, resulting from complex and dynamic interactions between catalyst, substrate and carbon at their interface, were sparsely observed during CNT growth by CVD. Due to their high surface energy, these step edges were supposed to act as active sites for binding, segregating and precipitating carbon species and thus for the formation of graphitic structures. First principle calculations revealed that for the transition metal catalysts, the adsorption sites at the step are preferred over those on a (111) terrace, while in the case of other metals, like Pd, Pt or Ag, the surface adsorption sites are more stable than the step edge sites. For instance, mono-atomic steps on crystalline Ni NP surface were observed [64], as exposed in Fig. 1.5.5. The graphene layers were supposed to nucleate between a pair of these steps by surface diffusion of carbon toward this edge. In addition, direct observations of the Ni-C interface at the tip of a CNF indicated that graphitic layers emerge at various angles of the Ni steps with 3-4 monolayers in height, and that subsequent graphitic layers nucleate at this Ni-C interface [65]. Another example shows the graphene formation on step sites on the surface of Co (111) lattice plane [188]. In this case, carbon atoms can easily precipitate from the step edges onto the catalyst surface to form graphene, which significantly lower the local energy at the step edge site.

These results suggest that a correlation between the catalyst and

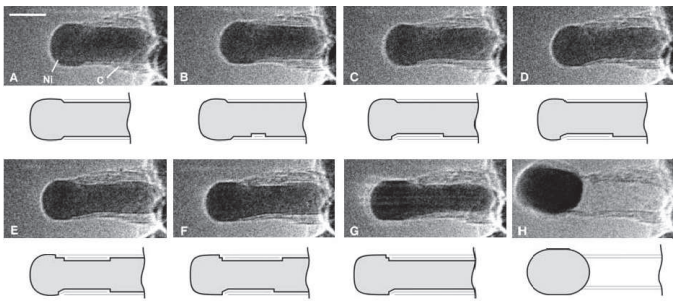

Figure 1.5.5: *In situ* TEM images showing the presence of mono-atomic steps on crystalline Ni NP surface [64].

CNT orientations may exist during initial nucleation. The existence of a template-effect was recently demonstrated theoretically [53] and experimentally [21] and may be a step towards chiral-selective growth. However, such epitaxial relation may be important in nucleation of the walls but not anymore during their growth. Indeed, the formation of the initial CNT seed on the catalyst is important and the CNT orientation and chirality may be determined at this initial stage. Nevertheless, the orientational relation between the catalyst and the CNT(s) may change as the growth proceeds by the addition of carbon atoms to the existing graphene edges. These observations are consistent with the idea that once an initial seed is formed, all that is needed is a source of carbon to facilitate further growth by addition to existing graphene edges. Thus, when the orientational correlations between the CNTs and the catalyst particles are examined at later stages of the growth, one may not find a correlation. For instance, Fe_3C catalyst crystals attached to the substrate, from which the CNTs grew, were found to exist in a variety of different orientations relative to the CNT axis [9], suggesting that CNTs do not elongate via epitaxy on the catalyst particles.

1.5.4 The CNT nucleus in catalytic CVD

The nucleus for CNT growth was studied by numerous *in situ* observations, and theoretical investigations. The formation of a cap structure on the transition metal catalyst NPs was frequently observed. For instance, a cone-shaped cap structure on Co catalyst was examined in the initial growth stages of SWNTs [188], as shown in Fig. 1.5.6. A small-sized carbon cap was found to emerge on the top of each Ni catalyst NP, leading to SWNTs with hemispherical graphitic caps [65]. The cap structure formation with a unique carbon layer on the surface of Fe NPs was observed during the early stages of SWNT growth [128], while the formation of a multilayered cap was reported during the MWNT nucleation on FeCo catalyst surface [142]. Nevertheless, the absence of a cap structure was also reported under specific conditions, like for the SWNT nucleation from sharp metal tips [143].

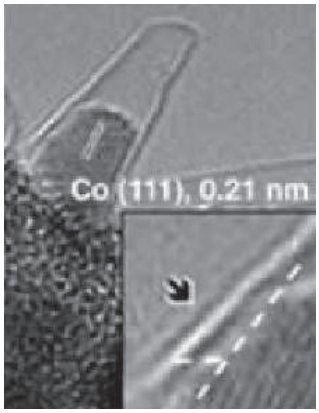

Figure 1.5.6: A step site on the surface of a Co NP [188].

However, only few studies focused on the processes prior to cap formation. Due to the dimensional [1-100 nm] and time scale (below 1 s) of the CNT nucleation and growth, experimental observations have to be supplemented by theoretical calculations and computer simulations to unravel the roles played by the catalyst NPs in the early

stages of the growth [72]. Various carbon species were supposed to be responsible for the cap structure formation, like hexagonal carbon networks [151], olefin species [165], carbon linear chains [4], atomic rings [130] and/or C_n species (with n ranging from 1 to 4) [120].

The influence of the cap structure on the CNT chirality has been widely discussed. With a good control over the cap geometry, structure and energy at the early nucleation stage, CNTs with a selective chirality can be grown [52] [141]. A correlation between the CNT chirality selectivity and the angle of step edges on (111) planes was found with respect to the growth direction [189]. Nevertheless, the orientational relation between the catalyst and the CNT(s) may change as the growth proceeds as mentioned above. The evolution of the cap shape during CVD process was investigated by in-situ TEM [99] (see Fig. 1.5.7). The cap was found to keep close during the synthesis, with an irregular shape during the growth and a round one during shrinkage [75]. The high density of carbon atoms available in the vicinity of the cap fragment can lead to a rearrangement of the existing sp^2-carbon-cap structures, forming defects, such as pentagon, heptagon and four/eight-member ring, and/or intermediate structures, like short polyyne chains.

Furthermore, despite this Chapter focused on iron-based catalysts, one must bear in mind that other transition metals might exhibit marked differences in their affinity and reactivity with the CNT. For instance, Zoberdier et al. [190] recently showed that W reacts only weakly with the CNT, while Re creates localized defects on the sidewall, and Os reacts readily causing extensive defect formation and constriction of the CNT sidewall followed by total rupture of the tubular structure.

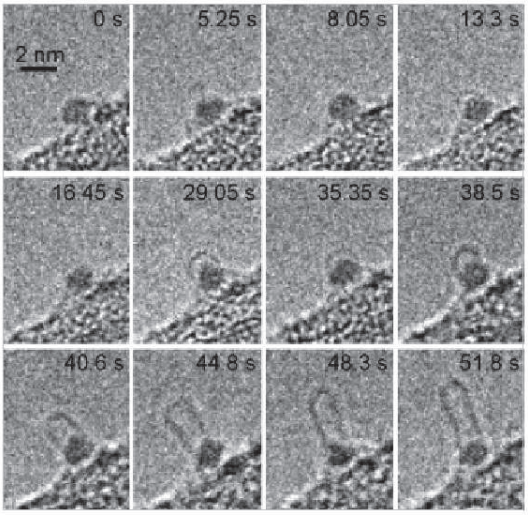

Figure 1.5.7: Atomic scale *in situ* observations of catalyst during CNT growth by CVD [99].

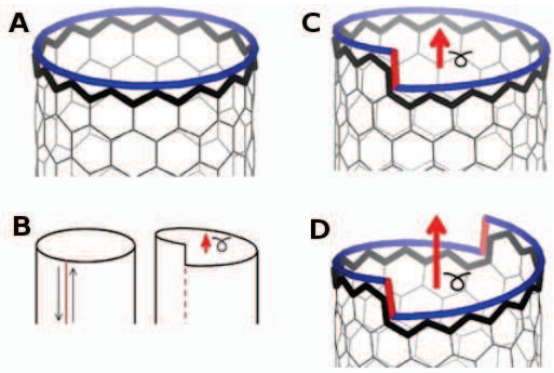

Figure 1.5.8: The screw dislocation-like model in the CNT growth. An achiral zigzag (n,0) tube (A) can be viewed as a perfect crystal, and transformed into a chiral one by cutting, shifting by a Burgers vector b (red arrows in BD), and resealing a tube cylinder (B). The chiral (n,1) in (C) and (n,2) in (D) tubes contain the axial screw dislocations with a single and double value of b, accordingly; the corresponding kinks at the open tube-end are marked in red [34].

Finally, after the carbon cap formation, the tube structure is supposed to elongate according to the dislocation theory [34]. Any CNT may be viewed as having a screw dislocation along the axis, as shown in Fig. 1.5.8. Consequently, its growth rate is shown to be proportional to the Burgers vector of such dislocation and therefore to the chiral angle of the tube, indicating the difficulty of growing zig-zag SWNTs rather than chiral ones. *In situ* field emission microscopy observations of the growths of individual CNTs revealed that the CNTs often rotate axially during growth [106], while Maruyama et al. [140] showed the evidence for chirality dependent growth rates of individual CNTs. Whereas the previous studies support the screw-dislocation-like CNT growth, more experimental data are required to confirm this model.

1.6 Summary

In this Chapter, we reviewed some basic knowledges of CNTs and other carbon allotropes. Various CNT synthesis routes were discussed and among them, floating CVD appeared of increasing significance for large-scale production of well-controlled CNTs. The state of the art research of floating CVD was thus reported. Moreover, CNTs based hybrid materials were largely investigated because of their outstanding properties and attractive application potentials in a wide range of fields such as biotechnology, catalysis, energy storage or aeronautics. Especially, multiscale hybrid materials consisting of CNTs and µ-particles or fibers are among the most promising materials which could be used as multifunctional fillers in composites. Due to the unique nano-micro hybridization, two great issues of typical CNT-based composites, i.e. CNT agglomeration and poor interfacial load transfer between filler-filler and filler-matrix, could be easily overcame when employing these hybrid structures as fillers. The CNT

hybridization with graphene nanoplatelets was shown as an example of the promising potential of this method, and their electrical, thermal and mechanical properties were tested as well as their *in situ* sensing abilities.

In the next part of this research, Chapter 2 will introduce the floating CVD process used in this research to synthesize the CNT-based materials and present the different ways of characterization developped to study the growth mechanism and the CNT structure. Then, Chapter 3 and 4 will focus on CVD gas phase investigations by the mean of *in situ* diagnostics and numerical simulations. Chapter 5 will study the role of the substrate and the influence of its features on the CNT morphology and yield. After that, Chapter 6 will deal with the CNT steady state growth on the substrate surface and different growth termination processes will be examined. Finally, Chapter 7 will summarize this research and suggest some perspectives that could be followed to deeper this work. Last but not least, health and environmental considerations of CNT-based technologies will be debated.

No amount of experimentation can ever prove me right; a single experiment can prove me wrong.

Albert Einstein

2

Experimental procedure

In this Chapter, the materials and equipments used in this research to synthesize the CNTs and their related products are presented. The different *ex situ* characterization methods are then introduced followed by the *in situ* techniques.

2.1 CNT growth by aerosol-assisted CVD

2.1.1 Materials and equipments

The main materials involved in this study are listed in the table below.

Table 2.1.1: Informations related to the main materials used in this research. G, L and S stand for gas, liquid and solid.

Materials	Formula	State	Origin
Xylene	C_8H_{10}	L	Alfa Aesar
Toluene	C_7H_8	L	Alfa Aesar
Acetylene	C_2H_2	G	Air Liquide
Ferrocene	$Fe(C_5H_5)_2$	S	Alfa Aesar
Argon	Ar	G	Air Liquide
Hydrogen	H_2	G	Air Liquide
Alumina	µ-Al_2O_3	S	Perf. Ceramics Comp.
Silicon carbide	µ-SiC	S	Marion Technol.
Graphene	GN	S	K-Nano
Titanium carbide	µ-TiC	S	Marion Technol.
Carbon fiber	CF	S	Porcher
Epoxy resin	-	S	Resoltech
Hardener	-	L	Resoltech
Poly(vinylidene fluoride)	PVDF	S	Arkema
N,N-dimethylformamide	DMF	L	Arkema

2.1.2 Injection system

The injection method utilized in this study is a "top down" technique consisting of the formation of an aerosol. The solid state catalyst precursor (i.e. ferrocene) was initially dissolved into a solvent used as the carbon feedstock (i.e. xylene). The solution was injected into the reactor by a spray composed of two concentric tubes of 0.5 mm diameter, one for gas and the other for liquid, as depicted in fig 2.1.1. The liquid flow was controled by an electronic syringe system (Razel Science, R99-E), while the gas flows were monitored by thermal electronic gas flow meters (Brook Smart).

The principle of the spray consists of the production of small droplets (aerosol) by dislocation of the solution injected into a high speed gas

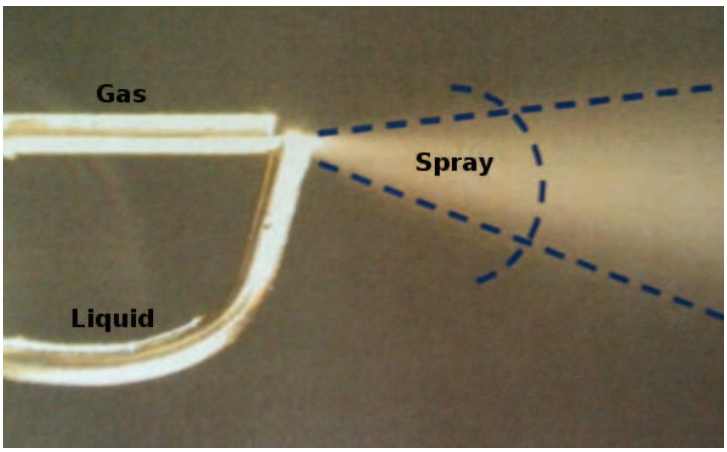

Figure 2.1.1: Image of the injection system used to spray the precursors into the CVD reactor.

stream. Atomizing a liquid means disintegrating the continuous phase in small fragments and droplets to increase the liquid-gas interfacial area. This requires to provide enough energy to the liquid to overcome both the reacting forces due to surface tension and the dissipating action of liquid viscosity. From an energetic point of view the process can be viewed as an energy transfer to the liquid in order to increase its surface energy. That is why the gas flow should not be too low to allow a good dispersion of the liquid, while an excessive flow rate would induce a recirculation effect in the reactor. The process can be assimilated as a continuous cross-flow injection. The liquid jet issuing from the section of the nozzle impinges on the transverse gas flow and is progressively deflected until its eventual alignment with the duct axis; in the meanwhile the gas drag promotes the distortion of the cross section of the jet and the stripping of small liquid fragments. A preheating system was set up at the end of the injection to ensure the direct vaporization of the spray. This method allows a fast and efficient mixing of the different precursors, which is of primary importance especially because the residence time in the reactor is relatevely short.

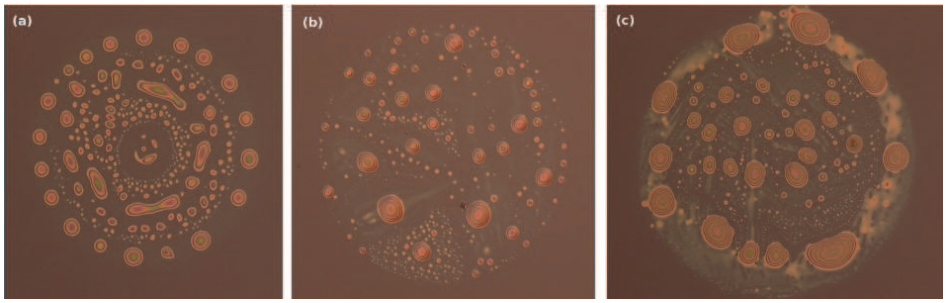

Figure 2.1.2: Microscopy images of droplets observed after impact on a quartz plate at 2 cm after the injector exit. Each droplet originated from solutions at different concentrations: (a) 0.01, (b) 0.05 and (c) 0.1 g/mL. The height of each image corresponds to 286 µm.

The size of the droplets was measured at 2 cm after the injector exit by microscopy observations of the droplet impacts on a quartz plate. The injection conditions were as follow: the liquid and the gas flows were set at 0.2 mL/min and 1 L/min, respectively. The liquid solutions were composed of ferrocene dissolved into xylene at different concentrations. Argon was fed as the carrier gas at room temperature and atmospheric pressure. Representative images of the droplet impacts are shown in Fig. 2.1.2. These observations confirmed that the droplets are spherically shaped and allow the evaluation of their diameter by counting and sizing them. Three different concentrations were used for the liquid solution: 0.01, 0.05 and 0.1 g/mL. Figure 2.1.3 shows a slight increase of the droplet mean diameter with the increase of the liquid solution concentration. Moreover, these observations indicate that the droplet size distribution, which is bimodal, does not change much with the concentration. One population of droplets is ranging about 220 µm, while the other one is about 285 µm diameter.

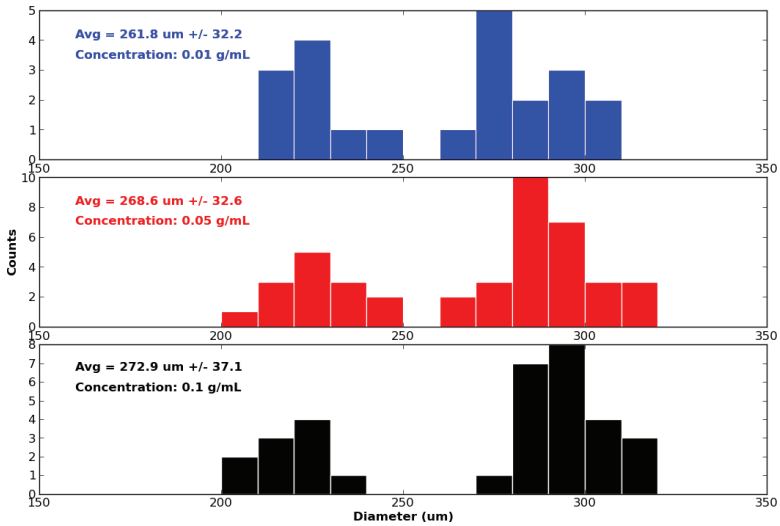

Figure 2.1.3: Droplet diameter distribution at 2 cm after the injector exit as a function of the liquid solution concentration.

2.1.3 CVD REACTOR

The CNT synthesis was carried out by catalytic CVD in a quartz tube reactor (110 cm long, inner diameter 45 mm). The reactor was placed in a two region oven under inert atmosphere. The first region (about 10 cm long) served for preparing the ferrocene/xylene working mixture by selecting the proper vaporization temperature, concentration and injection speed of the reagents in the mixture. The advantages of using ferrocene as a catalyst precursor are its innocuity and its low costs. The mixture was then sprayed by the carrier gas to the high temperature region as detailed earlier, where the decomposition of the different precursors took place by pyrolysis and/or catalysis. This zone was composed of a 60 cm long horizontal furnace (Carbolite, HZS) where the temperature was ranging between 400 and 1000°C. The temperature profiles were measured along the wall of the quartz tube at different set temperatures, as depicted in Fig. 2.1.4 and in Table 2.1.2. A K type thermocouple was introduced at different

positions into the CVD reactor. The quartz tube was kept well-sealed and argon was provided at 1 L/min during the measurements. The position of the quartz plate used as a substrate or as a substrate holder is marked by two red lines between two orange lines in Fig. 2.1.4 corresponding to the inner limits of the high temperature furnace.

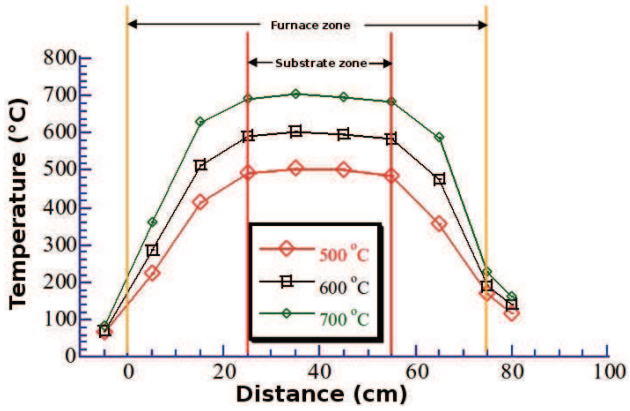

Figure 2.1.4: Temperature profiles along the reactor of the 45 mm diameter quartz tube at different set temperatures.

After heating the reactor to the set temperature under inert atmosphere and waiting for about 30 min for equilibrium, the liquid solution was fed in the form of spray and carried into the reactor. The carrier gas was composed of a mixture of argon (Ar, 99.8% purity, full scale: 10 L/min [6-20 vol.%]) and hydrogen (H_2, 99.9% purity, full scale: 5 L/min [0-9 vol.%]) introduced with different ratios into the reactor. The total gas flow rate was kept at 1 L/min. Acetylene was added as a second carbon feedstock at the same time as the ferrocene/xylene solution was fed (C_2H_2, 99.6% purity, full scale: 1 L/min [0-10 vol.%]). In general, the injection lasted from 5 to 30 min and could be divided into several sequences depending on the experiments. At the end, the furnace was cooled down to room temperature under argon at 1

Table 2.1.2: Temperature values measured along the center of the high temperature furnace at different set temperatures.

Distance (m)	450°C	550°C	600°C	650°C	700°C	850°C
0.02	317	402	460	511	573	755
0.07	383	476	536	592	631	799
0.12	422	521	569	628	673	824
0.17	449	543	588	646	690	838
0.22	455	551	597	651	698	845
0.27	460	557	604	657	704	854
0.32	459	558	605	657	705	856
0.37	452	552	602	653	703	851
0.42	444	545	597	646	699	844
0.47	434	539	591	641	692	836
0.52	414	518	580	630	681	823
0.57	376	481	555	602	659	798

L/min. A schematic representing the overall CVD system is presented in Fig. 2.1.5.

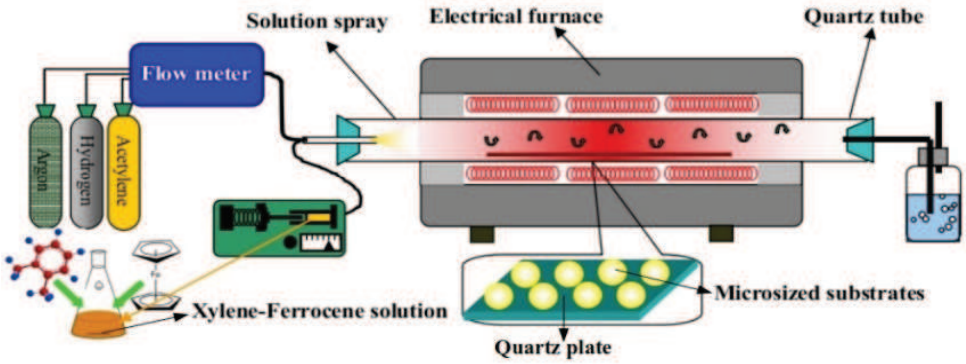

Figure 2.1.5: Schematic of the CNT growth by liquid injection CVD.

The residence time was estimated as the mean time needed for chemical species to go through the isothermal zone in the reactor. The isothermal zone can be determined by the temperature profiles of the

reactor depicted in fig. 2.1.4. The residence time is given by the following expression, where V is the volume of the isothermal zone (in our case $V = 0.48 \cdot 10^{-3}\mathrm{m}^3$) and Q corresponds to the volumetric flow rate at given pressure and temperature:

$$t = \frac{V_{isothermalzone}}{Q}$$

Hence, the residence times in our CVD reactor were determined as a function of both the total gas flow rate and the furnace temperature, as shown in Fig. 2.1.6.

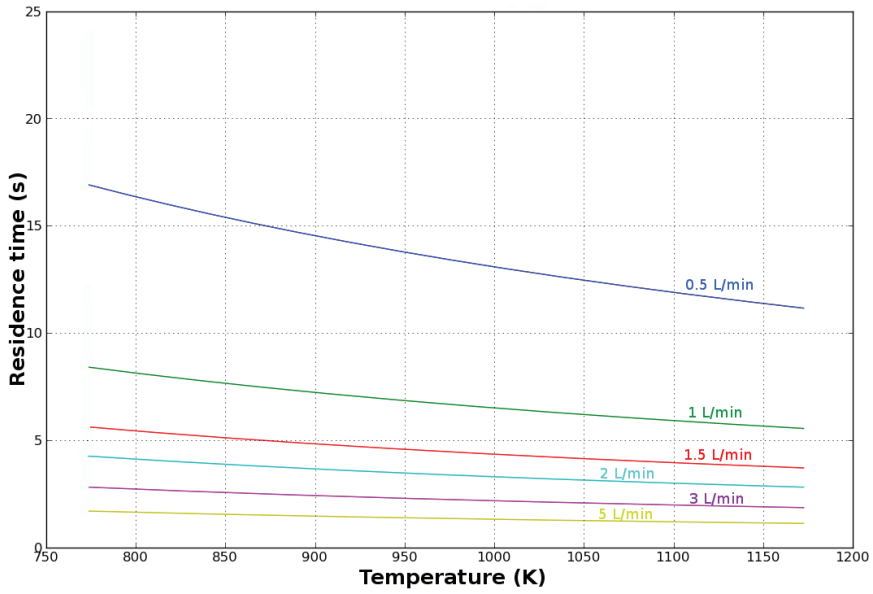

Figure 2.1.6: Residence time in the isothermal zone of the CVD reactor as a function of the furnace temperature and the total gas flow rate.

2.2 *Ex situ* CHARACTERIZATION METHODS

Various samples were collected at different positions on the quartz plate surface after the CVD synthesis. They were then characterized by different techniques as mentioned below.

2.2.1 ELECTRON MICROSCOPY

While optical microscopy is limited to the observation of µ-sized samples as illustrated in Fig 2.2.1a, electron microscopy consists of an essantial tool to examine the morphology of the as-prepared structures at a sub-micron scale. Three different equipments where utilized in this research: a scanning electron microscope (SEM, LEO Gemini 1530), a transmission electron microscope (TEM, JEOL 1200 EX) and a high resolution transmission electron microscope (HRTEM, Philips CM20-UT). While the SEM technique allows direct sample observations without any exaction, the TEM/HRTEM samples were prepared by sonicating a small amount of the as-prepared nano-structures in ethanol for 2 min and drying few drops of suspension on a Cu micro-grid. Examples of CNT structures observed by SEM and TEM are depicted in Fig. 2.2.1b and 2.2.1c, respectively. Our TEM system also allows sample analysis based on selective area electron diffraction (SAED). For instance, in the case of pure CNTs, the SAED pattern presents one pair of small but strong arcs of 002 reflections [149], revealing graphite-like concentric cylindrical structures.

2.2.2 THERMOGRAVIMETRIC ANALYSIS

Thermogravimetric analysis (TGA) consists in determining changes in weight in relation to a temperature program under a controlled

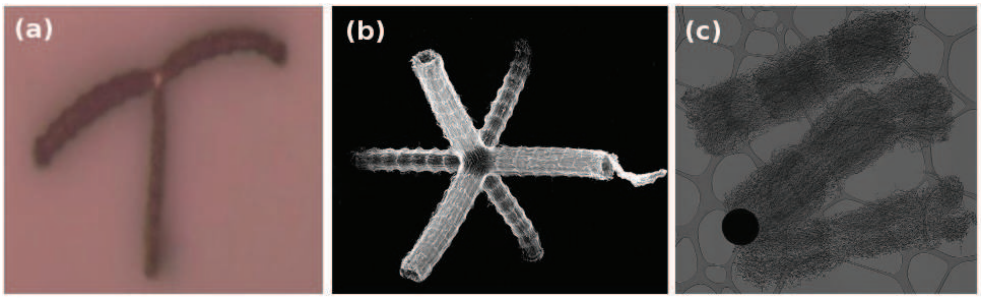

Figure 2.2.1: Examples of CNT-multilayers grown on μ-Al_2O_3 observed by optical microscopy (a), scanning electron microscopy (b) and transmission electron microscopy (c).

atmosphere. The sample temperature is raised up gradually and the sample weight is plotted against the temperature. In this research, the same program was performed for all the samples. A mass of CNT structures ranging between 10 and 20 mg was placed into the TGA analyzer (NETZSCH STA 449 F3 Jupiter) under an oxydizing atmosphere (flow rate of air: 1 L/min). The samples were then heated up from 30°C to 1000°C at 10°C/min. For pure CNT samples, the main mass loss is attributed to the oxydation of carbon. Carbon entirely transforms into CO_2 and the iron presents in the catalyst NPs turns to iron oxydes as illustrated in the equations below. Besides the thermal stability, it is thus possible to determine the amount of iron initially present in the CNTs.

$$3\,C + 2\,O_2 \longrightarrow 2\,CO + CO_2$$
$$4\,Fe + 3\,O_2 \longrightarrow 2\,Fe_2O_3 \text{ or } 3\,Fe + 2\,O_2 \longrightarrow Fe_3O_4$$

2.2.3 Raman spectroscopy

Raman spectroscopy analysis was performed in the range of 1050-3000 cm^{-1} by a Jobin Yvon LabRam spectrometer using an excitation wavelength of 632.8 nm. The CNT-based samples exhibit two first-

order peaks centered around 1325 cm^{-1} and 1585 cm^{-1}, corresponding to the so-called D and G bands, respectively. The G band is commonly attributed to the sp^2-bonded carbon, while the D band stands for the scattering of sp^3-bonded carbon plus a possible contribution of the disordered sp^2 phase [24]. In graphite-like carbon such as CNT or graphene, the D band originates from the structural defects. Hence the intensity ratio of the D band over the G band (I_D/I_G) is commonly used to quantify the CNT structural quality [86]. A lower I_D/I_G ratio thus suggests fewer structural defects in CNTs as well as higher purity [86]. Furthermore, the full-width at half-maximum (FWHM) of the G band can be used to determine the CNT crystallinity degree [86], as well as the second-order peak at 2700 cm^{-1}. This peak is usually assigned to 2D vibration and an increase of this 2D band can be interpreted as a better ordering of the graphitic structure [24] [86].

2.3 *In situ* CHARACTERIZATION METHODS

The CNT structure and properties are currently characterized by collecting samples for subsequent processing which do not provide a real-time feedback about what happens during the synthesis to unravel the growth mechanism. High process control and optimization will therefore benefit from real-time, non-intrusive and *in situ* diagnostics, such as those presented below.

2.3.1 LASER INDUCED INCANDESCENCE

HISTORY

The first use of the laser-induced incandescence (LII) technique was presented by Weeks and Duley in 1974 [172] in the case of aerosols composed of carbon black and alumina particles. The suspended par-

ticles irradiated by an intense laser radiation exhibited a momentary emission of light. It was found that this light contains informations about the size and composition of the particles. A first set of equations involving different heat transfers was proposed.

A decade later, Eckbreth found severe interferences during the Raman scaterring analyses of a combustion system. The source of these interferences was identifed as the Laser Modulated particulate Incandescence (LMI) [41]. Eckbreth worked on these signals to improve the signal/noise ratio of the Raman spectra. He examined the signal intensity and decay time under different conditions to determine a mathematical expression related to the Planck's law. Based on this work, Melton developed detailed equations of the incandescence phenomenon and suggested the possibility of using such signal to measure both the volume fraction (corresponding to the signal intensity) and the primary size (related the signal decay time) of particles like soot [111]. Then, the term LMI was replaced by LII or L2I standing for Laser-Induced Incandescence. The LII technology emerged and several teams investigated its potential. Hence, Vander Wal et al. [169] and Leipertz et al. [26] performed extensive study about the influence of the laser wavelength and fluence on the soot volume fraction and primary particle size. Santoro et al. [146] focused on the study of Polycyclic Aromatic Hydrocarbons (PAH). In 2002, R. Vander Wal et al. [170], reported for the first time the use of LII applied to the CNT growth by flame synthesis. The CNTs were produced in a pyrolysis flame configuration as mentioned in Chapter 1 using a solution of iron nitrate dissolved into ethanol carried by a mixture of CO, H_2, He and C_2H_2. This process yielded nearly exclusevely SWNTs with Fe particles. It was found that the catalyst NPs mainly contribute to the incandescence emission. Nowadays, LII is a non-intrusive and high throughput diagnostic widely used in combustion, such as vehicular

on-board testing or industrial exhaust emission analysis.

Theory

The time-resolved laser induced incandescence (TRLII) consists in measuring a mean particle diameter along the path of a laser beam. The principle is based on the detection of the thermal radiation of particles heated up by a short laser pulse, where the complete time-dependent particle emission is recorded during particle cooling. The signal magnitude is correlated with the particle volume fraction, whereas the signal decay rate is assumed to be associated with the primary particle size [147]. For signal quantitative evaluation, the measured cooling curves have to be fitted by calculated signals based on a theoretical model [115] [166]. The TRLII theory used in the present study is based on the energy balance of a single iron [83] or carbon [144] spherical particle during heating by a laser pulse and cooling. In Fig. 2.3.1, Q_{int} is the particle change in internal energy, Q_{abs} corresponds to the energy flux of laser absorption, and Q_{rad}, Q_{cond} and Q_{sub} refers to heat losses due to radiation, heat conduction and sublimation respectively. Energy losses due to other phase transitions, like photodesorption [114] or oxidation [116] are neglected under our conditions.

It is assumed that the particles are heated up only once per laser pulse, meaning that the multiple reflections of the laser in the system can be neglected. The process of absorption of electromagnetic radiation by a particle is described by the Mie theory [77]. In the Rayleigh limit of absorbing spheres with sizes small compared to the laser wavelength, the expression of the laser light absorption by the particle is given by:

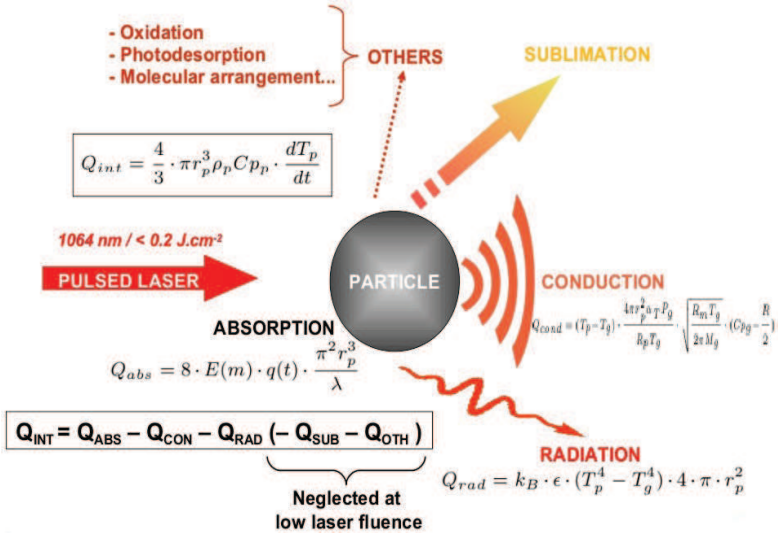

Figure 2.3.1: Energy balance in a single spherical particle during heating by a laser pulse and cooling through different heat transfers.

$$Q_{abs} = 8 \cdot E(m) \cdot q(t) \cdot \frac{\pi^2 r_p^3}{\lambda} \tag{2.1}$$

where, $E(m)$ corresponds to the particle refraction index, r_p describes the particle radius, λ is the laser wavelength and $q(t)$ refers to the laser profile (a gaussian temporal profile was used).

The resulting change in internal energy for a single spherical particle is given by equation (2.2), where, ρ_p and Cp_p are the density and the heat capacity of the particle respectively and T_p its temperature.

$$Q_{int} = \frac{4}{3} \cdot \pi r_p^3 \rho_p C p_p \cdot \frac{dT_p}{dt} \tag{2.2}$$

Different models for describing the heat fluxes exist [115]. Nevertheless, under our conditions the Knudsen numbers being significantly higher than one, it means that the heat transfer proceeds in the free

molecular regime. Hence, the expression of the heat conduction is given by the equation (2.3), where the translational energy accomodation coefficient α_T can be considered as an efficiency factor for the energy transfer during molecular collision, which was assumed to be equal to 1. P_g, M_g and Cp_g respectively correspond to the pressure, the molecular mass and the heat capacity of the gas, while R refers to the universal gas constant given in pressure (R_p) and in mass (R_m).

$$Q_{cond} = (T_p - T_g) \cdot \frac{4\pi r_p^2 \alpha_T P_g}{R_p T_g} \cdot \sqrt{\frac{R_m T_g}{2\pi M_g}} \cdot (Cp_g - \frac{R}{2}) \tag{2.3}$$

Moreover, for high laser fluences, the particles reach high temperatures inducing the sublimation of some fragments from the particle's surface. In other words, if the laser energy is sufficient to heat the particle above its sublimation threshold, some fragments will sublimate from the particle surface resulting in a mass loss of the particle and an increase of mass in the gas phase. However, for laser fluence below 0.6 J.cm^{-2} the heat transfer by sublimation can be neglected [13]. Excitation laser fluence greater than this value lead to superheated plasmas with temperatures well above the vaporization point of carbon. The temporal evolution of the emission signal at these fluences is consistent with plasma dissipation processes, but not with incandescence from solidlike structures. Therefore, a laser energy density of 0.2 J.cm^{-2} was used at a wavelength λ=1064 nm all along this study, allowing us to neglect the heat transfer by sublimation.

Finally, the heat loss due to radiation follows the Stefan-Boltzmann law. Thus, the emitted power over all the wavelengths is given by:

$$Q_{rad} = \sigma \cdot \epsilon \cdot (T_p^4 - T_g^4) \cdot 4 \cdot \pi \cdot r_p^2 \tag{2.4}$$

with, σ corresponding to the Stefan-Boltzmann constant, T_p and T_g describing the particle and its surrounding temperatures respectively and ϵ refering to the total emission coefficient.

The particle temperature as a function of cooling time can be calculated by solving the differential equation system (Eqs. (2.1) to (2.4)). A fourth order Runge-Kutta algorithm was implemented in the present work for that purpose. The particle temperature can be eventually related to the detected TRLII emission signal using Planck's law [47], where h is the Planck constant, c is the speed of light and $\Omega(\lambda)$ is the spectral response of the system. Therefore, the particle size can be estimated by comparing the decay time between the theoretical and the experimental TRLII signals.

$$S_{TRLII}(\lambda, T_p) = 64\pi^3 hc^2 r_p^3 E(m) \cdot \int_{\lambda_1}^{\lambda_2} \frac{\Omega(\lambda)}{\lambda^6 \cdot \left(e^{\frac{hc}{\lambda k_B T_p}} - 1\right)} \, \mathrm{d}\lambda \qquad (2.5)$$

Table 2.3.1: Summary of the symbols used in the TRL2I model with their corresponding values for both carbon and iron particles. Please refer to the references cited in the main text for more details.

Symbol	Description	Value for Fe	Value for C
E(m)	particle refraction index	$\frac{\lambda}{8\pi r_p}$	-
σ	Stefan-Boltzmann constant	$5.67 \cdot 10^{-8} J.m^{-2}s^{-1}K^{-4}$	-
ϵ	emission coefficient	1	-
r_p	particle radius	1-10 nm	-
T_p^0	initial particle temperature	1800-2800 K	-
T_g	gas temperature	723-1123 K	-
λ	detection wavelength	710 nm	-
h	Planck's constant	$6.63 \cdot 10^{-34} J.s^{-1}$	-
c	speed of light	$2.99 \cdot 10^{-10} cm.s^{-1}$	-
Cp_p	particle heat capacity	$800 J.kg^{-1}.K^{-1}$	$1.9 J.g^{-1}.K^{-1}$
α_T	energy accomodation coefficient	1	0.3
R	universal gas constant	$8.31 J.mol^{-1}.K^{-1}$	-
$\Omega(\lambda)$	spectral response of the system	1	-

The influences of some parameters on the TRL2I signal were both numerically and experimentally investigated. Hence, the variations

of the initial particle temperature (T_p) in the range between 1800 and 2800 K were found to be neglectable, while the surrounding gas temperature shows higher influence on the TRL2I signal decay time. In addition, the signal decay time increases with the detection wavelength, while it decreases with the laser fluence due to possible sublimation. Furthermore, for particle diameter smaller than 10 nm, the theoretically calculated TRLII signals of an iron spherical particle and a carbon spherical particle are almost exactely the same. Therefore, the model related to a single carbon spherical particle will be considered in the following. Moreover, if we assume a complete ferrocene pyrolysis, the estimated number of both iron and carbon atoms available in the gas phase are sufficient for the formation of either iron, carbon or iron/carbon clusters ranging from 1 to 10 nm. Therefore, as long as the measured NPs are smaller than 10 nm, there will be no influence from the actual chemical composition, meaning that no conclusive remarks can be drawn about the clusters' chemical composition.

Experimental procedure

For TRLII, an aperture (about 1.5 cm in height) was designed at the center of the high-temperature region without changing its temperature profile for the incident laser beam and the detection of the thermal particle emissions. The non-focalised 1064-nm light from a pulsed 2 Hz Nd:YAG laser (Excel, Surelite II-10) was operated with a pulse time of 7 ns and a beam diameter of 7 mm at less than 2 cm above the substrate for particle heat up. The pulse energy, recorded by an energy-meter was set up at 75 mJ per pulse, corresponding to a laser fluence of 0.2 J.cm^{-2}. At such laser fluence, the TRLII temporal profiles were found to be invariant with small variations in laser fluence. The optical detection system was composed of a narrow

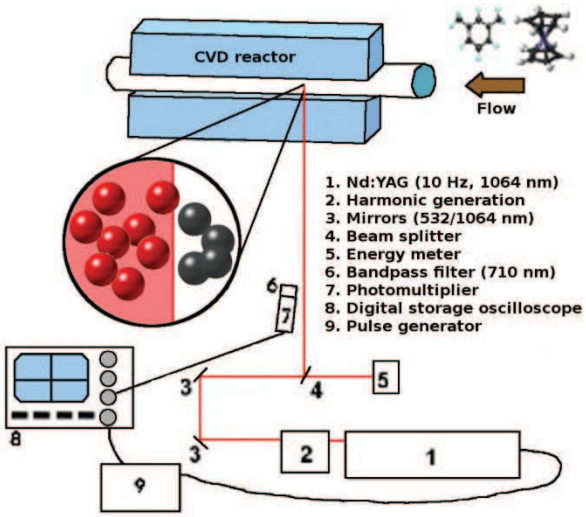

Figure 2.3.2: Schematic of the overall TRLII system.

band-pass filter with center-wavelength of 710 nm +/-10 to limit the radiation to a small spectral range and a high-speed photomultiplier with a separated amplifier (Hamamatsu, H6780-20 and C5594-44). The overall system is depicted in Fig 2.3.2. The signals were sampled by a 2 GHz digital storage oscilloscope (Lecroy, Wavejet 354A). A thousand individual time events were stored for each experiment.

Each individual time event was processed in the following way. At first, the maximum intensity of the signal was detected. This corresponds to the beginning of the cooling process. The time flag associated to this maximum was set at zero. The remaining temporal signal was adjusted with a single exponential decrease with 50 samples, representing 100 ns. Two algorithms were tested. The first was a simple linear fit on a logarithmic base, whereas the second was based on the Levenberg-Marquardt algorithm for minimization of a sum of squares of equation residuals [94] [108]. As no real differences were observed in the case of simple decay, in the remaining of the study, a lin-

ear fit was used to estimate the exponential decay of the TRLII signals.

A typical individual example illustrating the quality of the TRLII raw signals is given in Fig. 2.3.3a. The signal shows the photomultiplier output (continuous line) of the clusters suspended in the gas phase at the detection wavelength of 710 nm and a laser energy density of 0.2 J.cm^{-2}. Time zero is set at the start of the cooling down process, corresponding to the end of the laser pulse. The laser pulse caused sudden signal increase due to the particle heat-up. Then, the clusters radiate during cool down until the signal stabilizes to its initial value (i.e. before the laser pulse) after about 30 ns in case 1 and 50 ns in case 2. According to the model previsouly detailed (dashed lines in Fig. 2.3.3a), such decay times respectively correspond to cluster diameters of about 3 nm in case 1 and 5.5 nm in case 2. Case 1 and case 2 refer to two experiments performed under similar conditions (at 250°C vaporization temperature, 600°C growth temperature, 1 L.min^{-1} gas flow and 0.2 mL.min^{-1} injection speed) but with different ferrocene concentration (0.01 g.mL^{-1} for case 1 and 0.1 g.mL^{-1} for case 2).

In order to validate the applicability of the TRLII characterization method, almost simultaneously to the TRLII measurements, rapid particle sampling were performed in each case. A TEM-grid positioned on a holder was rapidly moved into the center of the high temperature region and removed after a short time, ensuring minimized heating of the grid and reduced disturbance. The sampled clusters were then visualized by HR-TEM. Representative examples of HR-TEM images obtained from the sampled clusters are shown in Fig. 2.3.3b for case 1 (bright field image) and in Fig. 2.3.3c for case 2 (dark field image). These observations confirm the particle spherical shape assumed in our model. Moreover, the HR-TEM investigations allow the evaluation of

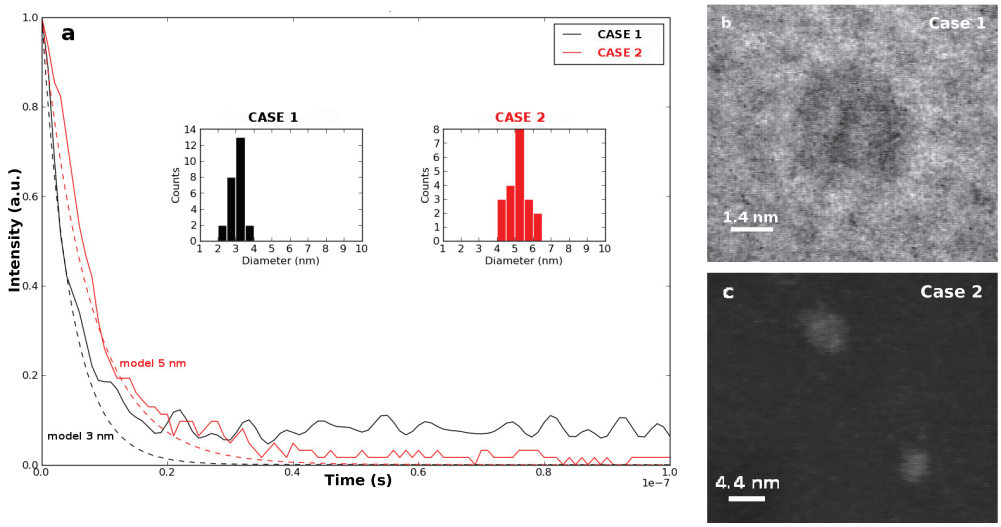

Figure 2.3.3: Typical experimental (continuous lines) and theoretical (dashed lines) TRLII signals of nanoparticles formed under similar conditions but with different ferrocene concentration (a). Representative high resolution TEM images of the corresponding nanoparticles (b-c).

the cluster size by counting and sizing them. The resulting histograms, depicted in the insets in Fig. 2.3.3a, were generated from several similar images and yield an average diameter with a narrow deviation of about 3.3 nm in case 1 and about 5.7 nm in case 2. The TRLII determined cluster size is in an excellent agreement with the HR-TEM measurements and can be therefore used for further *in situ* studies.

2.3.2 Laser induced breakdown spectroscopy

Principle

Laser-induced breakdown spectroscopy (LIBS) is an analytical technique that allows for the determination of samples elemental compositions. It is based on the sample laser ablation followed by ionic, atomic, and molecular emission processes coming from elements

transferred into the plasma as a result of laser-induced breakdown. A high power laser pulse, in the 1-10 MW/cm^2 range, is focused tightly on the targeted sample inducing dielectric breakdown leading to a plasma composed of elemental and molecular fragments originated from the sample and from the atmosphere in its immediate vicinity. During the early stages of the plasma development, the plasma temperature goes up to 10,000 to 25,000 K. At this temperature, the energy is sufficient to break molecular bonds to form constituent atoms and excite electrons of neutral atoms and ions into excited electronic states. All chemical bonds are broken resulting in highly excited, and unstable, atoms, ions and free electrons, resulting in a continuum emission. The continuum emission disappears quickly as the free electrons are absorbed by the atoms and ions in the plasma. As the plasma cools, characteristic photons are emitted as the excited ions and atoms stabilize, resulting in the formation the ionic and atomic emission lines of the elements, i.e. a spectrum. Each element has a unique spectrum of atomic and ionic emission lines. The emitted light from the laser-induced plasma can be collected and used to provide information on the elemental composition of the material by means of spectroscopy. However, absolute concentration determination by LIBS remains complicated because of the laser shot-to-shot variations. There are several key advantages to LIBS that can be beneficial for *in situ* on-line monitoring and diagnostic in hostile environments. LIBS is a non-contact, minimally destructive test, i.e. destroying an insignificant amount of particles.

Application to the detection of carbon and iron elements

The LIBS technique has been widely used to determine the carbon content of some soils or gases. One recent example of a LIBS system is

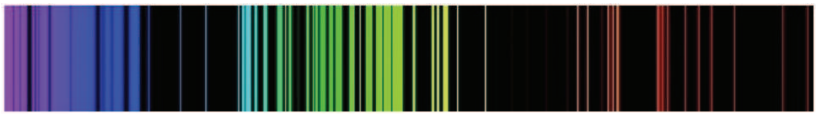

Figure 2.3.4: Emission spectrum of iron in the visible range. In total 4757 emission lines related to iron atomic emission were recorded between 200 and 1000 nm [NIST Atomic Spectra Database Lines].

the ChemCam equipment embedded in the NASA Curiosity robot for Mars exploration. In the case of carbon, the most frequently observed spectral lines are mainly in the UV at 247.9 nm or 248.4 nm. For instance, Martin et al [109] established a linear relationship between the emission intensity at 247.9 nm and the concentration of atomic carbon present in various soils. Although the spectral emission at 247.9 nm is commonly utilized to study carbon in solids or in gases, Ferioli et al [45] used the peak at 711.3 nm to characterize the levels of carbon in their system. Recently, carbon concentrations in the order of ten ppm were detected both in the UV at 193.1 nm [157] and in the IR at 833.52 nm [38]. For the rest of this research, the carbon emission peak at 711.3 nm will be considered (NIST Atomic Spectra Database Lines).

In the case of iron, the atomic emission is present over almost the entire spectral range from UV to IR, as depicted in Fig. 2.3.4. However, Martin et al. [109] found some interferences between the atomic emissions of iron and carbon at 248.4 nm. Moreover, an iron detection limit close to 10 ppm was achieved in the UV at 254.9 nm [38]. For the rest of this work, the iron emission peak at 404.5 nm will be studied.

Experimental procedure

In the same way as TRLII, an aperture (about 1.5 cm in height) was designed at the center of the high-temperature furnace without changing its temperature profile. A 10 Hz first harmonic laser beam (1064 nm) initiated by a Nd:YAG laser (Surelite II-10) was focused (f = 150 mm) at different positions on the quartz plate used as a substrate during the CNT synthesis by CVD. An energy meter was set up to control the laser fluence. The laser energy was about 500 mJ per shot before focalisation. The backscatterred signal was collected by a lens (f = 250 mm) directly to a spectrometer (CCS Thorlabs 200) for further analysis in the range between 200 and 900 nm. The acquisitions lasted for 10 ms and were synchronized with the laser pulse using a delay generator (Quantum Composers 9520 Series). Moreover, the effect of the angle between the incident laser beam and the substrate on the LIBS signal intensity was studied, while the detection position was kept constant. This factor shows a significant influence on the LIBS signal, as shown in Fig. 2.3.5. The LIBS signal intensity is maximal when the incident laser beam is normal to the substrate surface, while it increasingly decreases as the angle differs from 90°.

A representative example illustrating the quality of the LIBS spectra is given in Fig. 2.3.6. The signals show the spectrometer output of both pristine µ-Al_2O_3 deposited on the quartz plate into the CVD reactor before CNT growth (continuous line) and CNTs grown on µ-Al_2O_3 after 10 min CVD synthesis at 575°C (dashed line). While the LIBS signal of pristine µ-Al_2O_3 shows the emission lines of aluminium and oxygen, the signal detected after the CVD synthesis clearly exhibits new peaks related to the emission of carbon and iron. Hence, the iron/carbon ratio of the species deposited on the substrate surface

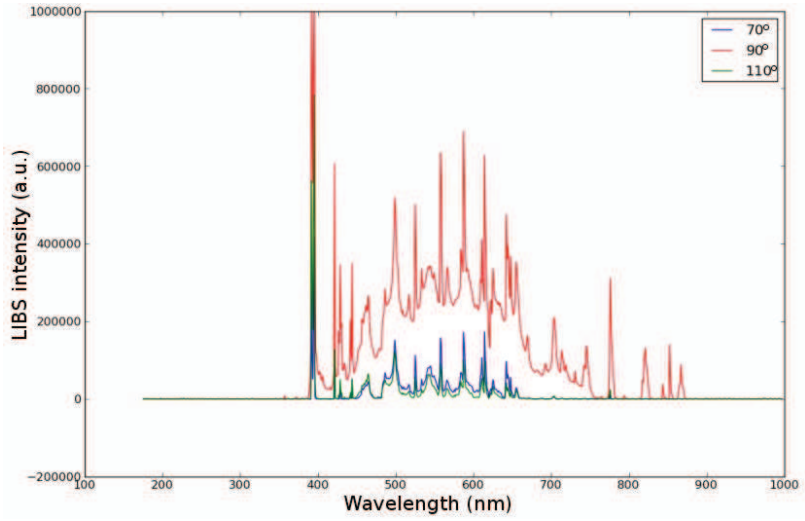

Figure 2.3.5: Influence of the angle between the incident laser beam and the substrate surface on the LIBS signal intensity averaged over 128 shots.

can be *in situ* and real-time determined by LIBS during the CVD process.

For calibration, the LIBS signals were correlated to the iron/carbon ratios determined by TGA of different samples synthesized under specific conditions. Five CNT arrays grown on quartz plates with different iron/carbon ratios were prepared and systematically analyzed by TGA and LIBS. The iron/carbon ratios determined by LIBS were plotted as a function of those measured by TGA. The LIBS iron/carbon ratios were obtained as follows: the ratios of the peak area at 711 nm (corresponding to CI emission) over that at 404 nm (referring to FeI emission) were calculated and averaged over 128 spectra. The resulting curve shown in Fig. 2.3.7 yields a linear correlation, validating the applicability of the LIBS method to *in situ* target the iron/carbon ratio during the CVD synthesis. This plot can be subsequently used for calibration.

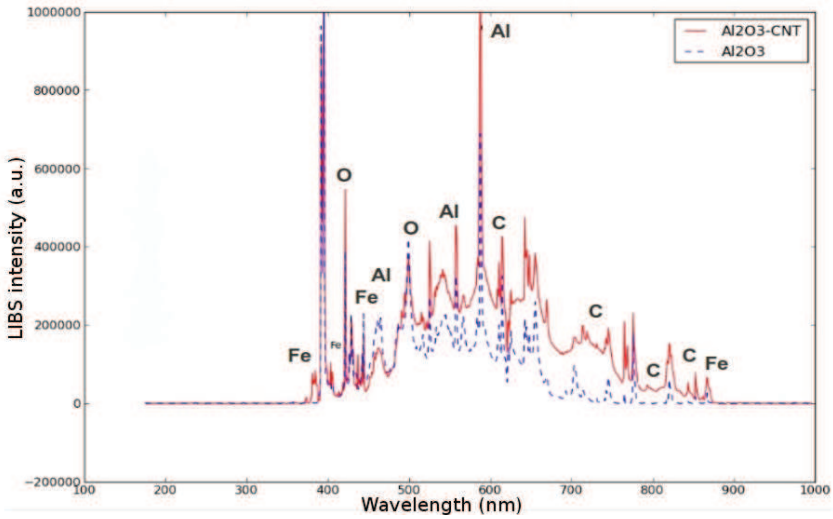

Figure 2.3.6: Typical *in situ* LIBS signals averaged over 128 shots of pristine μ-Al_2O_3 before (dashed line) and after (continuous line) CNT growth by 10 min CVD synthesis at 575°C.

Nevertheless, while LII can be considered as a fully non-intrusive technique, it is no longer the case for LIBS since the laser fluence and frequency involved are much higher. The plasma generated at the focal point induces new reactive species such as carbon atoms and radicals that can lead to new reactions during the CVD synthesis. Figure 2.3.8 illustrates the formation of carbon structures at the focal point on a quartz plate during CVD that would not occur without the mean of a laser beam. Indeed, no carbon formation can be usually reported at 350°C under typical floating catalyst CVD conditions as described in section 2.1, meaning that these carbon species actually arised from the plasma generated by the focused laser beam. Although such method can be interesting for growing CNT at low temperatures, we will not use LIBS for further real-time investigations. For instance, some methods recently reported the use of tightly focused laser beams for

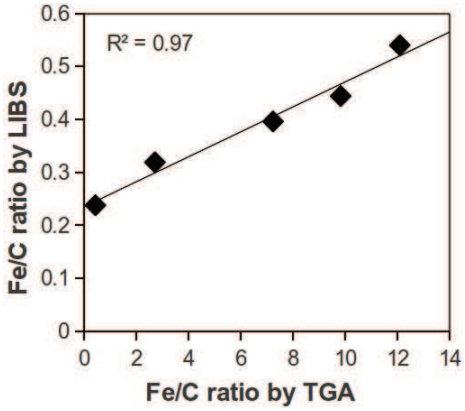

Figure 2.3.7: Iron/carbon ratio determined by LIBS as a function of that measured by TGA used for LIBS calibration. The TGA data give the amount of iron in wt.% calculated according to the equations in section 2.2.2.

the localised growth of CNTs. Such processes, known as laser-assisted CVD, involved different growth mechanism from typical thermal CVD that are closer to plasma-enhanced CVD. The presence of carbon atoms generated by the plasma allow CNT growth with a very low activation energy (about 0.3 eV) compared to that of thermal CVD (about 1.2 eV).

Figure 2.3.8: Formation of carbon structures after 10 min laser irradiation under typical floating catalyst conditions at 350°C.

To make sure that there is any plasma formation during the LII

analysis previously described, the spectra of the signals obtained both in LII and LIBS conditions were recorded. Figure 2.3.9 shows plasma induced atomic emissions in the case of LIBS characterized by distinct peaks in the spectra, while only continuous spectra was observed for LII, confirming that LII is a non-intrusive technique.

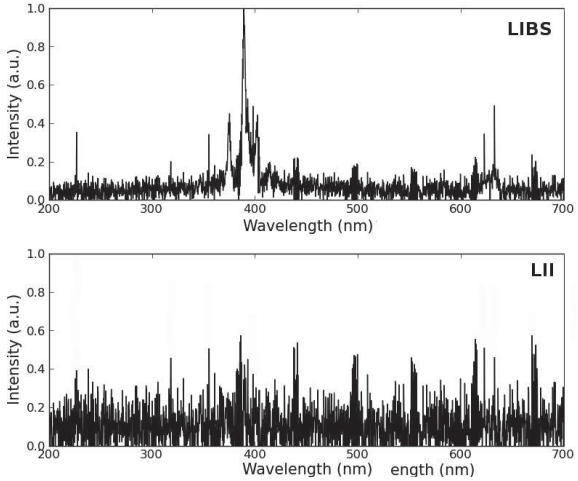

Figure 2.3.9: Comparaison of typical LIBS and LII single shot spectra in the range between 200 and 900 nm under similar CVD conditions.

2.3.3 Mass spectrometry couple with gas phase chromatography

Mass spectrometry coupled with gas phase chromatography was used to analyze the composition of the exhaust gas during the CNT synthesis by floating catalyst CVD. The mass spectrometer is composed of a quadrupole analyzer, a Faraday and a Channeltron sensors (Pfeiffer Vacuum GSD 301 Thermostar), while the chromatograph (Alpha MOS PR2100) consists of a thermal conductivity detector and a packed column using helium (He) as carrier. The exhaust gas was *in situ* captured

using a stainless steel capillary (length: 90 cm; inner diameter: 0.25 mm) which was drilled through a rubber plug set at the end of the reaction tube and kept well sealed. The gas sampling position was set up few centimeters above the substrate location at the centre of the reactor to analyse the gas in the CVD, avoiding the cooling down process. Each result presented in this research corresponds to an average of at least 3 measurements. The data were normalized as a function of the argon intensity. The analysis helped to understand the involved reactions in CNT growth and to developed a numerical model as detailed in Chapter 4.

Table 2.3.2: Mass spectrometry data of the main products related to this research from Pfeiffer Vacuum Spectra Library. The m/z peak ratios are given in the order of the decreasing relative intensities.

Product	Formula	N°peaks	m/z ratio
Acetylene	C_2H_2	8	26 25 13 24 27 12 14 28
O-xylene	C_8H_{10}	10	91 106 105 39 51 77 27 78 92 107
Toluene	C_7H_8	11	91 92 50 39 65 51 63 90 27 38 93
Benzene	C_6H_6	9	78 52 51 50 77 39 79 76 38
Argon	Ar	5	40 20 36 18 38
Water	H_2O	5	18 17 16 20 19

2.4 Summary

The table below summarizes the specifications of the vairous characterization techniques introduced in this Chapter.

The table below summarizes the studied parameters related to the CNT growth as a function of the different characterization techniques available.

Table 2.4.1: Listing of the different characterization methods and their specifications.

Techniques	Acquisitions	Resolutions	Comments
TRLII	decay time	[0-100] ns +/-6	*in situ*, real-time
LIBS	wavelength spectra	[200-1000] nm +/-2	*in situ*, intrusive
MS	mass spectra	[0-300] amu +/-0.3	*in situ*, real-time
GPC	elution time	[0-300] s +/-0.5	*in situ*, real-time
HRTEM	length	[2-100] nm	*ex situ*
TEM	length	[10-1.10^4] nm	*ex situ*
SEM	length	[15-5.10^6] nm	*ex situ*
Optical	length	[100-1.10^4] µm	*ex situ*

Table 2.4.2: Listing of the studied factors and the corresponding characterization techniques.

Measured factors	Available techniques
Reactor temperature	K type thermocouple
Droplet diameter	Optical microscopy after impact
$[C]/[Fe]$	LIBS and TGA
[gas phase species]	MS coupled with GPC
Suspended NP diameter	TRLII and HRTEM
Deposited NP diameter	HRTEM
CNT diameter	SEM, TEM and HRTEM
CNT length	SEM and TEM
CNT crystallization	Raman, TGA/DSC and SAED

Measure what is measurable, and make measurable what is not so.

Galileo Galilei

3

Catalyst nanoparticle nucleation in the gas phase

In this Chapter, the laser-based diagnostics introduced earlier are used to *in situ* study the nanoparticle formation and follow their spatio-temporal evolution in the CVD gas phase. Two possible mechanisms are first suggested based on the comparison between the droplets diameter and that of the NPs and the CNTs. Then, the Taguchi robust design approach is proposed to study the influence of seven key CVD parameters on the suspended NP size in the gas phase. Finally, the relationship between the suspended NP size in the gas phase and the resulting CNT diameter is examined and its effect on the growth mechanism is discussed.

3.1 The very first stage of the synthesis

3.1.1 Evolution of the droplets in the CVD reactor

As detailed in chapter 2, the CNT precursors were introduced into the CVD reactor in the form of spray via a cross-flow injection system. The resulting droplets can be considered as the very first CNT precursors. A study of their features would therefore help to understand the CNT growth mechanism. First, the droplet size distribution at the injector outlet was found to be nearly constant with the catalyst concentration, as depicted in Fig. 2.1.3. A similar bimodal population of droplets was observed for the different concentrations. This bimodal size distribution will necessary induce a gradient in the droplets speed, subsequently leading to coalescence since new droplets are continuously injected. The evolution of the droplet size in the CVD reactor was investigated at room temperature and atmospheric pressure. The injection conditions were kept constant during this study. Argon was fed at 1 L/min, while 0.01 g/mL ferrocene/xylene solution was provided in the reactor at 0.2 mL/min. The droplets were impacted on small quartz plates located at different positions in the CVD reactor for further optical microscopy observations. Figure 3.1.1 shows the resulting droplet size distributions as a function of the reactor position.

Compared to the droplet size distribution at 2 cm after the injector outlet illustrated in Chapter 2, that at 4 cm exhibits a slight increase of the droplet mean diameter while the bimodal distribution is conserved. The increase of the droplets size becomes larger at the end of the spray expansion (i.e. the distance when the spray reaches the reactor wall), corresponding to about 8 cm after the injector outlet. Hence, the smaller population of droplets reached about 275µm diam-

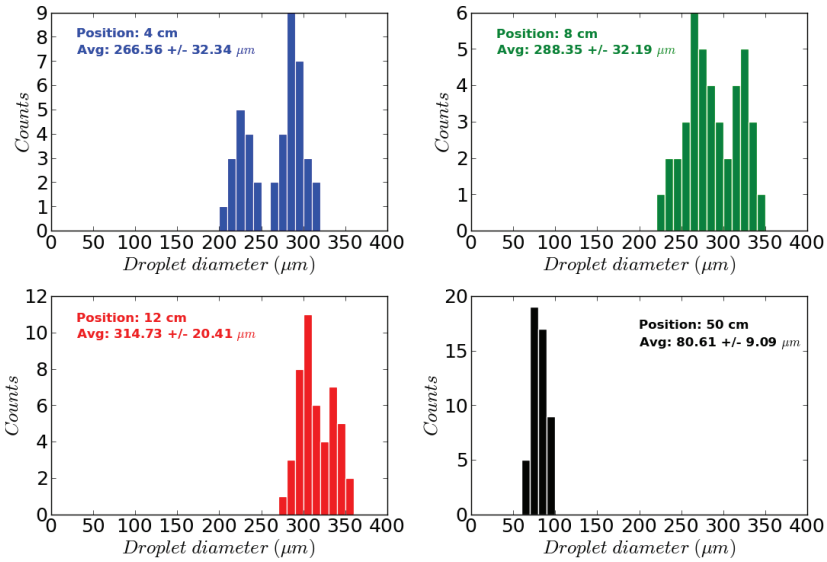

Figure 3.1.1: Evolution of the droplet size distribution at 0.01 g/mL ferrocene/xylene as a function of the position in the CVD reactor.

eter, while the larger one increased up to 325µm diameter in average, as depicted in Fig. 3.1.1. The droplets keep expanding further, thus confirming the coalescence suggested earlier. Nevertheless, at 12 cm after the injection outlet, corresponding to the beginning of the high temperature furnace, the two populations of droplets disappeared to form a broad monomodal distribution with a mean diameter of 315 µm. These droplets can be considered as the final CNT precursors before the CVD reactions in the high temperature furnace zone. After this position, the droplets monomodal distribution remains and its size decreases as the position gets farther from the injector outlet, as illustrated in Fig. 3.1.1. This decrease in size is due to the droplet evaporation which is not fully complete at room temperature, but must be total at higher temperatures.

3.1.2 Nucleation and evolution of the nanoparticles

The nanoparticle formation is still an open issue. In the case of floating catalyst using a spray aerosol injection, two mechanisms have been proposed [129] [122]. Either the catalyst NPs form by xylene evaporation and further precipitation of ferrocene as described in Fig. 3.1.2a, or the condensation and clustering of iron/carbon vapor originated from the precursors decomposition leads to NPs formation as illustrated in Fig. 3.1.2b.

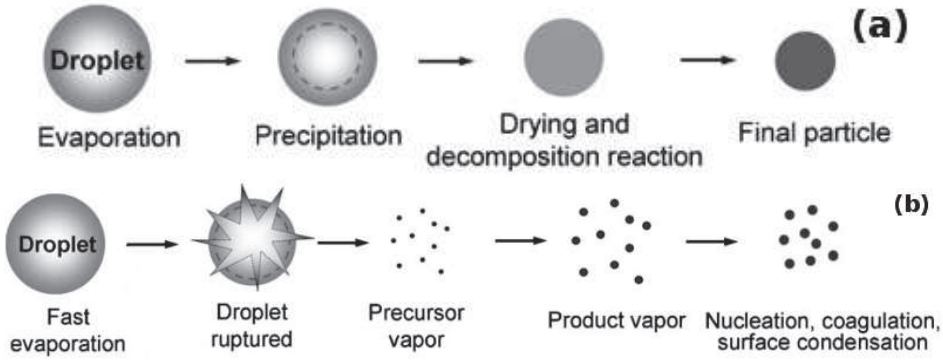

Figure 3.1.2: Schematics showing different nanoparticle formation mechanisms (a) by evaporation and precipitation of droplets, or (b) by condensation and coagulation of the vapor phase species [129].

3.1.3 Evaporation and precipitation mechanism

As previously mentioned, the injected droplets can be seen as the very first CNT precursors. Although the formation of NPs remains an open question, it is obvious that the droplet size is a critical factor that can change the CNT structure no matter the growth mechanism involved. Elguezabal et al. [2] reported that the diameter of MWNTs was significantly influenced by droplet size, while the CNT length was

controlled by the carrier gas flow rate. In our case, a way to tune the droplet size while keeping the gas flow constant would be to change the design of the injector. For instance, the use of different capillary diameters for the injection of liquid and gas was found to dramatically change the droplet size and the spray angle, as shown in Maxime Genestoux PhD thesis. However, this will also change the precursors speed and subsequently their residence time in the CVD reactor.

However, we propose a different approach to investigate the formation of NPs and their evolution in the CVD reactor before the CNT growth. For a given droplet size, different ferrocene concentrations should induce different NP sizes and densities independently from the mechanism involved in the NP formation shown in Fig. 3.1.2. Hence, various samples were prepared under similar CVD conditions but for different ferrocene concentrations. The temperature was set at 750°C, the gas flow rate was 1 L/min, while the liquid flow rate was 0.2 mL/min. Ferrocene/xylene solutions at different concentrations ranging from 0.005 to 0.1 g/mL were sprayed and carried into the CVD reactor by a mixture of argon and hydrogen (H_2 20 vol.%). No other chemical species was fed in the reactor. The injection lasted for 7 min before the furnace was cooled down. The resulting CNT samples were collected on a 3 cm quartz plate at the center of reactor for further examinations. Figure 3.1.3 shows representative SEM and TEM images of the CNT arrays produced with 0.005 g/mL of ferrocene/xylene.

Since several catalyst NPs were found encapsulated at the extremities of some nanotubes, we can assume that the CNT diameter is related to the NP size (see section 3.3). Therefore, the electron microscopy observations allow the evaluation of the NP size by counting

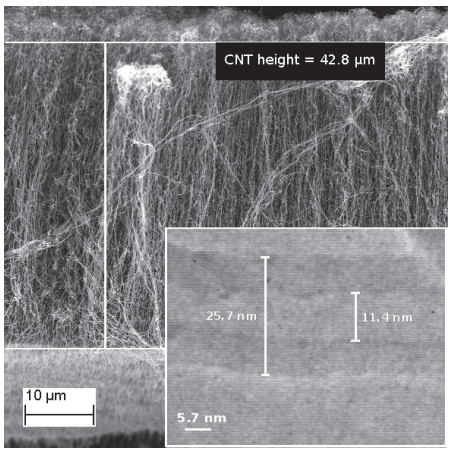

Figure 3.1.3: Representative SEM and TEM images of the CNT arrays produced for 0.005 g/mL of ferrocene/xylene during 7 min at 750°C under a mixture of Ar and H_2 (20 vol.%) fed at 1 L/min.

and sizing the CNT diameters. The resulting size distributions at different catalyst concentrations up to 0.3 g/mL are represented in Fig. 3.1.4.

The variations of ferrocene concentrations in the [0.005-0.2] g/mL range always lead to monomodal CNT diameter distributions. The CNT mean diameter increased with the catalyst concentration, while the distribution was broaden. For instance, the average CNT diameter was about 33.7, 38.6, 49.5 and 63.2 nm at 0.005, 0.0075, 0.01 and 0.02 g/mL, respectively. Since the droplet size is assumed to be constant for all experiments (Chapter 2 revealed that the droplets size is quite independent from the catalyst concentration) while xylene should completely evaporate under such conditions, it therefore means that the catalyst concentration plays a significant role in the CNT growth mechanism by controling the size of the NPs. Moreover, the droplets exhibit a monomodal distribution before reaching the high temperature furnace, as well as the collected CNTs synthesized in the concentration

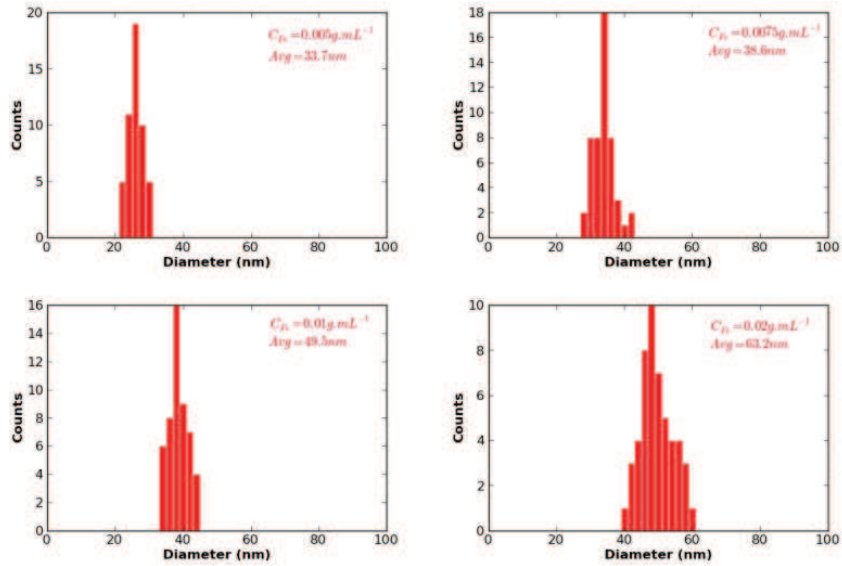

Figure 3.1.4: CNT outer diameter distribution as a function of the catalyst concentration ranging between 0.005 and 0.02 g/mL at 750°C under a mixture of Ar and H_2 (20 vol.%) fed at 1 L/min.

range [0.005-0.2] g/mL. A relation between the droplet size, the NPs and subsequently the CNT diameter would be possible. If one imagines that the NP formation follows the evaporation and precipitation process depicted in Fig. 3.1.2a, then one can assume that one droplet may lead to one NP. In this case, the NP size would depend on the evaporation rate of the solvent (i.e. xylene), which remains constant under the same conditions, and the concentration of the solute (i.e. ferrocene), explaining the data from Fig. 3.1.4. Hence, since the amount of Fe in the droplet must be the same as that in the NP, the NP diameter, d_p, could be expressed as a function of the droplet size, d_d and the volume fraction of ferrocene, F, as follows:

$$d_p = d_d \cdot \sqrt[3]{F}\,;\; where\, F = \frac{M_{Fe} \cdot C_{ferrocene}}{\rho_{Fe}}$$

In order to further study the evolution of the NPs in the CVD gas

phase by *in situ* TRLII, a solution of 0.01 g/mL ferrocene/xylene was injected at 0.2 mL/min and carried by argon at 1 L/min in the reactor heated up at 650°C. The NP size was examined *in situ* and in real-time by TRLII at different positions along the reactor (see Fig. 3.1.5)

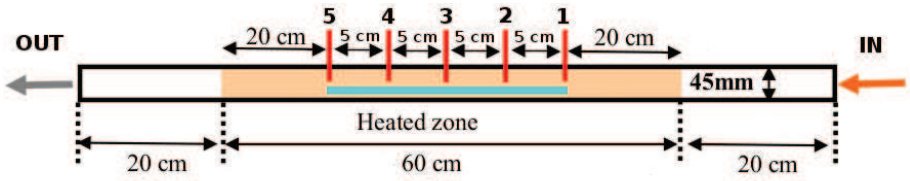

Figure 3.1.5: Schematic of the CVD reactor with the different positions where *in situ* TRLII analysis were performed.

Figure 3.1.6 shows the temporal evolution of the TRLII decay times (which are correlated to the NP sizes as detailed in Chapter 2) as a function of the positions in the CVD reactor. Apart from the first hundred seconds needed for the system stabilization after the injection, the NP size was quite constant in time for a given position. This indicates that the continuous injection process can actually be assimilated as a succession of independent waves of NPs. However, if the NP size gradient in one wave becomes large enough to induce sufficient difference of speed between the smaller and the bigger NPs, interactions between several waves would be therefore possible, leading to the agglomeration of the NPs.

Furthermore, the mean NPs diameter was found to decrease as the NPs get farer from the injector outlet, as depicted in Fig. 3.1.7a. The mean diameter of the NPs at the positions 1, 2, 3, 4 and 5 were 2.8, 2.5, 2.2, 1.7 and 1.2 nm, respectively. The bigger NPs were found closer to the injector outlet, indicating a possible evaporation and precipitation

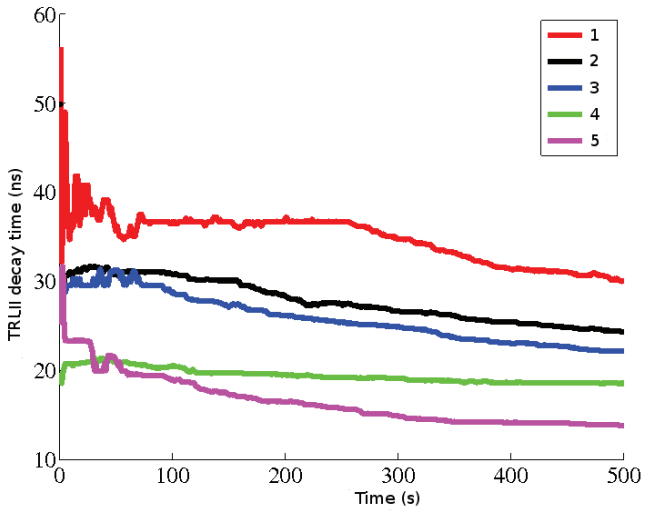

Figure 3.1.6: Temporal evolution of the TRLII decay times (which are correlated to the NP sizes as detailed in Chapter 2) as a function of the positions in the CVD reactor at 650°and 0.01 g/mL of ferrocene.

mechanism for the NP formation, as already suggested earlier. The reactor temperature gradient coupled with a few seconds residence time may induce the decrease of the NP size along the CVD according to the evaporation and precipitation mechanism. However, the NPs size detected in the gas phase are far from reaching that measured on the substrate, revealing the important role played by the substrate. This point will be discussed later in this research. In addition, the first and the last positions corresponding to the edges of the quartz plate (see Fig. 3.1.5) exhibit the highest standard deviations (see Fig. 3.1.7), which may indicate turbulences in the gas flow at these positions. Nevertheless, since the NP size remains constant in time as shown in Fig. 3.1.6, it means that there is no gas recirculation in the reactor. Moreover, the amount of Fe detected by LIBS on the quartz plate after the injection follows the same trend as the NP size, as illustrated in Fig. 3.1.7b. In this case, the injection was lasted longer than the TRLII analysis to allow sufficient deposition of products

on the quartz plate to be detected by LIBS. According to the LIBS calibration in Chapter 2, about 2.5, 1.2 and 0.5 wt.% of Fe were estimated at position 1, 3 and 5, respectively. Therefore, it indicates that there is a possible relation between the NP size and the amount of Fe deposited on the quartz plate along the CVD reactor.

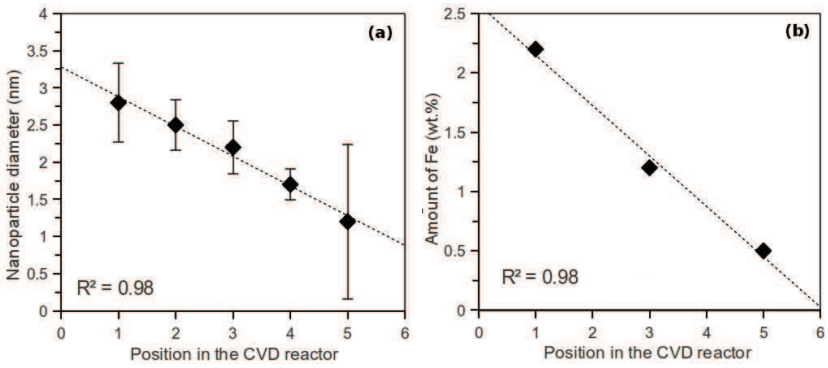

Figure 3.1.7: NP size *in situ* detected by TRLII in the CVD gas hase as a function of the position in the reactor at 650°C and 0.01 g/mL of ferrocene (a). Amount of Fe measured 15 min after the CVD synthesis by LIBS as a function of the position in the reactor under similar conditions (b).

3.1.4 Condensation or agglomeration mechanism

If the catalyst concentration increased further under the same CVD conditions as previously described, a second and even a third mode appear in the CNT diameter distribution, as depicted in Fig. 3.1.8. Similar multimodal distributions were also reported by Ionescu et al. [71] by hydrogen-free floating CVD. Considering that the CNT diameter is related to the NP diameter on the substrate, one may assume that the NPs deposited on the substrate also exhibit similar multimodal distributions.

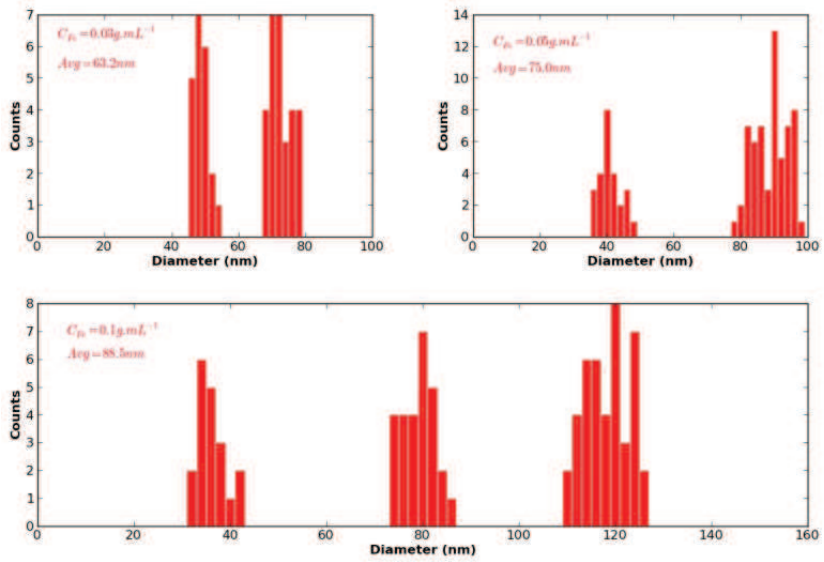

Figure 3.1.8: CNT outer diameter distribution as a function of the catalyst concentration ranging between 0.05 and 0.1 g/mL at 750°C under a mixture of Ar and H_2 (20 vol.%) fed at 1 L/min.

Since the CVD conditions were the same apart for the catalyst concentration, it indicates that the temperature gradient, the residence time and the size distribution of the precursor droplets did not change. Therefore, it means that a different mechanism is involved in the NP formation and evolution at higher catalyst concentration (above 0.3 g/mL). Moreover, if we use the expression given earlier between the NP size and the catalyst concentration based on the evaporation and precipitation process to fit the experimental results, two different modes can be clearly identified, as shown in Fig. 3.1.9. Catalyst concentrations ranging from 0.02 to 0.03 g/mL seem to be the limit between these two modes. Below this limit, the NP size is in a good agreement with the "one drop one particle" model, revealing that the NP formation might follow the evaporation and precipitation mechanism. Above the limit, new populations of NPs appear, as illustrated by the increase of the standard deviation in Fig. 3.1.9, and

the "one drop one particle" model does not suit to the experimental values anymore. Therefore, under given CVD conditions, the catalyst concentration influences the NP formation process and thus the CNT growth.

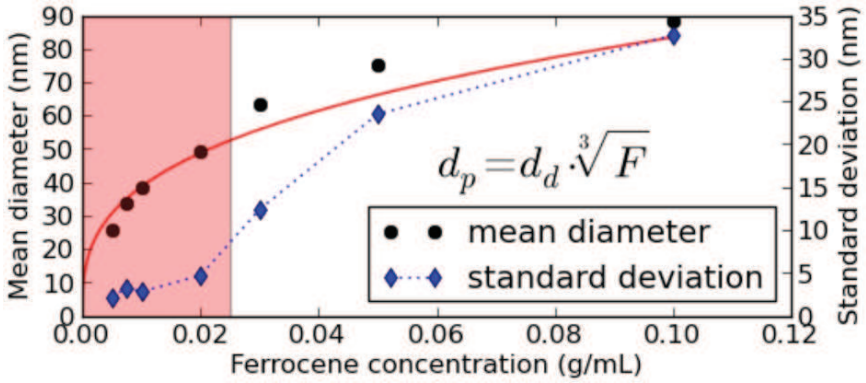

Figure 3.1.9: CNT mean outer diameter and standard deviation as a function of the catalyst concentration at 750°C under a mixture of Ar and H_2 (20 vol.%) fed at 1 L/min.

Besides its effect on the catalyst NPs formation, the catalyst concentration also influences the CNT growth kinetics. Figure 3.1.10 shows representative SEM and TEM images of CNT arrays produced at 0.1 g/mL of ferrocene/xylene under the same conditions as reported for the growth of CNTs presented in Fig. 3.1.3. The reaction time being the same in each case, hence higher concentrations induce faster growth rates. The CNT growth kinetics and the effect of various CVD factors will be discussed in more details in Chapter 6.

Furthermore, the evolution of the NPs formed at the [0.03-0.1] g/mL concentration range in the CVD reactor was investigated by *in situ* TRLII. A solution of 0.05 g/mL ferrocene/xylene was injected at 0.2

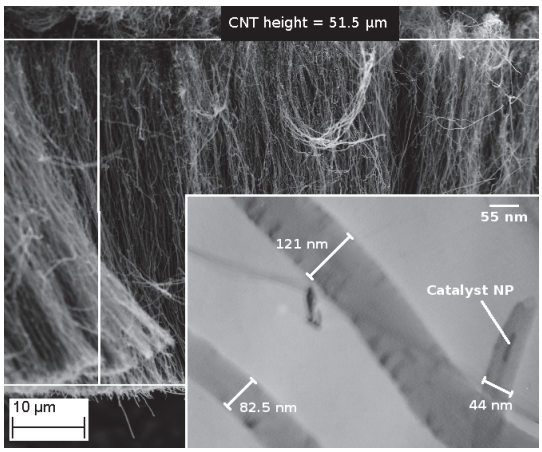

Figure 3.1.10: Representative SEM and TEM images of the CNT arrays produced for 0.1 g/mL of ferrocene/xylene at 750°C under a mixture of Ar and H_2 (20 vol.%) fed at 1 L/min.

mL/min and carried by argon at 1 L/min in the reactor heated up at 650°C. First, in the same way as for lower catalyst concentrations, higher standard deviations were found at the edges of the quartz plate, indicating that the turbulences in the gas flow are inherent to our CVD system. Nevertheless, the evolution of the NP size along the CVD reactor exhibits an opposite trend with that of the NPs formed at lower catalyst concentrations. Figure 3.1.11a shows that the mean NPs diameter increases as the NPs get farther from the injector outlet. The mean diameter of the NPs at the positions 1, 2, 3, 4 and 5 were 1.0, 1.3, 1.3, 1.5 and 1.7 nm, respectively. Moreover, the amount of Fe detected on the quartz plate by LIBS at the end of the experiment still increases along the reactor position, as depicted in Fig. 3.1.11b. The amount of Fe on the quartz plate is no longer related to the NP size in the gas phase, suggesting that the NP density is higher at the begining of the CVD reactor. The opposite variations of the NP size and density in the CVD gas phase may reveal the possible agglomeration of NPs which would explain the multimodal distribution observed in the

resulting CNT diameter. This will be discussed further in Chapter 4.

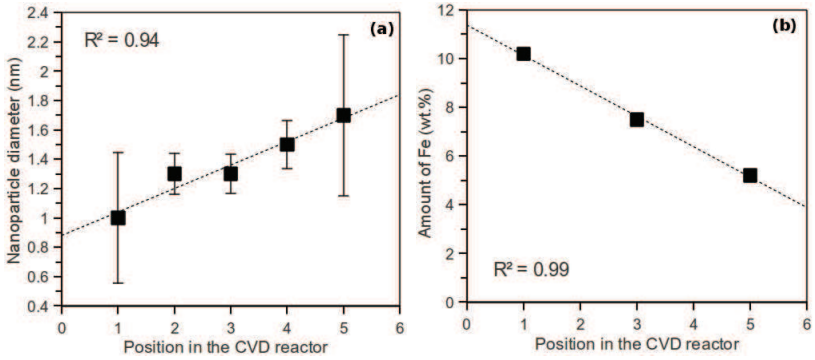

Figure 3.1.11: NP size *in situ* detected by TRLII in the CVD gas phase as a function of the position in the reactor at 650°C and 0.05 g/mL ferrocene/xylene (a). Amount of Fe measured after the synthesis by LIBS as a function of the position in the reactor (b).

3.2 How to control the nanoparticle size with the CVD conditions?

The continuous synthesis of specific types of CNTs with distinct structure and diameter for large scale production remains one of the principal and challenging goals. According to several authors [19], [74] a key parameter is the control of the catalyst NP size. Although a good monitoring of the NP size can be achieved by pre-deposited catalyst CVD methods using lithography [39] or catalyst pre-treatments [113], [124] it is still very difficult to do the same with aerosol-assisted CVD for mass production. It requires the ability to *in situ* monitor the NP size during the CNT growth from their migration and possible agglomeration in the gas phase to the CNT nucleation and growth on the substrate. While TEM observations focus on one particular event on a substrate, *in situ* TRLII provides insightful informations from

the gas phase.

Up to now, a limited control of the catalytic NP size and thus of the CNT diameter under typical aerosol-assited CVD has been reported by empirically tuning experimental factors [103], which is not surprising as the number of variables involved in the synthesis (e.g. temperature, pressure, feedstock and substrate chemical composition, catalyst injection...) is large. Hence, the analyses using conventional experimental techniques are inefficient. Therefore, the well-known Taguchi robust design method was introduced as a powerful and efficient tool for multifactor process optimization [161]. A systematic TRLII study of the influence of the FCCVD parameters on the particle size in the gas phase based on the Taguchi approach was performed.

A set of experiments was designed to investigate the most influential CVD parameters in the cluster size. Seven control factors with two levels were examined, leading to eight experiments organized in a L8 Taguchi matrix design. The seven parameters that were investigated were (i) the growh-temperature (600 and 650°C), (ii) the vaporization-temperature (room temperature and 250°C), (iii) the total gas flow (1 and 2 L.min^{-1}), (iv) the injection speed (0.1 and 0.2 mL.min^{-1}), (v) the ferrocene concentration (0.01 and 0.03 g.mL^{-1}), (vi) the substrate type (quartz plate and a powder composed of silicon carbide micro-platelets) and (vii) the hydrogen volume ratio (0 and 10 vol.%). Subsequently, the cluster size detected in the gas phase by TRLII was selected as the output response. The reaction time was kept constant for any of the Taguchi-designed experiment. The record of the TRLII signals was limited to the first 4 min of the CVD synthesis to keep the reactor wall sufficiently transparent for reliable TRLII analysis. Under this condition, the detected TRLII signals unambiguously correspond to the precursors' injection. The larger-is-better response showed in Eq.

(3.1) and the smaller-is-better response indicated in Eq. (3.2) were adopted for further analysis.

$$S/N_{larger} = -10log_{10}(\frac{1}{n}\sum\frac{1}{Y_i^2}) \tag{3.1}$$

$$S/N_{smaller} = -10log_{10}(\frac{1}{n}\sum Y_i^2) \tag{3.2}$$

S/N indicates the signal to noise ratio statistic used in the Taguchi parameter analysis, n is the number of levels in which each parameter was investigated and Y_i the ith value of the output response used for the evaluation. The Taguchi robust design and the corresponding results are summarized in the table below.

L_8	Substrate	T_2 (°C)	Ferrocene concentration (g.ml^{-1})	T_1 (°C)	Injection speed (ml.min^{-1})	Gas flow (l.min^{-1})	Hydrogen (vol.%)	Decay time (ns)	Diameter (nm)
1	Quartz	600	0.01	RT*	0.2	1	0	30.2	2.9
2	Quartz	600	0.01	250	0.4	2	10	15.0	1.5
3	Quartz	650	0.03	RT*	0.2	2	10	22.0	1.9
4	Quartz	650	0.03	250	0.4	1	0	13.4	1.3
5	SiC	600	0.03	RT*	0.4	1	10	14.1	1.4
6	SiC	600	0.03	250	0.2	2	0	28.0	2.7
7	SiC	650	0.01	RT*	0.4	2	0	27.2	2.5
8	SiC	650	0.01	250	0.2	1	10	35.8	3.3

Figure 3.2.1: Taguchi parameter design and results of the CVD experiments. *RT stands for room temperature

Strong changes in the TRLII decay time (i.e. in the cluster size in the gas-phase) were obtained by carrying out any of the Taguchi-designed experiment of Table 1. For each experiment, thousand TRLII signals were stored and computed as previsouly detailed. The results are summarized in Fig. 3.2.2, which shows the response graphs of the S/N ratios for the larger-is-better analysis (Fig. 3.2.2a) and for the smaller-is-better analysis (Fig. 3.2.2b) of the TRLII decay time (i.e. the cluster size) evaluations. The greatest variation of the S/N ratio was observed in each case with both the injection speed and the ferrocene concentration, revealing that these parameters have the

most important influence on the particle size. The other factors, like the total gas flow, the vaporization and the growth temperatures, the substrate's type and the hydrogen ratio show a secondary effect on the cluster size.

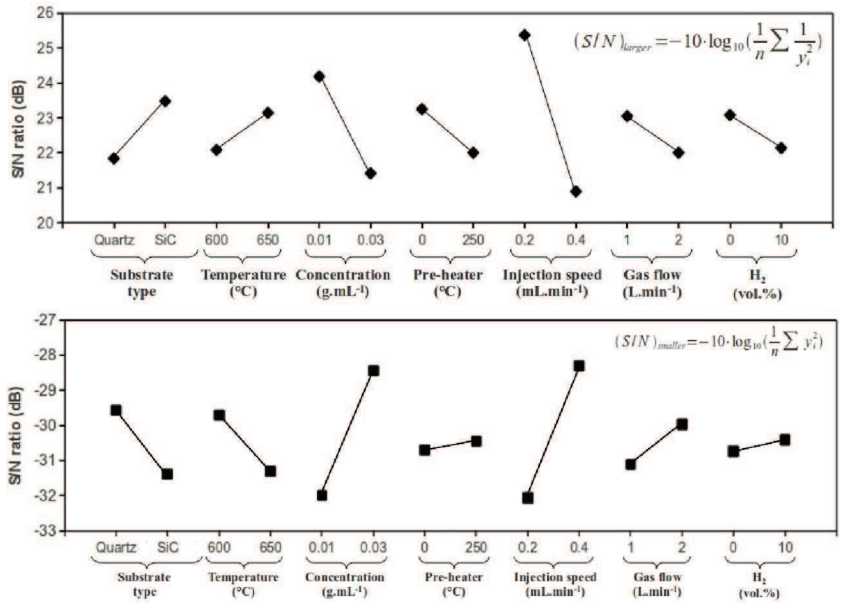

Figure 3.2.2: Response graph of *S/N* ratio for larger-is-better (a) and smaller-is-better analysis (b) of the NP size detected in the gas phase by *in situ* TRLII.

The larger-is-better analysis of the TRLII decay time (i.e. the cluster diameter) evaluation graph shows that the bigger clusters in the gas phase can be obtained at 650°C growth temperature, 1 L.min^{-1} total gas flow, 0.01 g.mL^{-1} catalyst concentration, 0.2 mL.min^{-1} injection speed and SiC micro-platelets used as a substrate, as depicted in Fig. 3.2.2a. The suspended cluster size can be increased further by enlarging the range of the Taguchi study. Reversely, the smaller clusters in the gas phase can be produced at 250°C vaporization temperature, 600°C growth temperature, 2 L.min^{-1} total gas flow,

0.03 g.mL^{-1} ferrocene concentration, 0.4 mL.min^{-1} injection speed, 10 vol.% hydrogen ratio and with a quartz plate used as a substrate, as described in Fig. 3.2.2b. Moreover, the conditions and the values of these optimized cluster sizes predicted by the Taguchi robust design are summarized in the table below. Hence, the smaller clusters' decay time is expected to be about 6.1 ns (i.e. corresonding to a NP diameter of about 0.7 nm), while the bigger clusters' decay time is expected to reach 39.2 ns (i.e. 3.7 nm). Repeating these particular experiments verified the applicability of the Taguchi analysis. Indeed, Fig. 3.2.3 depicting the experimental decay times over 500 TRLII signals of the clusters from the optimized configurations, confirms the predicted values. The smaller cluster decay time was found to be 8.5 ns in average (i.e. corresponding to a NP diameter of about 0.9 nm), while the bigger one was about 38.4 ns in average (i.e. 3.7 nm). The experimental TRLII signals for the optimized configurations are in an excellent agreement with the values predicted by the Taguchi method.

Table 3.2.1: Summary of the larger and smaller optimized conditions.

	Substrate	T_2	Concentration	T_1	Liquid flow	Gas flow	H_2
Larger	SiC	650°C	0.01 g/mL	RT	0.2 mL/min	1 L/min	0 vol.%
Smaller	Quartz	600°C	0.03 g/mL	250°C	0.04 mL/min	2 L/min	10 vol.%

3.3 Relations with the CNT growth

The "smaller" and "larger" optimized experiments previously described were last longer to allow the growth of CNTs. After 20 min under the same optimal conditions previously reported, sufficient CNTs were collected for further *ex situ* analysis. Fig. 3.3.1 shows representative electron microscopy images and the CNT outer diameter distributions of both CNTs grown under the "smaller" optimized

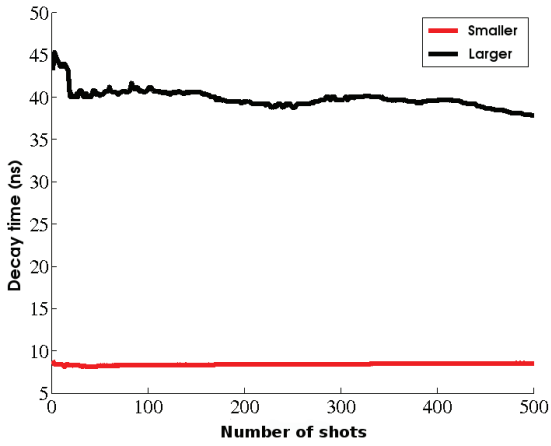

Figure 3.2.3: Representative TRLII signals for the smaller (in red) and the larger (in black) conditions according to the Taguchi robust design. The TRLII signals originate from a series of 500 signals stored at a sampling rate of 2 shots/second corresponding to a CVD synthesis of about 4 min.

conditions (Fig. 3.3.1a) and CNTs synthesized under the "larger" optimized process (Fig. 3.3.1b). The estimated mean diameter of the particle size in the gas phase was 0.9 nm for the "smaller" conditions and 3.7 nm for the "larger" ones, respectively leading to CNT with an average outer diameter of 12.2 and 41.0 nm. Although the NPs originated from the gas phase are much smaller that the resulting CNTs, the CNTs from the "larger" optimized experiment are significantly bigger than the ones from the "smaller" optimized experiment. This suggests a possible link between the suspended NP size and the CNT diameter. Since, the Taguchi experiments number 1, 2 and 5 induced intermediate particle sizes in the gas phase (2.9, 1.5 and 1.4 nm respectively), they were last longer for further *ex situ* analysis. The resulting CNTs also showed intermediate outer diameters about 30.5, 16.5 and 15.3 nm for the Taguchi experiment number 1, 2 and 5 respectively. The CNT diameter distributions with representative SEM images of these samples are shown below. The figures entitled (c), (d) and (e) respectively correspond to the CNTs

grown under the Taguchi designed conditions 1, 2 and 5.

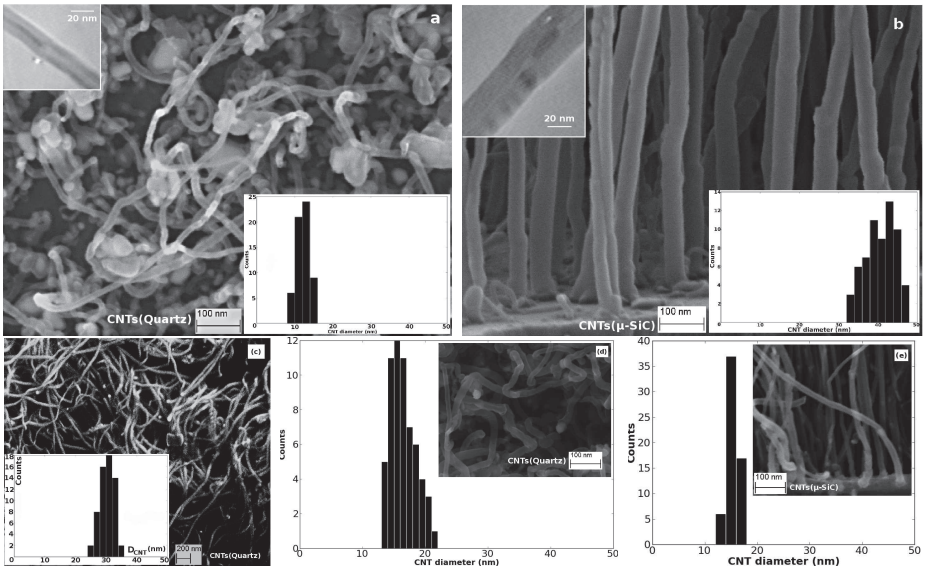

Figure 3.3.1: Electron microscopy images and diameter distribution of the resulting CNTs grown under the smaller (a) and the larger (b) conditions. The images presented in (c), (d) and (e) correspond to CNTs grown under the Taguchi conditions 1, 2 and 5, respectively.

The evolution of the particle sizes *in situ* detected in the gas phase with the corresponding *ex situ* measured CNT diameters plotted in Fig. 3.3.2 yields a linear correlation ($R^2 = 0.978$). It means that there is a direct relationship between the NPs formed in the gas phase and the CNT growth. Therefore, TRLII diagnostic can serve as a powerful tool to *in situ* monitor the final CNT structure.

However, the suspended NPs being about ten times smaller than the resulting CNTs, it reveals that further reactions must occur. Since the cluster size detected in the gas phase was found to almost remain constant during the FCCVD synthesis as depicted in Fig.

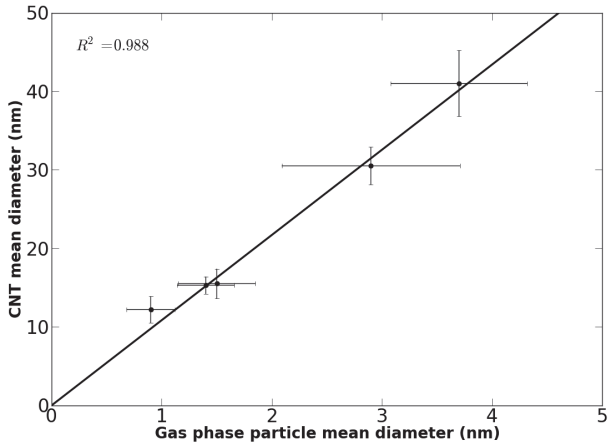

Figure 3.3.2: Evolution of the resulting CNT diameter determined by *ex situ* electron microscopy with the nanoparticle size detected by *in situ* TRLII.

3.2.3, it is believed that further reactions will happen on the substrate surface. Two different mechanisms were proposed. In one hand, the NPs might coalesce on the substrate via surface diffusion or Ostwald ripening [145]. For instance, some substrates are known to restrict the catalyst mobility and thus prevent NPs to coalesce [110], while others with high surface tensions such as tantalum, allow the formation of a catalytic wetting layer [171]. The CNT nucleation will eventually occur via the adsorption, diffusion and precipation of carbon through the catalyst NPs. Then, the growth will follow either a perpendicular or a tangential configuration as recently detailed elsewhere [46]. In the tangential configuration, the resulting CNTs have a diameter close to that of its seeding particle, while in the perpendicular one the NP size on the substrate and the resulting CNT diameter are no longer related. In our case the CNTs are believed to grow via the tangential configuration, and several NPs were found encapsulated inside the CNT core (see Fig. 3.3.3). In the other hand, the difference in size between the NPs and the resulting CNT diameter may be explained by the particle-wire-tube mechanism [36]. The NPs will self-assembly

into nanowires due to the strong anisotropy of their structure. The as-formed nanowires will then empty into tubular structures via structural crystallization and extension due to the relatively low stability of the NPs under thermal annealing. Although the CNT growth mechanism remains an open issue, the main factor for the control of CNT diameter is, in each case, the size of the incipiently formed NPs, which depends on the synthesis conditions.

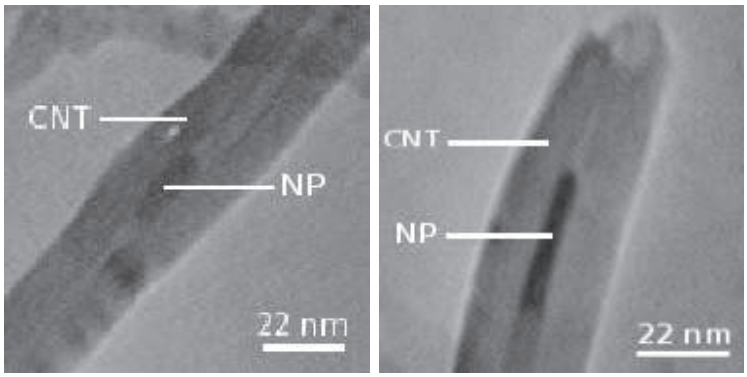

Figure 3.3.3: TEM images showing catalyst NPs encaspulated inside the core of CNTs after CVD synthesis under the conditions reported for the Taguchi experiment 1 (a) and 1 (b).

Finally, the particle size will not only influence the CNT structure and its resulting properties, but it will also affect the growth kinetics. The solubility, S, in a spherical iron particle with radius r can be expressed by $S = S_0 exp(\frac{2\sigma V}{k_B T r})$, where S_0 is the solubility of the bulk material, σ is the surface tension, V is the volume of metal molecule, k_B is the Boltzmann constant and T is the melting temperature in bulk phase [85] [117]. Figure 3.3.4 shows that the carbon solubility in a catalyst NP dramatically increases with the decrease of the particle size. Indeed, the diffusion distance being shorter for smaller particles, the carbon atoms generated from the dissociation of the reactive

species can diffuse easily and rapidly to participate to the growth of CNTs, leading to larger growth rates.

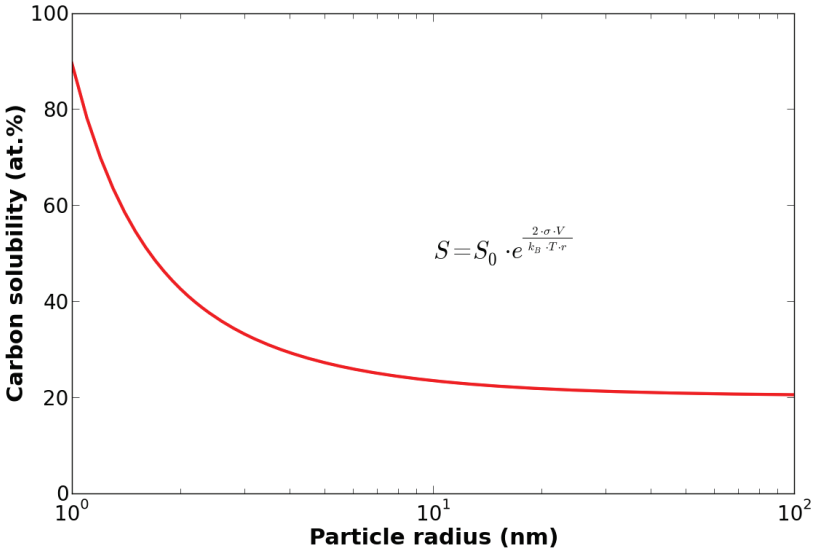

Figure 3.3.4: Evolution of the carbon solubility with the size of a spherical iron nanoparticle.

Although it was difficult to estimate the CNT length and thus the growth rate because most of samples exhibit entangled CNTs, such changes in the carbon solubility are found to be particularly significant for the NP sizes below 5 nm as detected in our CVD reactor. Furthermore, since the CNTs are formed by dissolving, diffusing and precipitating the carbon atoms through the catalyst NPs, when the NP size is too small, the diffusing rate becomes higher than the precipitating rate at a given temperature. Hence, the catalyst NP lose its catalytic activity and the carbon atoms accumulate on its surface as amorphous carbon which terminates the CNT growth. In addition, since smaller NPs exhibit higher surface/volume ratio, it means that for the same amount of carbon, a small particle would have a smaller

volume to incorporate the carbon atoms on a given surface compared to a bigger one. Therefore, the carbon atoms would be essentially located on the small NP surface inducing a higher probability to form a stable hull around the particle. According to these two reasons, a small NP is more likely to be encapsulated by carbon, thus explaining the presence of carbon encapsulated catalyst NPs for the "smaller" optimized conditions observed in Fig. 3.3.1a, while the "larger" conditions exhibit higher CNT purity (Fig. 3.3.1b).

3.4 Summary

To sum up, *in situ*, non-intrusive, high throughput TRLII investigations were performed during the CNT synthesis by FCCVD for quantitative measurements of the NP size suspended in the gas phase, while LIBS was used to determine the iron/carbon atomic ratio along the CVD reactor. The Taguchi matrix robust design approach was utilized to examine the effect of the process parameters on the suspended NP diameter. The catalyst concentration and the injection speed have shown the most important influence, while other factors, such as the total gas flow, the vaporization or the growth temperatures, reveal a secondary impact. A linear correlation was found between the NPs formed in the gas phase and the resulting CNTs, whereas the former are about ten times smaller than the later. The consequences for the CNT growth mechanism were discussed. Finally, the TRLII diagnostic is a powerful tool to *in situ* monitor the final CNT structure and unravel the CNT growth mechanism.

Nothing in life is to be feared, it is only to be understood. Now is the time to understand more, so that we may fear less.

Marie Curie

4

Chemical reactions in the gas phase

Chemical reactions in the CVD reactor mainly relies on physical mass and heat transport processes. As observed in the previous Chapters, the specific reactor geometry generates intrinsic temperature and species concentration gradients, inducing variations in both composition and structure of the as-grown materials. Therefore, a comprehensive understanding of the interactions between the physical and chemical reactions in the CVD reactor is desired.

4.1 Modelisation and *in situ* investigations

The gas phase multi physico-chemical mechanisms in the high temperature CVD reactor were numerically examined by combining

Table 4.1.1: Gas phase reactions of xylene, acetylene and ferrocene and rate constants in the CVD reactor.

Chemical reactions	Rate constants	Ref.
$C_8H_{10} + H_2 \rightleftharpoons C_7H_8 + CH_4$	$r = 9.2 \cdot 10^9 \cdot e^{\frac{-220000}{RT}} [C_8H_{10}] [H_2]^{1/2}$	[10]
$C_7H_8 + H_2 \rightleftharpoons C_6H_6 + CH_4$	$r = 4.0 \cdot 10^9 \cdot e^{\frac{-224000}{RT}} [C_7H_8] [H_2]^{1/2}$	[10]
$C_2H_2 + H_2 \rightleftharpoons C_2H_4$	$k = 1.4 \cdot 10^{35} \cdot T^{-9.06} e^{\frac{-214000}{RT}}$	[126]
$2\,C_2H_2 \rightleftharpoons C_4H_4$	$k = 8.7 \cdot 10^{13} \cdot e^{\frac{-312850}{RT}}$	[126]
$2\,C_2H_2 \rightleftharpoons C_4H_2 + H_2$	$k = 1.5 \cdot 10^7 \cdot e^{\frac{-178670}{RT}}$	[126]
$C_2H_2 + C_4H_4 \rightleftharpoons C_6H_6$	$k = 4.5 \cdot 10^5 \cdot e^{\frac{-126000}{RT}}$	[126]
$Fe(C_5H_5)_2 + H_2 \rightleftharpoons Fe + 2\,C_5H_6$	$k = 1.6 \cdot 10^{11} \cdot e^{\frac{-218000}{RT}}$	[88]

chemical reaction kinetics with physical transport phenomena, while the surface reactions were not computed due to lack ok kinetics data. Surface reactions and influence of the substrate will be experimentally investigated in Chapter 5. The simulations were performed in the high temperature furnace in the temperature range 500-800°C, assuming that the ferrocene/xylene solution was completely vaporized in the previous zone, as shown in Chapter 3. The chemical reactions used in this simulation are summarized in Table 4.1.1.

The gas fluid in the CVD system consisted of the different chemical species, including catalyst precursor, carbon feedstocks and their various decomposition byproducts. Argon being used as gas carrier, it was treated as solvent of the gas mixture. Hence, the fluid thermodynamic properties were approximated by those of argon. Correspondingly, the other species were considered as solutes. Moreover, according to the reactor geometry and the continuous mass feeding, the reacting fluid was described by 2D stationary momentum (Eq. 4.1), mass (Eq. 4.2) and heat balance (Eq. 4.4) equations. The fluid flow was expressed by the weakly compressible Navier-Stokes equations where is the $\vec{u}$ velocity vector ($m.s^{-1}$), η denotes the dynamic viscosity ($N.s.m^{-2}$), ρ is the fluid density ($kg.m^{-3}$) p and is the pressure (Pa).

$$\rho(\vec{u}\cdot\nabla)\vec{u} = \nabla\cdot[-p\vec{I} + \eta(\nabla_{\vec{u}} + \nabla_{\vec{u}}^{T}) - (\frac{2\eta}{3})(\nabla\cdot\vec{u})\vec{I}] \tag{4.1}$$

$$\nabla\cdot(\rho\vec{u}) = 0 \tag{4.2}$$

It is worth noting that the gas flow is assumed to be in laminar regime, according to the Reynolds number ($Re = 40 < 2200$), determined following the formula below, where V is the mean flow velocity ($\mathrm{m.s^{-1}}$), d is the diameter of the quartz tube (m), ρ is the fluid density ($\mathrm{kg.m^{-3}}$), Q is the volumetric flow rate ($\mathrm{m^2.s^{-1}}$), A is the cross-sectional area of the tube ($\mathrm{m^2}$) and µand v are the dynamic ($\mathrm{N.s.m^{-2}}$) and the kinetic ($\mathrm{m^2.s^{-1}}$) viscosity of the fluid respectively.

$$Re = \frac{\rho.V.d}{\mu} = \frac{Q.d}{v.A}$$

The boundary conditions used for the gas flow are as follows:

$$\text{Inlet} \Rightarrow u_0 = 0.01 m.s^{-1}; p_0 = 1.0x10^5 Pa$$
$$\text{Reactor wall and quartz plate} \Rightarrow \vec{u} = 0$$
$$\text{Outlet} \Rightarrow [\eta(\nabla_{\vec{u}} + \nabla_{\vec{u}}^{T}) - (\tfrac{2\eta}{3})(\nabla\cdot\vec{u})\vec{I}]\cdot\vec{n} = 0$$

The mass transfer was given by the following convection-diffusion equation, where c_i denotes the species concentration ($\mathrm{mol.m^{-3}}$), while D_i and R_i corresponds to the diffusion coefficient ($\mathrm{m^2.s^{-1}}$) and the reaction term ($\mathrm{mol.m^{-3}.s^{-1}}$) of the i specy respectively.

$$\nabla\cdot(-D_i\nabla_{ci}) = R_i - \vec{u}\cdot\nabla_{ci} \tag{4.3}$$

The corresponding boundary conditions are as follows:

$$\text{Inlet} \Rightarrow c_i = c_{i,0}$$
$$\text{Outlet} \Rightarrow \vec{n}\cdot(-D_i\nabla_{ci}) = 0$$

Finally, the energy balance was described by the convection and conduction equation, where C_p refers to the heat capacity ($\mathrm{J.kg^{-1}.K^{-1}}$),

k is the thermal conductivity ($W.m^{-1}.K^{-1}$), T stands for the temperature (K) and Q corresponds to the heat source ($W.m^{-3}$)term which was neglected here.

$$\nabla \cdot (-k\nabla T) = Q - \rho C_p \vec{u} \cdot \nabla T \tag{4.4}$$

It is worth noting that the species thermal conductivity (k) is given by the Stiel-Thodos equation [156], where M is the molecular weight and R_g is the gas constant ($J.mol^{-1}.K^{-1}$).

$$k = \frac{\eta}{M} \cdot (1.15C_p + 0.88R_g)$$

The related boundary conditions are given below, where T_{surf} is an interpolation function of the temperatures measured along the CVD reactor as shown in Chapter 2.

$$\begin{gathered}\text{Inlet} \Rightarrow T = T_0 \\ \text{Reactor wall} \Rightarrow T = T_{surf} \\ \text{Outlet} \Rightarrow \vec{q} \cdot \vec{n} = -\rho C_p T \vec{u} \cdot \vec{n}\end{gathered}$$

The resolution was carried out using the commercial computational software COMSOL Multiphysics 3.5. The schematic of the numerical CVD reactor is illustrated in Fig. 4.1.1a, while Fig. 4.1.1b shows the mesh element size. The mesh sequences were refined in the vicinity of the substrate, the inlet and the outlet.

The velocity field is illustrated in Fig. 4.1.2a and the 2D temperature profiles at 550°C, 700°C and 850°C are depicted in Fig. 4.1.2b-d.

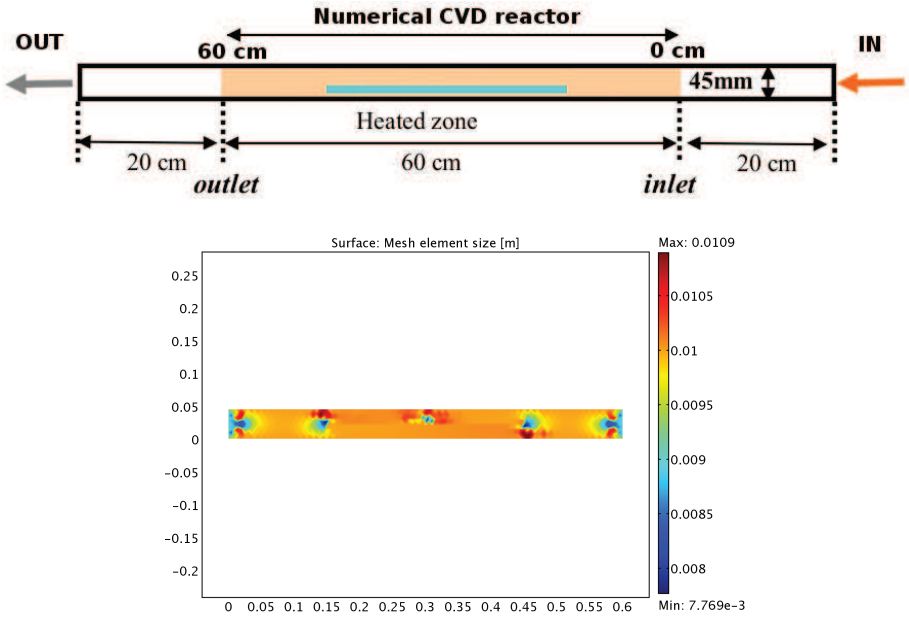

Figure 4.1.1: Schematic of the numerical CVD reactor (upper image) and surface graph of the mesh element size used for the simulations (bottom image).

4.1.1 Comparaisons between simulations and experiments

In order to validate the applicability of our gas phase chemical reactions model, the same CVD conditions (i.e. 1 L/min of Ar, 0.04 L/min of C_2H_2, 0.2 mL/min of ferrocene dissolved into xylene at 0.05 g/mL) were used for both experimental and numerical investigations. The gas exhaust at the center of the high temperature furnace was *in situ* analyzed by MS and GPC as a function of the temperature, based on the procedure depicted in Chapter 2. The relative intensities of C_2H_2 and C_8H_{10} were thus measured by GPC and those of C_7H_8 and C_6H_6 were obtained by MS. For comparison purposes, the simulations were performed at the center of the numerical reactor, corresponding to the center of the high temperature furnace. Figure 4.1.3. shows both the experimental (red dotted

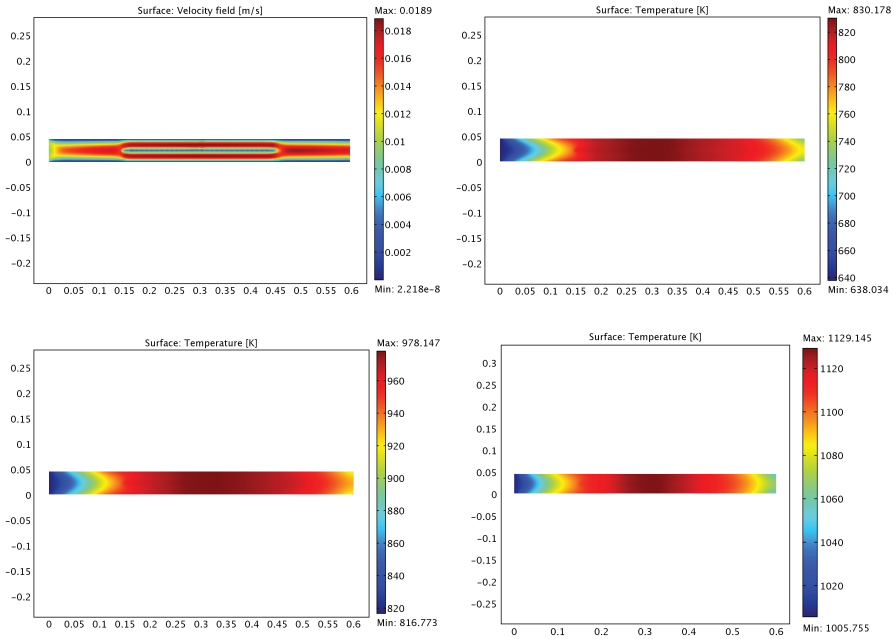

Figure 4.1.2: Surface graph of the velocity field (top left image) and the temperatures profiles at 550°C (top right image), 700°C (bottom left image) and 850°C (bottom right image).

line) and numerical (black straight line) evolutions of C_2H_2, C_8H_{10}, C_7H_8 and C_6H_6 in the CVD gas phase as a function of the temperature.

The concentrations obtained from experiment and simulation exhibit similar variation tendencies with the increase of the temperature. Hence, the numerical data are in a good agreement with the experiments. Nevertheless, since the experimental settings did not provide quantitative measurements, further investigations are needed to entirely validate the simulation model. Therefore, it can be used to predict the evolution of the chemical species in the CVD reactor under different conditions. For instance, similar simulations reported that the concentration of each species is space-dependant at a given

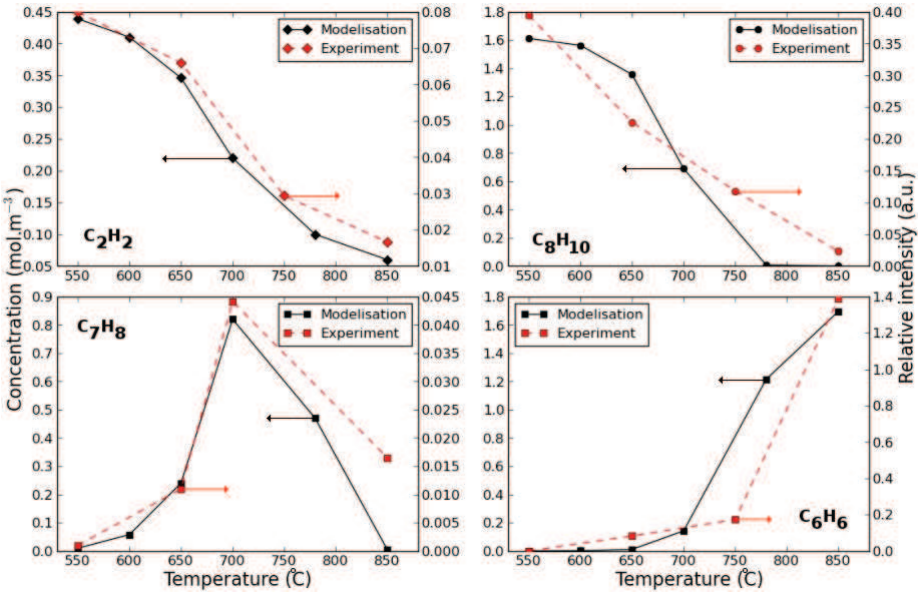

Figure 4.1.3: Comparaisons between experimental (red dotted lines) and theoretical (black straight lines) concentration evolutions of C_2H_2, C_8H_{10}, C_7H_8 and C_6H_6 at the middle of the CVD reactor as a function of the temperature.

temperature [62].

Moreover, Fig. 4.1.3 shows that little amount of xylene and acetylene are decomposed at temperatures lower than 600°C. Hence, xylene and acetylene were found to take one of the most important proportion in the gas phase atmosphere at these temperatures. Above 600°C, significant decomposition of these two carbon sources takes place. Toluene appeared as the second main carbon species in the CVD gas phase in the [600-700°C] range, while methane was also identifed as an important byproduct of the hydrocarbon decomposition under these conditions. When the temperature increases further (up to 850°C), benzene becomes the largest species in the gas atmosphere, as indicated by both experimental and numerical results in Fig. 4.1.3.

4.2 Influence of hydrogen

Real-time *in situ* GPC and MS were set up to analyse the pyrolytic decomposition of C_8H_{10} carried by a mixture of H_2 and Ar at different growth temperatures. It was found that the level of C_8H_{10}, continuously provided during the experiment, decreases as the reaction advances, leading to the generation of C_7H_8, CH_4, and further C_6H_6. When H_2 is added in the reacting atmosphere, the level of C_8H_{10} drops off while those of its byproducts increase, indicating that the dissociation of C_8H_{10} is significantly improved in the presence of H_2, as depicted in Fig. 4.2.1.

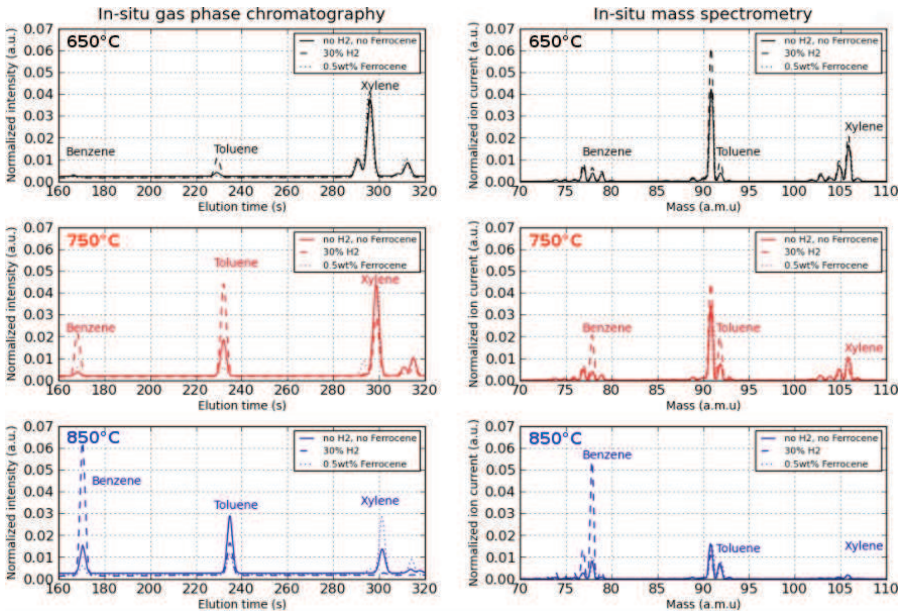

Figure 4.2.1: *In situ* GPC (left column) and MS (right column) analyses during the pyrolysis of C_8H_{10} at different temperatures without additional H_2 (straight line), with 30 vol.% H_2 (dashed line) or with 0.5 wt.% ferrocene (dotted line) [31].

H_2 addition-exchange reactions being much easier than the direct

bond cleavage pyrolysis, C_8H_{10} and further C_7H_8 can therefore decompose into C_6H_6 by hydrogenolysis as suggested by Benson et al. [10]. Since, this phenomena was observed at different temperatures ranging from 450 to 800°C, it validates the use of these reactions in the simulation as long as H_2 is directly provided in the reactor. However, even if H_2 is not directly provided in the CVD reactor, it can be produced in smaller amount during the chemical reactions, thus allowing the hydrocarbon decomposition by hydrogenolysis. In the same way as Fig. 4.1.1 where 30 vol.% of H_2 was directly provided in the reactor, a good agreement was also found between experimental and theoretical data when the feed of H_2 was turned off, as depicted in Fig. 4.2.2.

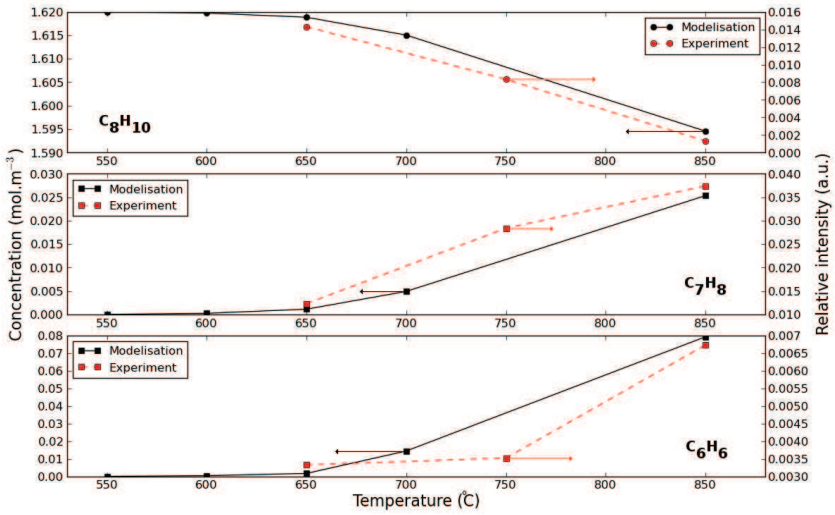

Figure 4.2.2: Comparaisons between experimental (red dotted lines) and theoretical (black straight lines) concentration evolutions of C_8H_{10}, C_7H_8 and C_6H_6 at the middle of the CVD reactor as a function of the temperature.

Moreover, similar results were obtained with ferrocene, as shown in Fig. 4.2.3. However, the difficulty to detect ferrocene and some

of its byproducts with our equipment did not allow quantitative measurement studies over the entire temperature range. Nevertheless, the comparison between the ferrocene pyrolysis *in situ* mass spectra at 550°C with and without H_2 shows that almost neither ferrocene nor some of its byproducts were detected in the presence of H_2, while the peak of ferrocene was clearly identified without H_2. It means that they were decomposed in the reacting atmosphere possibly via a hydrogenolysis mechanism, as proposed in our numerical model. Similar experiments conducted by Dormans [35] also reported the reduction of ferrocene at temperatures ranging between 400°C and 900°C in hydrogen atmosphere. Therefore, the presence of H_2 enhances the decomposition of both catalytic precursor and carbon feedstocks and allows to lower the reaction temperature.

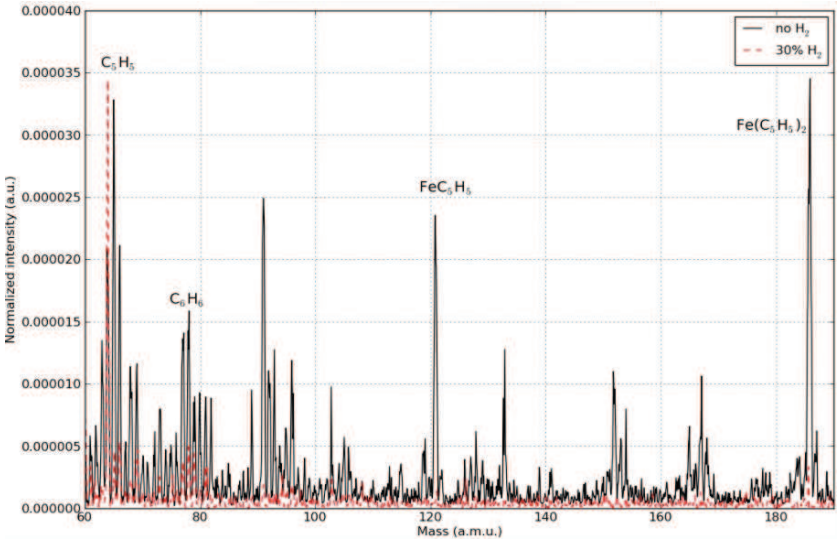

Figure 4.2.3: Mass spectra of the ferrocene pyrolysis at 550°C without additional H_2 (straight line) and with 30 vol.% H_2 (dashed line) [31].

Furthermore, when the H_2 rate becomes too high, it induces

suppressing effects on the CNT synthesis. For instance, H_2 rates higher than 30 vol.% were found to impede the CNT growth by driving the reverse reaction for decomposition due to the gasification of the deposited carbon [180], etching sp^2 bonds [7], inducing catalyst deactivation by Otswald ripening [15] and saturating dangling carbon bonds [125].

4.3 Influence of the effective carbon source(s) on the CNT growth mechanism

The real-time *in situ* analysis revealed an interesting correlation between the growth of CNT and the presence of C_6H_6. When no H_2 is directly provided in the reactor, the CNT growth was inhibited at temperatures lower than 750°C, which is consistent with other studies under similar conditions without H_2 [71] [187]. Mostly C_8H_{10} was detected under such conditions, as depicted in Fig. 4.1.3 and Fig. 4.2.1. Moreover, the amount of C_8H_{10} and its byproducts was found to remain at a similar level whether ferrocene was provided in the reactor or not. This means that C_8H_{10} does not experience any catalytic decomposition. Therefore, since no CNT growth was reported when almost only C_8H_{10} was detected in the reacting atmosphere it indicates that C_8H_{10} is not the effective hydrocarbon leading directly to CNT growth. In other words, the species originated from C_8H_{10} decomposition must be more efficient for the CNT growth than C_8H_{10} itself. This reveals that an incubation time is needed to accumulate sufficient amount of effective carbon sources to promote CNT nucleation and growth. This period duration strongly depends on the reaction kinetics and temperature. Hence, finding out the dominant effective carbon feedstock leading to high yield CNT synthesis is a critical factor for scaled-up CVD process.

Furthermore, the CNT growth at high temperature (above 700°C) is highly correlated with the presence of C_6H_6 in the reacting atmosphere, as shown in Fig. 4.1.1. It suggests that under these conditions, C_6H_6 might be one of the main precursors directly leading to CNTs, which is consistent with the six-membered ring model [44]. Therefore, the C_8H_{10} pyrolysis leading to C_6H_6 must occur to promote the growth of CNTs, which requires relatively high temperatures (above 750 °C). H_2 can be added into the reactor to catalyse the C_8H_{10} decomposition by hydrogenolysis, allowing to decrease the growth temperature, as detailed in previous section. However, C_8H_{10} does not decompose even in the presence of H_2 for temperatures below 600°C. In other words, C_8H_{10} only acts as a carrier below 600°C. It indicates that another carbon source is needed to grow CNT below 600°C. Nevertheless, Fig. 4.2.3 reveals that ferrocene can decompose at 550°C in a reducing atmosphere leading to both iron compounds and hydrocarbons, including C_6H_6. The numerical model indicates that C_5H_6 is one of the main product originated from ferrocene decomposition. Figure 4.3.1 shows that sufficient amount of this byproduct is produced in the CVD gas phase at relatively low temperatures.

These ferrocene byproducts may be able to serve as carbon feedstock to promote the CNT growth [102]. Figure 4.3.2a shows that CNTs can be successfully synthesized at 550°C after 15 min by using ferrocene as the only precursor for both catalytic and carbon sources. However, with the as-grown CNTs exhibiting a poor degree of alignment, short lengths and low density, this method is not efficient to synthesize CNTs at low temperatures for both composite applications and mass production. In addition, rising up the growth temperature does not increase the CNT yield under such conditions. Whereas the CNTs

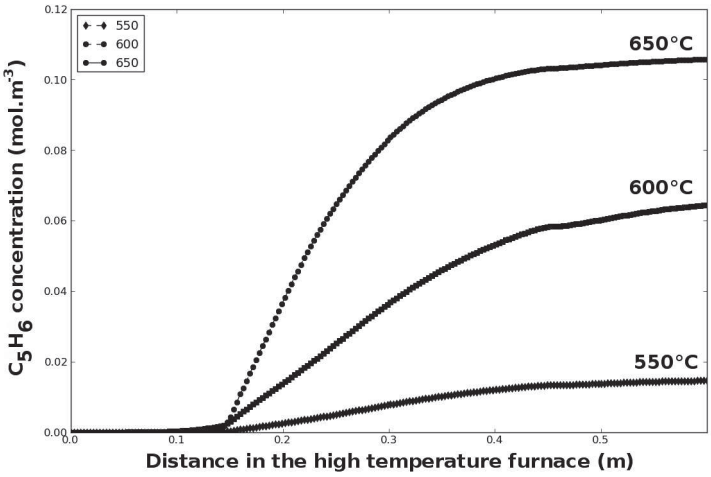

Figure 4.3.1: Predicted concentrations of C_5H_6 in the CVD gas phase from ferrocene decomposition in hydrogen atmosphere at low temperatures.

synthesized under the same conditions but at 650°C tend to be longer, the CNT density and purity significantly decreases, as depicted in Fig. 4.3.2b.

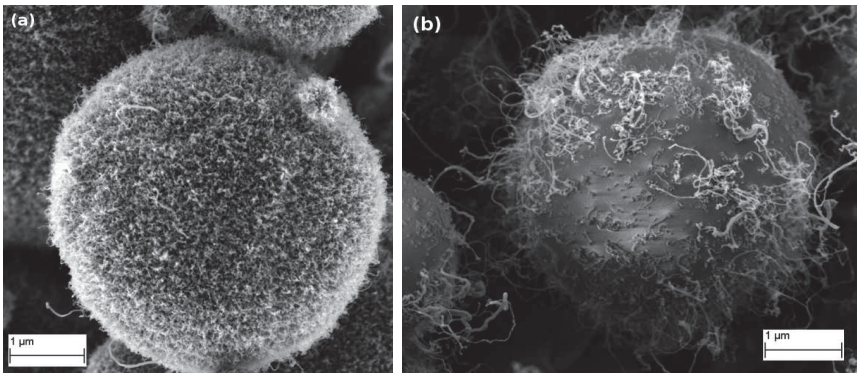

Figure 4.3.2: SEM image of CNTs synthesized on µ-Al_2O_3 after 15 min at 550°C (a) [31] and 650°C (b) using ferrocene as the only precursor for both catalyst and carbon source. The ferrocene was vaporized in the pre-heated zone at 250°C and carried into the CVD reactor by a mixture of Ar/H_2 at 1 L/min (H_2=20 vol.%).

Hence, the use of an additional carbon source is required. He et al. [60] showed that the addition of C_2H_2 as a second carbon source allows to keep decreasing the growth temperature down to 400°C under a reducing atmosphere. Indeed, at such low temperature, no CNT growth is reported if no C_2H_2 is provided in the reacting atmosphere. C_2H_2 and/or its byproducts may be able to react with C_8H_{10} used as the ferrocene carrier. Nevertheless, under these conditions, almost no C_6H_6 was detected neither by in situ MS nor by in situ GPC, suggesting that another growth mechanism different from the six-membered ring model occurs. In this case, C_2H_2 is supposed to be the main precursor directly leading to CNTs [91]. Therefore, all the species containing carbon are not necessarily effective carbon sources which efficiently contribute to the CNT growth. For instance, some carbon sources like xylene are directly inefficient in their original form, but becomes undirectly useful for the CNT synthesis through their decomposition byproducts. Hence, some carbon precursors favor the CNT synthesis at low temperature, while others require higher temperature to promote the CNT formation.

4.4 CNT GROWTH MECHANISM

Chapter 3 revealed that the quantity of iron deposited on the quartz plate decreases as the distance from the injector increases. However, the results from the numerical model based on Table 4.1.1 shows that the concentration of iron atoms in the gas phase observed an opposite trend, as depicted in Fig. 4.4.1.

Moreover, catalyst NPs in the gas phase were successfully detected at low temperatures (see Chapter 3), while the presence of iron atoms has not been experimentaly confirmed yet. This may indicate that the formation of catalyst NPs may not arise from the agglomeration of

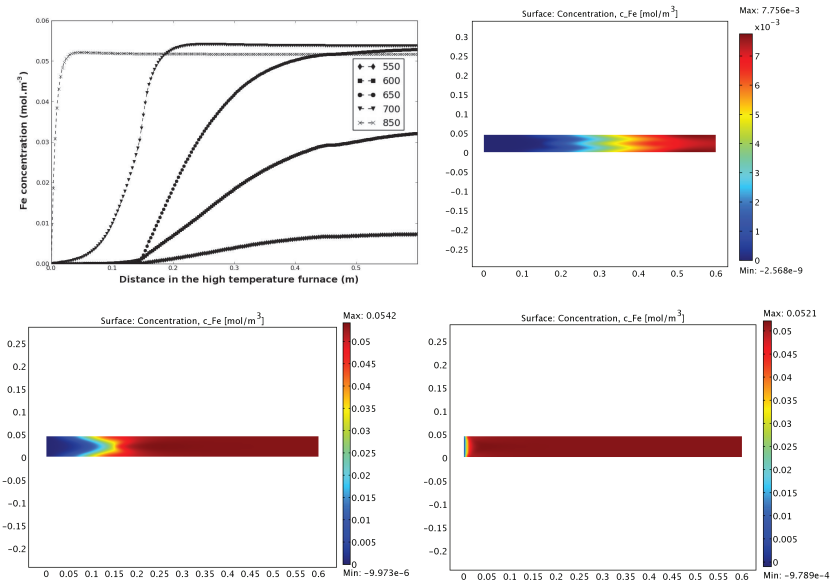

Figure 4.4.1: Predicted volume concentration distributions of Fe along the centerline in the CVD gas phase as a function of the temperature. The surface graphs of Fe volume concentration distribution are shown at 550, 700 and 850°C.

iron atoms into clusters at least in the first half of the CVD reactor at low temperatures, where residual ferrocene is dominant. In this case, the NP formation is more likely due to the precipitation and densification of solute in the droplets, as suggested in Chapter 3. The spray pyrolysis atomizes the xylene/ferrocene solution and heats the droplets to produce suspended solid particles with various size, which can further agglomerate to each other depending on their size distribution as detailed in Chapter 3. However, in the second half of the CVD reactor or at higher temperatures, faster droplet evaporation may induce a hybrid nanoparticle formation mechanism combining the liquid-to-solid NPs process previously suggested with the gas-to-solid NPs one, where the NPs would arise from vapor condensation. Such process is schematically represented in Fig. 4.4.2 based on the two mechanisms reported in Chapter 3. It may induce a larger NP size

distribution, which would subsequently lead to the agglomeration of NPs, as proposed in Chapter 3. Moreover, the NPs might keep growing on the substrate surface through different mechanism like condensation, coalescence or Otswald ripening. However, once CNT synthesis begins, further NP growth becomes less probable by virtue of the appended CNT. Hence the NP size distribution evolves both in the gas phase and on the substrate until it becomes truncated by catalytic growth of carbon species.

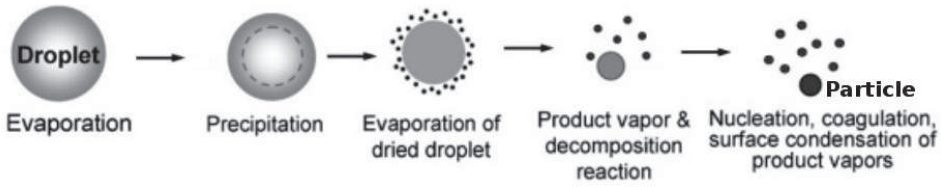

Figure 4.4.2: Schematic of the nanoparticle formation in floating CVD based on [129].

4.5 Summary

In this Chapter, the CVD gas phase chemical reaction kinetics were numerically investigated. The non-equilibrium CVD processes were simulated by combining chemical reaction kinetics with physical transport phenomena. The model took into account the influences of the reactor geometry (which was the same as that described in Chapter 2), the CVD parameters, the chemical reactions and the mass and energy transports to predict the evolution of the different species in the CVD atmosphere. *In situ* MS and GPC examinations were in a good agreement with the numerical data. Moreover, the evidence of a catalytic effect of hydrogen on the hydrocarbon decomposition was found, while the effective carbon sources were identified

as a function of the CVD temperature. Finally, the importance of the gas phase phenomena in the CNT growth mechanism was discussed.

One always admires what one really doesn't understand.

Blaise Pascal

5

Hidden role of the substrate

In this Chapter, CNT growth was successfully reported on a very large variety of substrates under different CVD conditions. This allows us to study the role(s) played by the substrate in the CNT growth mechanism.

5.1 The important role of the substrate

5.1.1 CNT growth on various substrates

The same floating catalyst CVD process was used to synthesize numerous CNT-based hybrid structures under different conditions for potential applications in composite materials. For instance, CNTs

with different density and morphology were grown on quartz, µ-SiC, µ-Al_2O_3, µ-TiC, graphene nanoplatelets and carbon fiber. Figure 5.1.1a shows the growth of a CNT multilayered forest on quartz, while the CNT hybridization with µ-TiC is presented in Fig. 5.1.1b. Therefore, CNTs are able to grow directly on almost any kind of substrate no matter its nature and morphology.

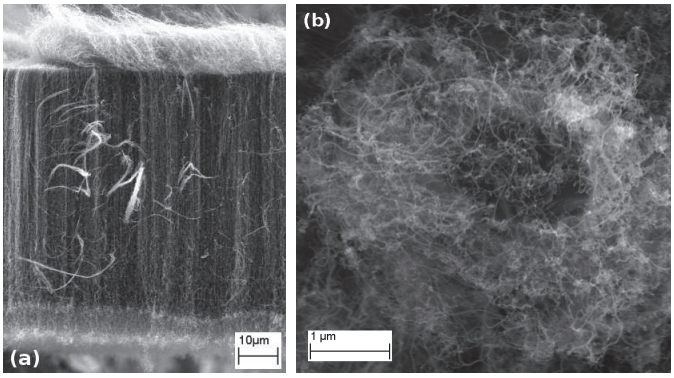

Figure 5.1.1: CNT grown under different CVD conditions on (a) quartz plate and (b) µ-TiC.

However, the CNT growth on carbon substrate is known to be very difficult due to the diffusion of catalyst in the substrate inducing deactivation and thus growth termination (the growth termination mechanisms will be discussed in details in the next chapter). To overcome this issue a diffusion barrier is usually coated on carbon substrates to allow the growth of CNTs. Such diffusion barriers being essentially made of ceramic materials can alter the properties of the final structure. Here, we report the CNT growth on graphene nanoplatelets and carbon fiber without any pre-treatment (like the deposition of a diffusion barrier). The CVD synthesis of CNTs on carbon fiber was investigated as a function of the growth temperature and the acetylene flow rate used as the carbon source. Since the

diffusion of catalyst through the carbon fiber is a thermodynamic process, the temperature should not be too high to prevent the catalysts from reacting with the substrate, but it should not be too low as well to allow the growth of CNTs. The results are summarized in Fig. 5.1.2 and show that CNTs can be directly and successfully synthesized even on carbon substrate in a wide range of conditions.

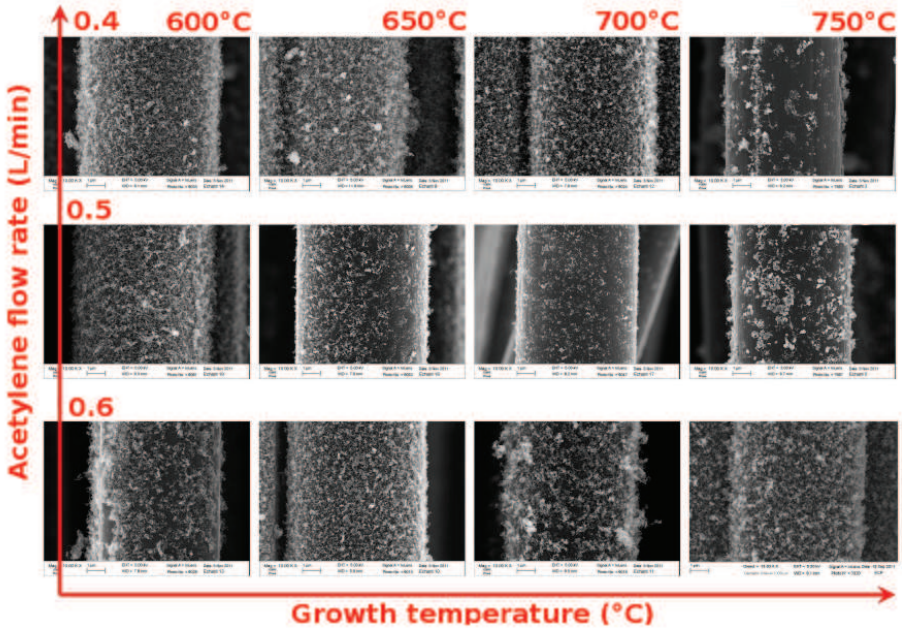

Figure 5.1.2: CNT growth on T700GC-12K carbon fibers by floating catalyst CVD as a function of the growth temperature and the acetylene flow rate. The other CVD factors were kept constant.

In the same way, the CNT growth on graphene nanoplatelets (GNs) by floating catalyst CVD without any pre-treatment was successfully reported. Raman analyses were performed on pristine GNs, as-grown CNTs and as-prepared CNT-GN hybrids. The Raman spectra of the GNs shown in Fig. 5.1.3 exhibits three characteristic peaks centered

at 1330, 1575 and 2690 cm^1 that can be assigned to the D, G and 2D bands of graphene, respectively. The peak width of 2D band and the ratio of 2D/G (about 0.63) confirm that the graphene nanosheet is few-layered. In comparison, the Raman spectrum of CNT-GN hybrids exhibits broadened G and 2D bands, and a prominent D band due to the existence of CNTs. Interestingly, the D and 2D bands appeared with a slight shift toward lower frequencies. To validate this, CNTs were grown on quartz under the same conditions as the ones synthesized on GNs for Raman measurements. As expected, the Raman spectra of the as-grown CNTs presents a large D band at 1325 cm^1 and a weaker G band at 1590 cm^1, in addition to 2D band. The ratio between D band and G band of GNs is about 0.5, whereas that of CNT-GN and CNTs are 1.3 and 1.4 respectively.

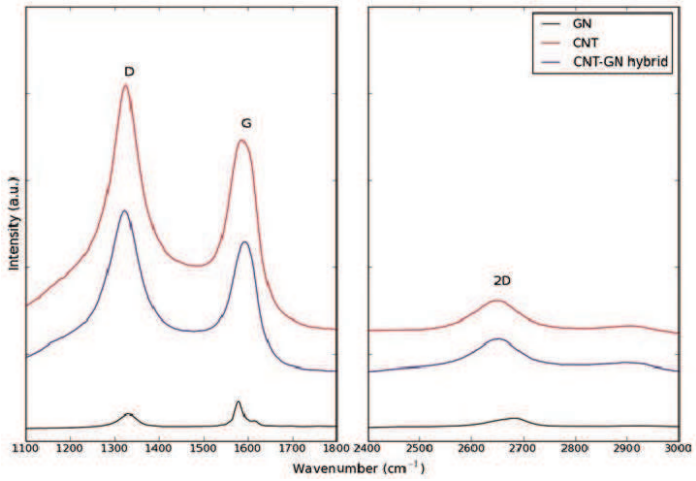

Figure 5.1.3: Raman spectra of GNs (black), CNTs (red) and CNT-GN hybrids (blue) [32].

The CNT growth on GNs was successfully reported for a wide range of temperature varying from 450 to 950°C. The CNTs were found to be well aligned and perpendicular to the GNs surface above 550°C, as

shown in Fig. 5.1.4. The thickness of the GNs is about few nanometers confirming the results from Raman, and the length of the CNTs reaches up to 10 µm. Moreover, the arrows in Fig. 5.1.4 suggest a CNT base growth mechanism, since most of the catalyst nanoparticles were found at the root of the CNTs. Since the temperature is known to influence the growth rate, the synthesis time was adjusted to obtained similar CNT lengths (about 10 µm) at different temperatures. Notably, the temperature also affects the CNT diameter, as depicted in Fig. 5.1.4f. Indeed, the CNT mean diameter measured by TEM increases with the reaction temperature from 5.4 to 9.3, 15.2, 21.4 and 35.1 nm at 550, 600, 650, 700 and 850°C respectively. In addition, the diameter distributions were nearly mono-dispersed at relatively low temperatures (below 600°C), while they were broadened when the temperature increases, as detailed in chapter 3. Therefore, CNTs are able to grow directly on any kind of substrate no matter its nature and morphology, even on bulk and on nanocarbon substrates.

Furthermore, for a given substrate CNTs can grow in very different ways depending on the CVD conditions leading to a large variety of morphologies for one hybridization which is of paramount importance for further applications. For instance, CNTs were found to grow either on one side (see Fig. 5.1.5a) or on both sides (see Fig. 5.1.5b) of the SiC µ-platelets by tunning the temperature and hydrogen ratio. Different CNT morphologies were also reported on µ-Al_2O_3 as described by He et al. [61]. Hence a 'six-branched' CNT/µ-Al_2O_3 structure is depicted in Fig. 5.1.5c, while Fig. 5.1.5d shows a 'urchin-like' one.

To sum-up, the CVD synthesis of vertically-aligned CNTs was successfully reported independantly from the substrate nature and

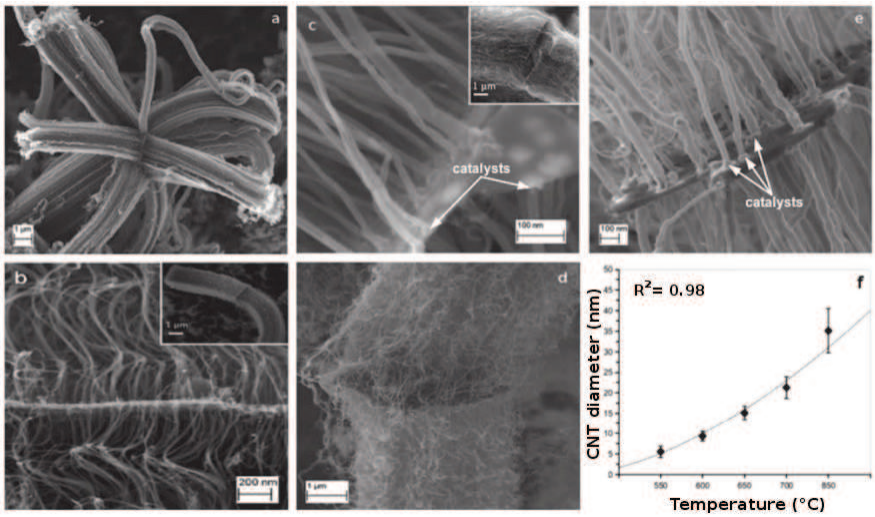

Figure 5.1.4: SEM images of CNT-GN hybrids synthesized at (a) 550°C, (b) 600°C, (c) 650°C, (d) 700°C and (e) 850°C. The mean diameters of CNTs measured by TEM at different growth temperatures are plotted in (f). The error bars correspond to the standard deviation of the CNT diameters [32].

morphology. The growth of the nanotubes is probably initiated normal to the substrate surface due to the direction of the carbon concentration gradient, when carbon will be first deposited on the exposed upper surface of the metal particle and diffuse through and over the metal to precipitate at the opposite face in the form of nanotubes. Once initial nanotube growth is established, growth will tend to continue in this same direction and may well be reinforced by the presence of surrounding nanotubes, where crowding will limit the possibilities for nanotube propagation in other directions. Moreover, under similar CVD conditions, TGA analysis show that CNTs have a small content of amorphous carbon of 3 wt%, a high carbon purity of 99% and a high oxidation stability of about 923 K no matter the type of substrate involved. However, the CNT aspect ratio and density were found to widely change with the type of substrate. In the following, we will focus on the CNT growth on two different ceramic

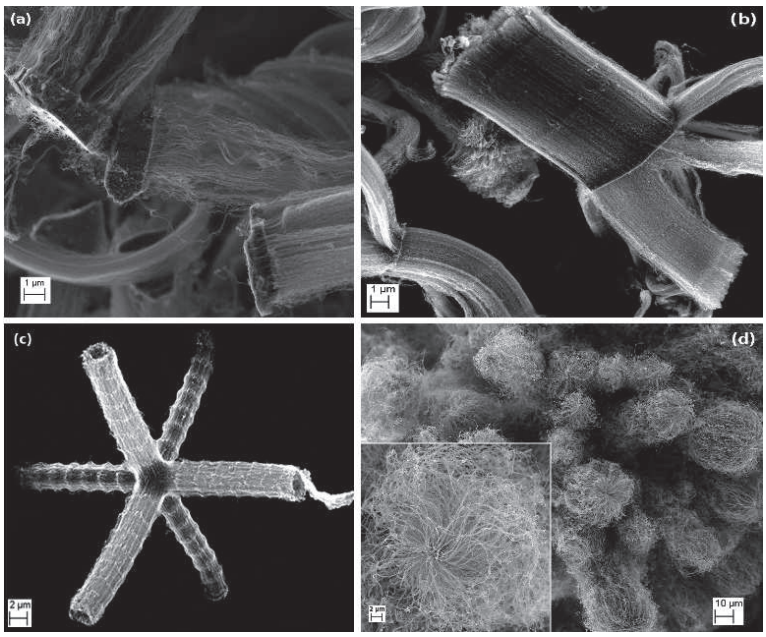

Figure 5.1.5: SEM images of vertically-aligned CNTs grown on one side (a) and both sides (b) of SiC µ-platelets. SEM images of the 'six-branched' and the 'urchin-like' CNT-µ-Al_2O_3 hybrid structures.

particles: the CNTs grown on alumina micro-spherical particles (µ-Al_2O_3) and that synthesized on silicon carbide µ-platelet particles (µ-SiC). These hybrid structures are among the most promising multi-scale combinations due to their interesting electrical [183], thermal [16] and mechanical [23] properties. Moreover, the CNT growth on non-flat µ-sized substrates is a promising approach for the mass production of CNT arrays, due to their large surface/volume ratio [79]. The advantage of the CNT synthesis on such kind of substrates is therefore twofold: it allows both to achieve large amounts of CNTs for industrial production purposes and to improve the properties of composite materials. Therefore, a better understanding and monitoring of the CNT growth process on non-flat substrates is needed.

5.1.2 Evidence of a catalytic effect of the substrate

At low temperatures, the CNT self-assembly was found to occur only on the ceramic µ-particles. Indeed, neither CNTs, nor amorphous carbon were observed neither on the reactor wall, nor on the quartz plate supporting the ceramic µ-particles, as shown in Fig. 5.1.7. However, when the reactor temperature increases above 550°C, the CNT growth covers all parts of the system (both the quartz plate, the reactor wall and the ceramic µ-particles). In other words, no CNT growth is achieved if no ceramic µ-particles are supplied in the CVD reactor at low temperatures. This already indicates the evidence of a catalytic effect of these substrates toward the CNT growth. Their larger surface/volume ratio compared to bulk substrates (here the quartz tube and plate) may enhance their reactivity. For instance, some studies reported the growth of SWNTs and DWNTs by ethanol CVD at 900°C using SiC [162] and Al_2O_3 [100] nanoparticles as catalysts without any additional metal. Therefore, it is supposed that these ceramic µ-particles act as catalyst in the precursors decomposition. They may absorb the hydrocarbons, and the byproducts might diffuse over the ceramic surface to the iron catalysts where they are incorporated.

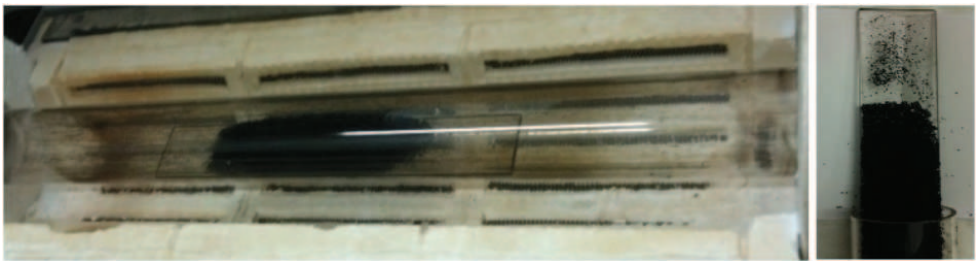

Figure 5.1.6: Pictures showing the very clean quartz tube and the quartz plate supporting the ceramic µ-particles right after 10 min CNT growth by aerosol-assisted CVD at low temperature [31].

Besides the substrate nature, the surface/volume ratio also seems to be a significant factor for the CNT yield. In order to validate this statement, we compare our results with the ones of Kim et al. [79] using bigger Al_2O_3 particles. In our case, for 0.40 g of µ-Al_2O_3 beads (2-5 µm in diameter) introduced in the reactor, about 0.42 g of CNTs were collected after 10 min reaction at 550°C, while Kim et al. [79] reported a CNT production of 0.26 g for 40 g of Al_2O_3 beads (0.5 mm in diameter) after 10 min reaction at 820°C. Since the substrate nature and the growth conditions are almost the same in both cases, it underlines the importance of the substrate morphology on the CNT yield. Hence, smaller Al_2O_3 beads exhibit higher surface/volume ratio, inducing higher reactivity and thus leading to higher CNT yield. Nevertheless, the CNTs grown on µ-sized substrates will be easily entangled after reaching few hundreds µm in length, which is not suitable for mm-long CNT synthesis contrary to bigger beads. Thus, in one hand, the semi-continuous method proposed by Kim et al. [79] allows the CNT separation from the supports and provide mm-long vertically-aligned CNT arrays, while in the other hand the method reported here, produces high density µ-scaled hybrid structures that can be directly used as reinforcements in multi-functional composites.

5.2 Synegistic effect of a mixture of ceramic particles

The simultaneous synthesis of multi-walled CNTs on a mixture of µ-Al_2O_3 and µ-SiC by floating CVD was examined. Liquid injection CVD process was used through a spray of aerosols containing both carbon feedstocks (xylene and acetylene) and catalyst precursors (ferrocene) at 575°C. Five samples with different SiC/Al_2O_3 mass ratios but a fixed total mass of 0,05 g were prepared as detailed in

Table 5.2.1. The CNT mass yield and morphology on the different mixtures of µ-Al_2O_3 and µ-SiC were systematically investigated by electron microscopy and thermo-gravimetric analysis (TGA). Then, the as-synthesized hybrid structures were directly incorporated into polyvinylidene fluoride (PVDF) to prepare composites without any other manipulation. The resulting polymer composites using the as-prepared hybrids as reinforcements exhibit significant enhancements of the dielectric properties while they preserve a good insulating nature.

Sample	SiC:Al_2O_3 (wt.%)	Ceramic (g)	Hybrid (g)	CNTs (g)	PVDF (g)	Hybrid content (wt.%)
1	100:0	0.05	0.080	0.030	5.00	1.57
2	70:30	0.05	0.130	0.080	5.00	2.53
3	50:50	0.05	0.185	0.135	5.00	3.57
4	30:70	0.05	0.140	0.090	5.00	2.72
5	0:100	0.05	0.105	0.055	5.00	2.06

Table 5.2.1: The mass of each component in the hybrid/PVDF composites.

5.2.1 Evidence of a synergistic effect of a mixture of ceramic particles

As already reported, the CNT self-assembly was found to always occur only on the ceramic µ-particles only. This selectivity makes the reaction mass yield easy to determine by measuring the weight difference of the ceramic particles before and after the CVD synthesis. As depicted in Table 5.2.1, five samples with different SiC/Al_2O_3 mass ratios but a fixed total mass of 0,05 g were prepared. The results, shown in Fig. 1, revealed that the CNT mass yield (including the catalyst particles) is dramatically affected by the substrate composition ratio. The estimated mass of the catalyst particles was about 2 wt.%, as detailed in Chapter 3. First, Al_2O_3 taken individually (sample 5)

exhibits higher reactivity than SiC (sample 1). Indeed, the CNT yield on Al_2O_3 alone is up to 52 wt.%, while that on SiC reaches about 38 wt.%. Larger CNTs yields were also observed on Al_2O_3 by Seidal et al. [148]. This can be actually explained by the surface area of µ-Al_2O_3 which is about 1.5 times higher than that of µ-SiC. The surface area is $\pi \cdot d^2$ for µ-Al_2O_3, while it is $2d^2$ for µ-SiC, assuming that both µ-Al_2O_3 and µ-SiC have the same diameter/length (d) ranging from 2 to 5 µm. Therefore, the CNT yield per unit area is in the same range for each substrate.

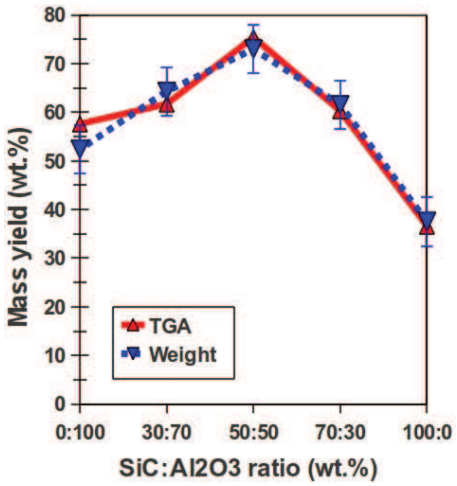

Figure 5.2.1: Evolution of the CNT mass yield determined by TGA and by the weight difference between the ceramic µ-particles before and after the CVD synthesis as a function of the SiC/Al_2O_3 ratio.

Since a large difference was found with the CNT growth on the two ceramic substrates taken individually, intermediate yields were expected when mixing Al_2O_3 and SiC together. However, Fig. 1 (dotted line) shows that the estimated CNT mass yield of the sample with an equal amount of SiC and Al_2O_3 (sample 3) is up to 73 wt.%, which is about 1.5 and 2 times larger than that of samples with

only Al_2O_3 or SiC respectively. As a comparison, Singh et al. [153] reported a CNT mass yield of 66 wt.% on ball milled silica using a solution of ferrocene/toluene at 700°C for 90 min (here 575°C for 10 min). Moreover, high CNT mass yields were also found for the other mixtures (samples 2 and 4). TGA analysis were performed to validate the CNT mass yield determined by the weight difference of the ceramic particles before and after the CVD synthesis. The results show that all the samples have a small content of amorphous carbon of about 3 wt.% and a relatively high oxidation stability of about 570°C. The CNT mass yield determined by TGA is in an excellent agreement with the one estimated from the weight difference, as depicted in Fig. 5.2.1. Higher CNT mass yields were found when mixing the two ceramic particles together. This unambiguously revealed a synergistic effect on the CNT growth under our CVD conditions.

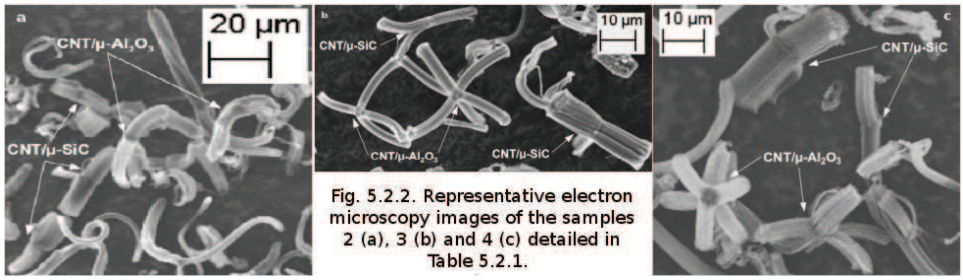

Fig. 5.2.2. Representative electron microscopy images of the samples 2 (a), 3 (b) and 4 (c) detailed in Table 5.2.1.

5.2.2 Discussion about the involved mechanisms

Nevertheless, at this stage the involved mechanism remains unclear. Systematic electron microscopy observations were performed on the different samples. Each one shows vertically aligned CNTs no matter the substrate nature or the SiC/Al_2O_3 mass ratio. Representative electron microscopy images can be seen in Fig. 5.2.2. The evaluation of the CNT length and diameter was averaged over 50 tubes for

each sample. The results, plotted in Fig. 5.2.3a, exhibit the CNT length, which is actually directly proportional to the growth rate, measured on µ-Al_2O_3 (continuous line) and on µ-SiC in the different mixtures. It can be seen that the length of the CNTs on µ-Al_2O_3 slightly increases with the addition of SiC µ-platelets into the mixture. Indeed, the CNT length on µ-Al_2O_3 rises up from 16.9 to 17.5, 18.4 and 19.7 µm, when the amount of µ-SiC in the mixture reaches 0, 30, 50 and 70 wt.% respectively. Reversely, the CNT length on µ-SiC decreases when µ-Al_2O_3 are added into the mixture. Indeed, the CNTs length on µ-SiC is ranging from 21.8 to 15.5, 14.9 and 14.4 µm with the addition of µ-Al_2O_3 into the mixture ranging from 0, 30, 50 and 70 wt.% respectively. Hence, the total CNT length over the different mixtures, being balanced by the opposite trend observed on the two ceramic particles, remains quite stable. Therefore, this cannot explain the increase of the CNT yield observed in Fig. 5.2.1.

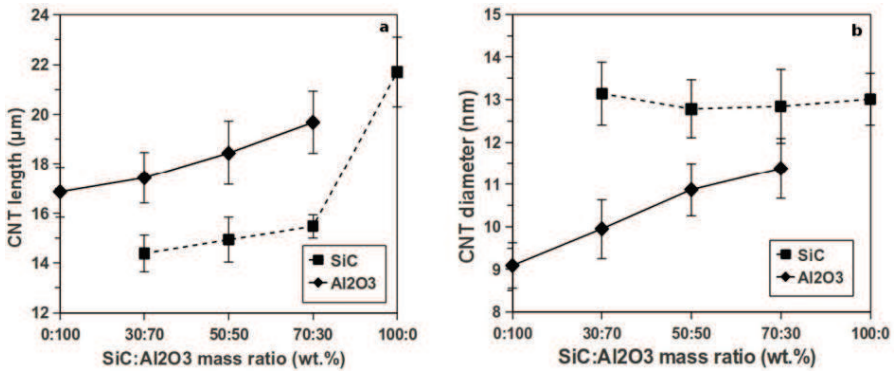

Figure 5.2.2: Evolution of the CNT length (a) and diameter (b) on both ceramic µ-particles as a function of the SiC/Al_2O_3 mass ratio.

Similar investigations have been performed about the CNT diameter, as depicted in Fig. 5.2.3b. It has been found that the CNT mean diameter on SiC µ-platelets (dotted line) remains almost the same

regardless the SiC/Al_2O_3 mass ratio, while the CNTs on µ-Al_2O_3 (continuous line) are getting larger when the amount of µ-SiC in the mixture increases. Indeed, the average CNT diameter on µ-SiC is in the range between 12.78 and 13.17 nm no matter the conditions, while the mean diameter of the CNTs grown on µ-Al_2O_3 slightly increases from 9.09 to 9.95, 10.87 and 11.38 nm with the µ-SiC content in the mixture set at 0, 30, 50 and 70 wt.% respectively. Moreover, change in the CNT diameter accounts for the CNT mass in a more significant way than that in the CNT length, as described by the equation: $m_{CNT} = \mu_{CNT} \cdot \pi \cdot r_{CNT}^2 \cdot L_{CNT}$, where m_{CNT}, μ_{CNT}, r_{CNT} and L_{CNT} respectively correspond to the mass, density, radius and length of a single CNT. Indeed, the CNT mass is directly proportional to the length, while it varies with the square of the diameter, assuming that the CNT density remains constant for each individual CNT. However, the changes in the CNT diameter shown in Fig. 3b induce a maximum augmentation of the CNT mass on µ-Al_2O_3 of 56.7 % for a fixed CNT length, which is not self-sufficient to explain the increase of the CNT mass yield observed in Fig. 1. Even if this value is slightly underestimated because the calculation above only considers SWNTs rather than MWNTs, it is still necessary to examine the bulk CNT density (i.e. the number of CNTs per unit surface area) in the mixtures. Although the number of CNTs was relatively difficult to quantify, an obvious difference can be observed between sample 1 and sample 3 respectively referring to CNTs grown on µ-SiC alone and on µ-SiC mixed with µ-Al_2O_3, as depicted in Fig. 5.2.4. The change in the bulk CNT density is not as significant on µ-Al_2O_3 as on µ-SiC.

Furthermore, the opposite trends found on the CNT length coupled with the observations of the CNT diameter and bulk density may indicate that µ-SiC and µ-Al_2O_3 play different roles in the CNT growth.

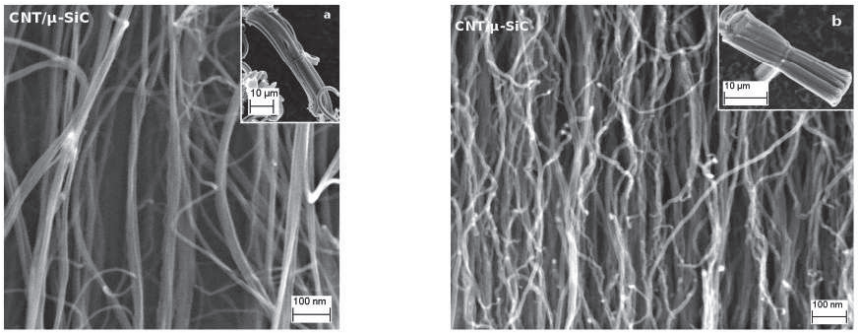

Figure 5.2.3: Representative electron microscopy images of the CNTs grown on SiC from sample 1 (a) and sample 3 (b). The bulk CNT density is obviously higher when the two ceramic µ-particles are mixed together. Low magnification SEM images of the corresponding CNT/µ-SiC hybrids are shown in the insets.

Since the CNT diameter can be correlated to the catalyst particle size [46], the fact that the CNT diameter on µ-Al_2O_3 increases with the addition of µ-SiC, while that on µ-SiC remains the same even in the presence of µ-Al_2O_3 may suggest that µ-SiC possibly plays a role in the formation of the catalyst particles contrary to µ-Al_2O_3. In order to verify this statement, new CVD synthesis were performed under the same conditions as already described but without using C_2H_2. In other words, only the ferrocene/xylene solution was provided in the reactor. Chapter 4 reported that the xylene does not decompose under these conditions and thus only serves as a carrier. Three samples were prepared with different substrates: the first one used a mixture equally composed of µ-SiC and µ-Al_2O_3, while the second and the last ones used µ-Al_2O_3 alone and µ-SiC alone respectively. Fig. 5.2.5b shows representative SEM image of the µ-SiC/µ-Al_2O_3 mixture after the CVD synthesis. It can be seen that the Al_2O_3 µ-particles remain totally free from CNTs, while the surfaces of the SiC µ-platelets are covered by both CNTs and nanoparticles. However, the same CVD conditions were found to independently lead to CNT growth on both µ-Al_2O_3 and µ-SiC, as depicted in Fig. 5.2.5a and 5.2.5c respectively.

Hence, we can say that µ-SiC play a role on the catalyst nanoparticle formation while µ-Al_2O_3 rather affect the carbon feedstock decomposition. In fact, we did observe the color change of µ-Al_2O_3 (from white to dark grey) under these conditions when only C_2H_2 was fed due to the enhanced decomposition of C_2H_2. Therefore, the combination of these two substrates induces larger amounts of both catalyst and carbon precursors available to promote the CNT growth, confirming the increase of the CNT density and diameter, which subsequently induces higher CNT mass yields.

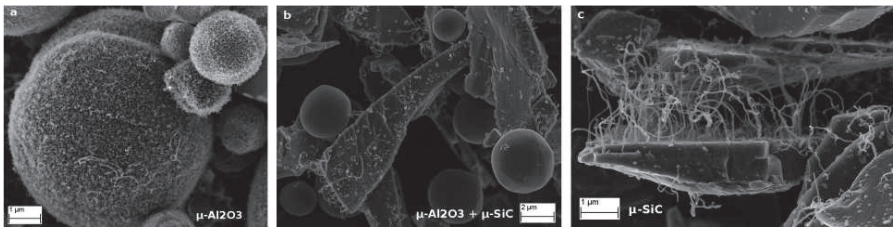

Figure 5.2.4: SEM images of CNTs on µ-Al_2O_3 (a), µ-SiC (c) and a mixture equally composed of µ-SiC/Al_2O_3 (b) grown under the same CVD conditions.

5.2.3 Application to dielectric polymer composites

Finally, the as-prepared CNT-based hybrids were incorporated into PVDF for the preparation of polymer composites as detailed in Table 5.2.1. Figure 5.2.6 shows the dielectric permittivity, AC conductivity and loss tangent of the resulting composites. The dielectric permittivity (Fig. 5.2.6a) of the composite reinforced with SiC hybrid alone is 26 at 100 Hz and room temperature, which is about 2 times larger than that of pristine PVDF (10 13). With the increase of the µ-Al_2O_3 mass ratio in the mixture while retaining the total mass constant, the dielectric permittivity of the composites increases accordingly and reaches the maximum (360) at SiC:Al_2O_3=50:50. After that, the permittivity starts to decrease with increasing µ-Al_2O_3

ratio further until reaching the lowest value (19) in the composite with Al_2O_3 hybrid alone. In the hybrid/PVDF composites, the increase in the dielectric permittivity can be derived from the formation of microcapacitors as a result of readily aligned state of nanotubes [183]. In the case of SiC:Al_2O_3=50:50, the highest CNT density could give rise to the most effective microcapacitors, thus resulting in the largest permittivity value. The AC conductivity exhibits almost the same trend as that of the dielectric permittivity, as depicted in Fig. 5.2.6b. It should be emphasized that even the maximum conductivity is very low ($2.1 \cdot 10^{-7} S.m^{-1}$), indicating a good insulated nature. This is further confirmed by the low loss values found for all the as-prepared dielectric composites, as shown in Fig. 5.2.6c.

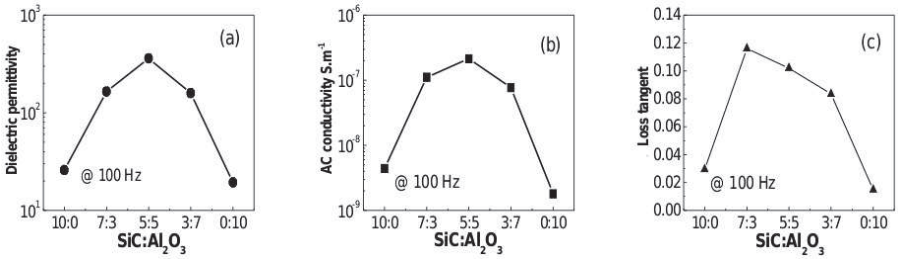

Figure 5.2.5: Dependence of the dielectric permittivity (a), the AC conductivity (b) and the loss tangent (c) of the PVDF and CNT-based hybrids composites with different SiC/Al_2O_3 mass ratio.

5.3 Summary

In this Chapter, CNT growth on several different type of substrates was reported, revealing the importance of the substrate nature and shape on the CNT yield and morphology. The CNT synthesis on μ-Al_2O_3, μ-SiC and their mixtures was studied further. A synergistic effect between μ-Al_2O_3 and μ-SiC on enhancing the CNT mass yield

during CVD was found. When these two ceramic particles were mixed together, larger CNTs were identified on µ-SiC, while longer CNTs were reported on µ-Al_2O_3. The number of CNTs per surface area was also found to be affected, explaining the increase of the global mass yield. This synergistic effect may arise from the favorable combination of the catalytic roles of µ-Al_2O_3 and µ-SiC. Finally, the as-synthesized CNT-based hybrids were directly used to prepare polymer composites exhibiting improved dielectric permittivity and loss tangent. The dielectrical properties were signicantly enhanced, especially in the case of composites with SiC:Al_2O_3=50:50 ratio, which might be ascribed to the largely formed microcapacitors composed of the CNT-based hybrids as electrodes and the polymer matrix as dielectric. The high permittivity and low loss of these new composite materials may provide great potential applications as energy storage material.

It matters if you just don't give up.

Stephen Hawking

6

The CNT growth stage

6.1 Evidence of a base growth mechanism

SEM observation in Fig. 6.1.1a revealed a "six-branch" CNTs/Al_2O_3 hybrid structure as described by He et al. [61]. Each branch is composed of three stacked layers constituting a multi-layered carpet of MWNTs deposited on Al_2O_3 µ-spheres. In this case, the number of layers corresponds to the number of sequences during the overall growth process. Moreover, the CNT growth rate, averaged over several samples originating from different batches, is linear with the reaction time, as shown in the insets in Fig. 6.1.1. It means that the CNT length of each layer is actually controlled by the growth time of its respective sequence (1.9 µm for 3 min growth, 3.5 µm for 5 min and 6.1 µm for 7 min). It is thus possible to identify the layer corresponding

to each sequence: the height of the carpet being proportional to the duration of the sequence, it is easy to attribute the top layer to the first injection and the bottom one to the very last. Indeed, the shortest layer, corresponding to the first sequence (3 min) ends at the top of the stack and reversely the longest layer, which refers to the last sequence (7 min) ends at the bottom of the stack. In addition, it should be noticed that the same conclusion can be drawn with different substrates like SiC µ-platelets under similar conditions even when the sequence order has been reversed (7 min following by 5 min and then 3 min), as depicted in Fig. 6.1.1b. The growth of a new layer eventually occurs under the previous one by lifting it up, the same result as the isotope labelling technique on flat Si substrates [134]. Figure 6.1.2 definately validates this assomption. Three CVD sequences were performed under the same conditions to grow stacks of vertically-aligned CNTs inside µ-Al_2O_3 which were partially broken but still exist as single individual pieces. During the synthesis, the µ-Al_2O_3 were broken in half. Each piece of a single µ-Al_2O_3 was pushed apart from each other but remained linked through the CNTs grown in between, just like a bridge. This bridge was composed of 6 stacks of aligned CNTs, indicating that three stacks actually originated from one piece of the µ-Al_2O_3, while the other three stacks were grown from the other piece. Therefore, this confirms that the CNT growth mechanism originates from the substrate surface independendtly from its nature and morphology as long as both catalyst precursors and carbon feedstock are provided in the floating catalyst CVD reactor.

This multi-layered CNT growth on various substrates was performed while all the sequences were done during the same CVD batch. Moreover, similar results were also reported when each sequence correspond to a different and independent CVD batch. For instance, after the

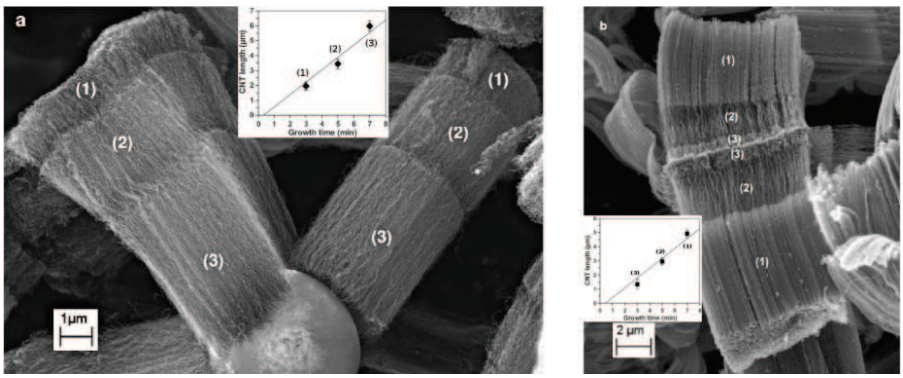

Figure 6.1.1: SEM images showing a 3 stack of aligned CNT layers on µ-Al2O3 (a) and on µ-SiC (b). Three separated growth sequences with the same conditions but different growth time were used [31].

first CVD synthesis leads to the first CNT layer, the samples were collected and kept out of the reactor at room temperature in air under typical atmospheric conditions. The next sequence was then processed one year later under similar CVD condition in the same reactor. First, even after 1 year, the 'old' CNTs exhibited similar length, diameter and density as before, indicating that they have not been damaged during that time. Then, the new CNT layer was grown under the 1 year-old one by lifting it up according to the same mechanism as previously described.

6.2 A PSEUDO *in situ* PARAMETRIC STUDY

The as-reported CNT stack formation technique was used as a pseudo *in situ* method to investigate the CNT growth on µ-SiC and µ-Al_2O_3. It was tailored to explore the effects of various growth factors such as growth temperature, reaction time, carbon sources, hydrogen flow rates, catalyst concentration, solution feed rate on the CNT

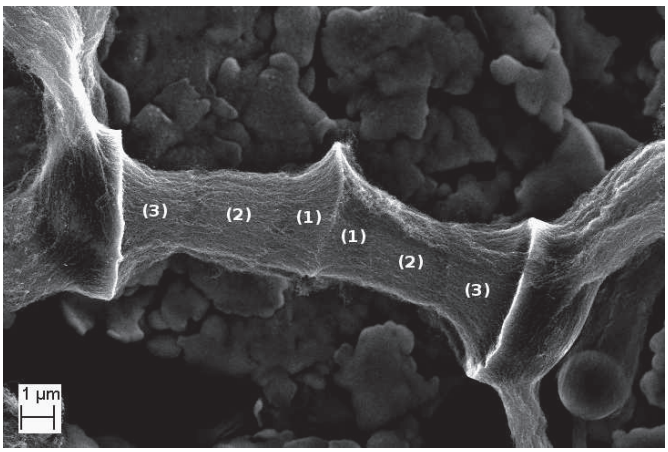

Figure 6.1.2: SEM images showing a bridge composed of 6 stacks of aligned CNTs connecting two pieces of a single µ-Al_2O_3 after three different injections performed under similar conditions by floating catalyst CVD.

synthesis.

The synthesis of CNTs was carried out in the CVD reactor, as detailed in Chapter 2. Briefly, the front part was heated to 523 K by a pre-heater system (10 cm long), while the main part was heated to a temperature ranging from 673 to 1173 K. Less than 1/2 g of pristine ceramic µ-particles (µ-SiC or µ-Al_2O_3) without any pretreatment were first homogeneously dispersed on the surface of a quartz plate, which was then put into the centre of the reactor. The same settings were used for all the experiments. The substrate was heated to the set temperature under the carrier gas, argon (Ar 99.8% purity full scale: 10 L.min^1 [6-10%]) and hydrogen (H_2 99.9% purity full scale: 5 L.min^1 [0-8%]), introduced with different ratios. The total gas flow rate was kept at 1 L.min1. Ferrocene ($Fe(C_5H_5)_2$) was dissolved into xylene (C_8H_{10}) at various concentrations to serve as catalyst precursor. Then, the mixture was fed by a syringe system (Razel Science, R99-E) at different rates and carried into the pre-heated stable reaction zone

in the form of spray by the carrier gas. The injection of acetylene as an additional carbon source was performed at a flow rate ranging from 0.02 to 0.1 L.min^1 depending on the experiments (C_2H_2 99.6% purity full scale: 1 L.min^1). A 12 min pause, where the injection of both carbon sources and catalyst precursors was turned off, separated the injection sequences from each other. The total CNT growth time, less than 20 min was divided in several sequences ranging from 3 to 7 minutes each. The sequential injection method was used to *in situ* change some factors during the same CVD batch, as detailed in Table 6.2.1. At the end, the furnace was cooled down under Ar at 1 L.min^1.

Studied parameters	Substrate's type	Sequence 1	Sequence 2	Sequence 3
Reaction time	Al_2O_3 µ-spheres	823; 0.05; 0.2; 3	823; 0.05; 0.2; 5	823; 0.05; 0.2; 7
	SiC µ-platelets	823; 0.05; 0.2; 7	823; 0.05; 0.2; 5	823; 0.05; 0.2; 3
Growth temperature	Al_2O_3 µ-spheres	823; 0.05; 0.2; 5	873; 0.05; 0.2; 4	923; 0.05; 0.2; 3
	SiC µ-platelets	823; 0.05; 0.2; 5	873; 0.05; 0.2; 4	923; 0.05; 0.2; 3
Catalyst concentration	Al_2O_3 µ-spheres	823; 0.01; 0.2; 4	823; 0.05; 0.2; 4	823; 0.1; 0.2; 4
	SiC µ-platelets	823; 0.01; 0.2; 4	823; 0.05; 0.2; 4	823; 0.1; 0.2; 4
Injection speed	Al_2O_3 µ-spheres	823; 0.05; 0.05; 5	823; 0.05; 0.1; 5	823; 0.05; 0.2; 5
	SiC µ-platelets	823; 0.05; 0.05; 5	823; 0.05; 0.1; 5	823; 0.05; 0.2; 5

Table 6.2.1: Summary of the growth conditions used at each sequence for the different experiments. The constant parameters for all experiments are the Ar (0.7 L/min), the H_2 (0.3 L/min) and the C_2H_2 (0.04 L/min) flow rates. The data respectively refer to the growth temperature (K), the catalyst concentration (g/mL), the liquid injection speed (mL/min) and the reaction time (min) [31].

Tuning the CVD conditions can induce significant changes in the CNT yield and morphology. For instance, the reaction temperature is responsible of the CNT organisation on the substrate, as depicted in Fig. 6.2.1. When the temperature rises up, the CNT diameter increases, while the CNT diameter distribution was found to be nearly mono-dispersed under these conditions for both µ-Al_2O_3 and µ-SiC. The CNT average diameter was evaluated by HR-TEM onµ-Al_2O_3 to 6.2, 9.7 and 13.7 nm at 823, 873 and 923 K respectively and to 10.6, 14.3 and 18.8 nm on µ-SiC. Hence, bigger catalyst particles are formed at higher temperatures under the conditions depicted in Table 6.2.1,

possibly caused by coarsening of the catalyst nanoparticles [57]. For a given amount of catalyst precursor, reducing the catalyst particle size is usually effective to increase the CNT density. Since the same amount of iron was provided during each injection, it means that the CNT density decreases when the temperature increases, which can be obviously observed in Fig. 6.2.1.

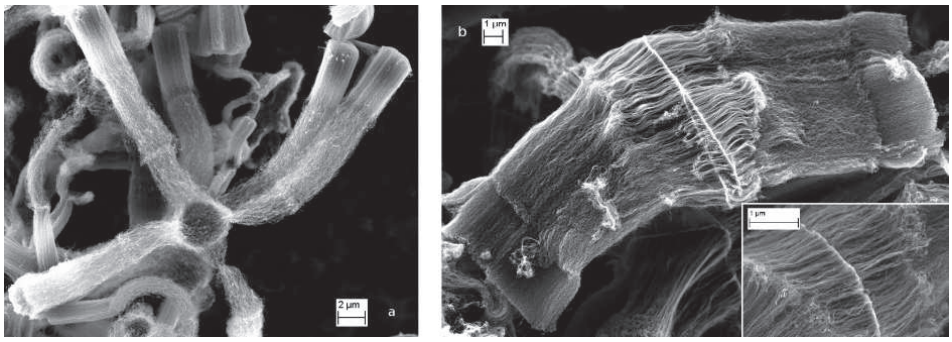

Figure 6.2.1: SEM image showing the CNT stack formation on µ-Al_2O_3 (a) and µ-SiC (b) where each layer was synthesized at different growth temperatures as detailed in Table 6.2.1 [31].

In contrary, tuning the feed of catalyst precursor at a given temperature may help to control the CNT diameter and density. Two parameters monitor the feed of ferrocene: the catalyst concentration and the injection speed. However, no significant changes were found in the CNT diameter and density, neither with the catalyst concentration nor with the solution feed rate, under the conditions detailed in Table 6.2.1. Reducing the feed of ferrocene actually results in a significant decrease of the CNT yield, as also observed by Kim et al. [79]. Indeed, no CNTs were reported for catalyst concentrations below 0.001 g/mL, and few, sparse, very short and non-aligned CNTs are synthesized for the concentrations ranging from 0.001 to 0.01 g/mL. When the concentration reaches 0.01 g/mL, vertically aligned CNTs can be

grown on the surface of the different µ-particles, as depicted in Fig. 6.2.2. If the concentration is further increased up to 0.1 g/mL as referred in Table 6.2.1, the CNT growth rate increases on both µ-Al_2O_3 (inset Fig.6.2.2a) and µ-SiC (inset Fig.6.2.2b). It indicates that the addition of ferrocene favours the decomposition of carbon source, and thus the CNT yield. In the same way as the catalyst concentration, the solution feed rate also influences the CNT yield. The CNT length is about 0.5 µm on both µ-Al_2O_3 and µ-SiC when the solution feed rate is 0.05 mL/min, while it reaches 3.5 µm on µ-Al_2O_3 and 2.7 µm on µ-SiC when the feed rate is 0.1 mL/min. When the injection speed is further increased above 0.1 mL/min, the CNT length becomes stable, meaning that below 0.1 mL/min, the CNT growth is limited by the catalyst formation and the incubation time [76]. Since the growth rate tends to stabilize beyond 0.1 mL/min, it suggests that the optimum Fe/C ratio is reached.

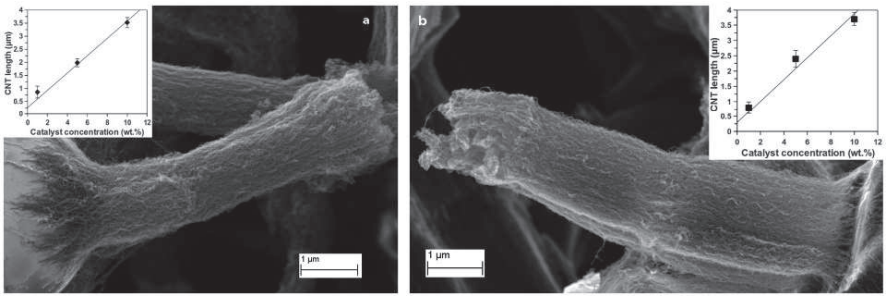

Figure 6.2.2: SEM image showing the CNT stack formation on µ-Al_2O_3 (a) and µ-SiC (b) where each layer has been synthesized. The CNT length vs the catalyst concentration is plotted in the insets [31].

Besides its effect on the growth kinetics, the Fe/C ratio also shows a significant influence on the CNT graphitization degree. Six specimens of CNT/µ-Al_2O_3 hybrids were prepared under similar CVD conditions but with different Fe/C atomic ratio injected into the reactor. Figure

6.2.3a shows the Raman spectra of each sample. The ratio of the G band over the D band which is related to the CNT graphitization degree was plotted as a function of the Fe/C atomic ratio used to synthesis the hybrids, as depicted in Fig. 6.2.3b. The observations show that there is an optimum Fe/C atomic ratio under the considered CVD conditions for which the I_G/I_D ratio is maximised. Below and above this Fe/C ratio, the CNT graphitization degree was found to decrease, as illustrated in Fig. 6.2.3b.

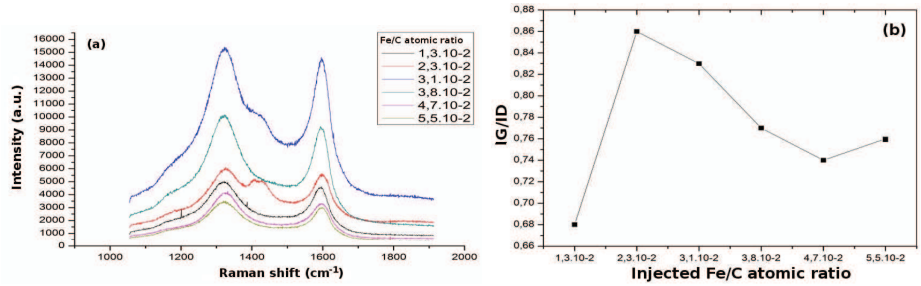

Figure 6.2.3: Raman spectra of the CNTs grown on μ-Al_2O_3 at different Fe/C atomic ratios injected in the CVD reactor (a). The ratio between the intensity of the G band over that of the D band is plotted as a function of the Fe/C atomic ratio injected during the growth.

According to these results, it is thus possible to control precisely the CNT density and aspect ratio on different substrates by simply playing on the CVD growth factors. Moreover, different CNT densities and aspect ratios will induce various hybrid morphologies as described by He et al. [61], namely six-branch, short dense homogeneous and urchin-like. Therefore, if one designs an appropriate sequential injection process where each sequence would respectively correspond to the growth of a specific morphology, one will be able to create a CNT-based hybrid structure with a totally new architecture. Such hybrid structures were successfully synthesized as depicted in Fig.

6.2.3, by applying a first sequence corresponding to the six-branch parameters followed by a second one related to the urchin-like conditions. These new hybrid structures mixing both materials and morphologies differently will provide interesting properties, achieve high performances and give great benefits to composite materials in a wide range of applications.

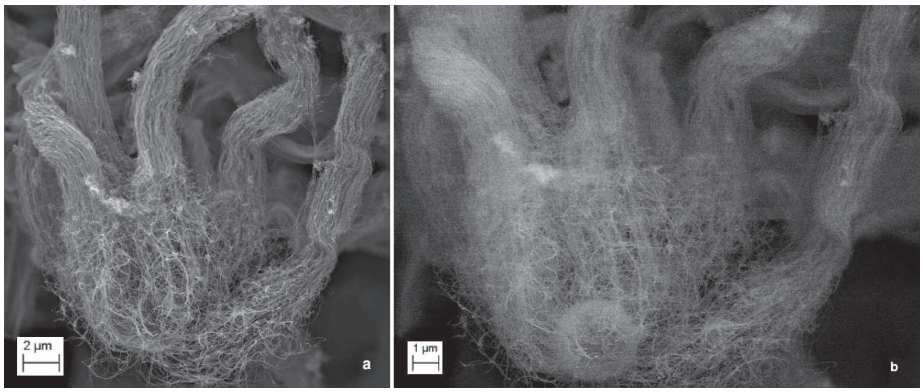

Figure 6.2.4: SEM images of a mixed morphology CNT-µ-Al_2O_3 hybrid structure synthesized by a first CVD sequence with acetylene at 750°C followed by a second one under the same conditions without acetylene.

6.3 CNT Growth kinetics

6.3.1 Steady state growth

As the CNT growth originates from the substrate, both carbon sources and catalyst precursors must penetrate pre-existing CNT layers to allow additional stacks to be synthesized. Louchev et al. [104] reported that the mean free path of the feedstock, which might be less than the average CNT spacing, could prevent it from reaching the catalyst. In such case, the diffusion resistance of the feedstock

from the top to the root might arise as an obstruction, and can act as a unique decelerating growth mechanism. In our case, high CNT density was reached and small indentations were observed on the top of most CNT branches on μ-Al_2O_3, as shown in the inset in Fig. 6.3.1a. The taller CNTs at the edge compared with those at the centre may suggest that the CNT growth rate is limited by the diffusion of growth species through the forest of CNTs, as explained by Louchev et al. [104].

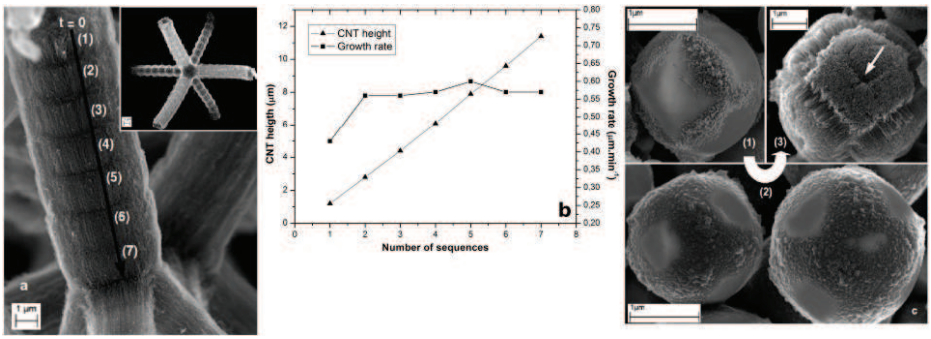

Figure 6.3.1: SEM image showing a six branch CNT structure on μ-Al_2O_3, where each branch is composed of a seven stack aligned CNT layers (a). The inset corresponds to 8 stacks of aligned CNT layers on μ-Al_2O_3. Each layer was synthesized under the same condition. Average CNT height and growth rate as the function of time (b). SEM images showing the growth chronology from 1 to 3 sequences of CNT multi-layers synthesized on μ-Al_2O_3 at 450°C (c) [31].

However, Fig. 6.3.1a shows CNT multi-layered structures, where each layer were synthesized under the same conditions. The dimensions, number of graphitic walls, orientations, densities and height of CNTs being all similar for all the layers, it indicates that the pre-existing layers do not influence the growth kinetics. Indeed, the growth rate remains constant during the overall process as shown in Fig. 6.3.1b. The small variations observed occur because the growth sequences were initiated and terminated manually. Only the top layer

corresponding to the first injection is slightly shorter. Hence, it clearly means that the CNT synthesis under our conditions is not limited by the transport of new feedstocks through the highly dense CNT forest. This is in good agreement with the non-dimensional modulus proposed by Xiang et al. [175] to evaluate the degree of the feedstock diffusion limit, showing that even for mm-scale MWNTs, no feedstock diffusion resistance occurs. The small indentations observed on some CNT/µ-Al_2O_3 hybrids are actually due to the substrate morphology rather than the feedstock transport through the CNT forest. Indeed, at the first sequence, when there is no such diffusion issue because the µ-Al_2O_3 particles have not been covered by CNTs yet, the CNTs start growing on the edges before expanding to broader regions, as depicted in Fig. 6.3.1c. This also explains why the top layer is slightly shorter than the others. Some crystal step sites have been identified at the edges of the 6 polar zones of µ-Al_2O_3, forming an inscribed cube on the µ-sphere particles, and leading to a CNT self-assembly which starts earlier at the edges than in the centre of µ-Al_2O_3 [63].

The CNT growth rate can be expressed as $r = k \cdot [P_{C_2H_2}]^n$, where k is the rate constant, $P_{C_2H_2}$ corresponds to the acetylene partial pressure, and n is the reaction order. The reaction order was determined at 823 K by changing the acetylene flow rate from 0.02 to 0.1 L/min. The resulting growth rate dependence on the acetylene partial pressure is plotted in Fig. 6.3.2a. The acetylene partial pressure was calculated by multiplying the acetylene molar ratio (acetylene flow rate divided by total gas flow rate in the reactor) by the total pressure (101.325 kPa). Since the growth rate increases linearly with the acetylene partial pressure, the reaction is first order (n=1) for each substrate (µ-Al_2O_3 and µ-SiC). This confirms that the CNT growth is not limited by the carbon diffusion. Moreover, according to the Arrhenius equation,

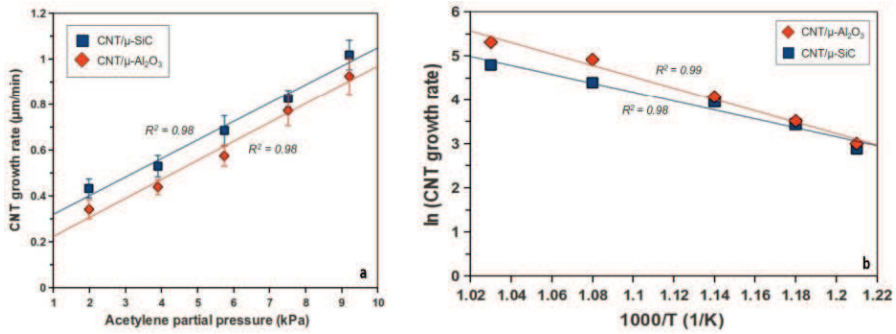

Figure 6.3.2: CNT growth rate at 550°C as a function of the acetylene partial pressure. Solid diamonds and squares represent the experimental data on μ-Al_2O_3 and μ-SiC respectively (a). CNT growth rate as a function of the temperature (b). The solid line is a linear fit of the natural logarithm of the growth rate as a function of the reciprocal of the absolute temperature. Diamonds and squares represent the experimental data respectively obtained on μ-Al_2O_3 and μ-SiC [31].

the rate constant can be written as k=A.e(-Ea/RT), where A is the frequency factor, Ea stands for the effective activation energy, r refers to the gas constant, and T is the absolute temperature. The plot ln(r) vs 1000/T, depicted in Fig. 6.3.2b yields a line with a slope of -Ea/R. The data fit well to a linear function (R_2=0.98) and from the slope the activation energy was determined as 1.2 eV (117.45 kJ/mol) for μ-Al_2O_3 and 0.95 eV (91.75 kJ/mol) for μ-SiC. Therefore, the CNT synthesis under the conditions detailed in Table 6.2.1 is first order with an activation energy of about 1 eV depending on the substrate. Similar studies reported an activation energy in the same range on bulk flat substrates [22] [20]. Finally, because of the intermediate temperature range used here, both bulk and surface diffusion are supposed to contribute to the CNT growth [29].

6.3.2 Growth termination

A good understanding of the CNT growth termination is of paramount importance to push the limits of the CVD process towards higher production yields. For instance, the synthesis of MWNT arrays on quartz from floating catalyst CVD at 750°C show a decelerating growth behaviour over long time, as depicted in Fig. 6.3.3. The CNT growth termination can be attributed to the catalyst deactivation arising from different phenomena which are usually divided into six categories: (i) the feedstock diffusion limit, (ii) the insertion of defects in the CNT structure, (iii) the catalyst reaction with its substrate, (iv) the catalyst NP coalescence, (v) hydrogenation of unsaturated hydrocarbon intermediates and (vi) the catalyst NP encapsulation by carbon.

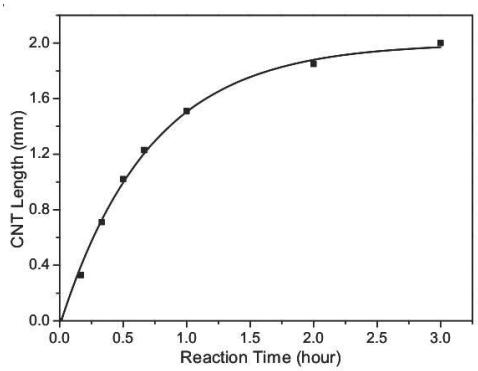

Figure 6.3.3: Time dependent growth of vertically aligned MWNT arrays on quartz.

Feedstock diffusion limit

As reported in section 6.1, the CNT bottom growth mode indicates that the feedstock molecules have to diffuse through the thick CNT forest, reach the substrate where catalysts locate, and then contribute

to the CNT growth. Therefore, diffusion limit of the feedstock from the top to the root of the CNT arrays may become a decelerating growth mechanism. In other words, the carbon source concentration at the CNT root might be lower than the bulk concentration, as illustrated in Fig. 6.3.4. Feedstock molecules diffuse from the top to the root of dense CNT forest, deposit and form solid CNTs while other gas byproducts like H_2 need to diffuse at the opposite direction from the root to the top.

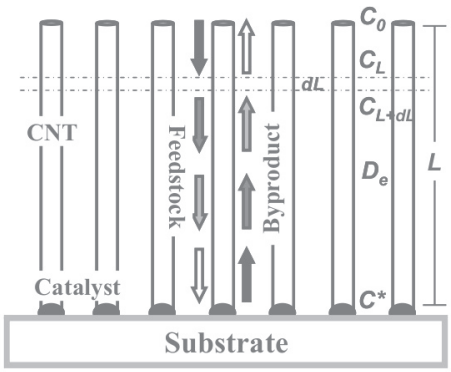

Figure 6.3.4: Schematic describing the diffusion of feedstock as well as gas product during the bottom-up CVD growth of CNT arrays [175].

However, we have shown in section 6.3.1 that the CNT synthesis under our conditions is not limited by the transport of carbon feedstocks through the CNT forest. Furthermore, Xiang et al. [175] proposed a one-dimensional (along the tube axis) diffusion model inside the CNT forest. The diffusion from the sides of the forest were neglected due to the higher collision frequency in the anisotropic structure of vertically aligned CNT forest. Therefore, in a small sliced CNT forest region dL (as indicated by dashes in Fig. 6.3.4), the difference in the amount of the feedstock diffusing in from the top and diffusing out from the bottom can be given by the expressions below according to Fick Law. It was assumed that the reaction is first order (as shown earlier) and

that at the CNT-substrate interface, the diffusion flux equals to the CNT growth rate.

$$D_e \cdot S \cdot \frac{dC_{L+dL}}{dL} - D_e \cdot S \cdot \frac{dC_L}{dL} = 0 \text{ (inside of CNT forest)}$$

$$D_e \cdot S \cdot \frac{C_0 - C}{L} = a \cdot S \cdot \frac{dL}{dt} = k_s \cdot S \cdot C^m \text{ (root of CNT forest)}$$

D_e is the effective diffusion coefficient, S is the film area, L is the CNT length, k_s is the constant reaction of carbon source to CNT, C is the effective feedstock concentration at the CNT root, m is the reaction order (in our case $m = 1$), and a corresponds to the structure constant of the CNT array. If further assuming that k_s is constant, the time dependent growth curve can be deduced as follow.

$$L = \sqrt[2]{\frac{D_e}{k_s}^2 + \frac{2 \cdot D_e \cdot C_0}{a} \cdot t} - \frac{D_e}{k_s} \tag{6.1}$$

Hence, depending on the values of $\frac{D_e}{k_s}^2$ and $\frac{2 \cdot D_e \cdot C_0}{a} \cdot t$, the CNT length, L, can be either proportional to t or t^2. The first case corresponds to CNT growth without diffusion limit, while the latter one relates the case of CNT synthesis strongly limited by the feedstock diffusion. Thus, applying this model to our CNT growth by floating catalyst CVD confirms that the diffusion limit is not the main reason for the decreasing growth rate, since the concentration at the root of array is almost the same as the bulk concentration. Xiang et al. [175] even show that the diffusion resistance in MWNT arrays can be neglected for CNT hight lower than 10 cm. Therefore, the decelerating growth behaviour observed in Fig. 6.3.3 may be due to a different termination mechanism.

Insertion of defects

The growth termination by the insertion of defects in the CNT structure was reported by Tomanek et al. [93] in the case of SWNTs. The catalyst allows the stabilization of an intermediate state before the final insertion of a hexagon in the CNT structure. The catalyst role is therefore twofold: it plays a role in the decomposition of carbon precursor and also in the healing of defects at the interface catalyst/CNT. Hence, the inclusion of defects in the CNT walls result of an error during this process [159]. The presence of a structural defect in the CNT structure, such as a pentagon or a heptagon rather than a hexagon generates a local change of curvature and the CNT becomes quite conical. Therefore, either another defect comes to compensate the previous one and the CNT can keep growing with a new chirality, or the CNT growth stops. Nevertheless, this deactivation mechanism was mostly observed for SWNTs, thus it may not be the main cause of deactivation in our conditions.

Catalyst reaction with substrate

Another source of deactivation is the reaction of the catalyst with its support, which prevents it from reacting with the carbon feedstock for further CNT growth. Such deactivation mechanism usually occurs at relatevily high temperatures, when the catalyst is more likely to diffuse into the bulk of the substrate, as already demonstrated by several authors [73]. One way to overcome this problem is the use of a thin coating layer to create a good diffusion barrier on the substrate. Materials like thermally oxidized SiO_2, MgO, ZnO, TiO_2 or Al_2O_3 are currently used. However, regarding the low synthesis temperatures used in this research, the catalyst reaction with the ceramic µ-particles is not believe to play a significant role in the growth termination.

Coalescence of catalyst particles

The coalescence of catalyst NPs was observed in the literature under typical thermal CVD conditions [3]. It is based on Ostwald ripening, which arises from the interaction between the catalyst NPs at high temperature. The larger particles being thermodynamically more stable, the small catalyst NPs will tend to disappear in favor of the bigger ones. Therefore, Ostwald ripening induces the decrease of the number of the catalyst NPs while their average size increases, thus leading to growth termination, as explained in Fig. 6.3.5. A mono-dispersed catalyst NP distribution can avoid Otswald ripening [15].

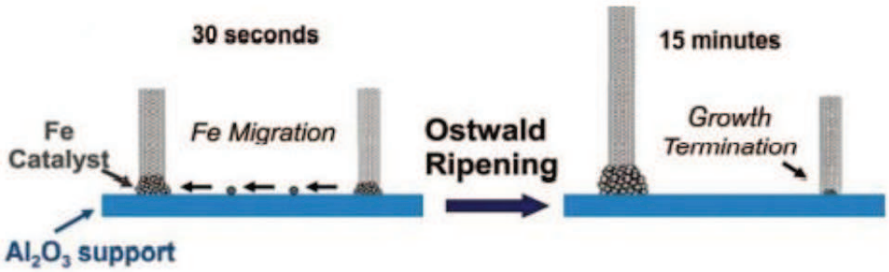

Figure 6.3.5: Schematic describing the Otswald ripening mechanism of catalyst during CNT growth by thermal CVD [3].

Hydrogenation of unsaturated hydrocarbon intermediates

During the growth of CNT multilayers by sequential injection CVD, the pre-existing CNTs and catalyst NPs were not responsible for the growth new layers. For instance, no differences in term of CNT length (about 4.2 m and 4.1 m) or layer numbers (1 layer for each sample)

were noticed between two samples prepared under the following conditions. Sample (a) was synthesized by one injection of both (C_2H_2) and ferrocene/xylene (see Fig. 6.3.6a), and sample (b) was collected after a first injection of both C_2H_2 and ferrocene/xylene and a second one of C_2H_2 only (see Fig. 6.3.6b). Since only one CNT layer was observed in sample (b), it means that during the second injection where only C_2H_2 was provided, the catalyst NPs deposited at the first injection do not catalyse the growth CNTs any more. A base growth mechanism being assumed, it thus indicates that the catalyst originated from the first injection have lost their catalytic activity after the first sequence and before the beginning of the second one. A 12 min pause was used to separate the sequences from each other as detailed earlier. During this pause, only Ar and H_2 were fed under the same flow rate, pressure and temperature as the rest of the synthesis. However, when H_2 was turned off during this pause (so only Ar remains) for the synthesis of sample (c), the growth of a new CNT layer was found, as depicted in Fig. 6.3.6c. Apart from the pause when H_2 was turned off, sample (c) was prepared under the same conditions as sample (b). Figure 2c reveals the growth of a stack composed of two CNT layers, while the total CNT length reaches about 5.5 m, which is longer than both sample (a) and (b). This means that the catalyst NPs from the first injection were still activated during the second injection if no H_2 is provided between the two sequences. Moreover, the comparisons of the CNT length for each sample reveals that no CNT were etched by the H_2 provided during the pause between two sequences.

In situ mass spectrometry analyses were performed to examine the catalytic activity during the second sequence of samples (b) and (c) respectively. Figure 6.3.7 shows the mass spectra *in situ* detected during the second injection of sample (b) (dashed line) and that measured during the second injection of sample (c) (straight line). The

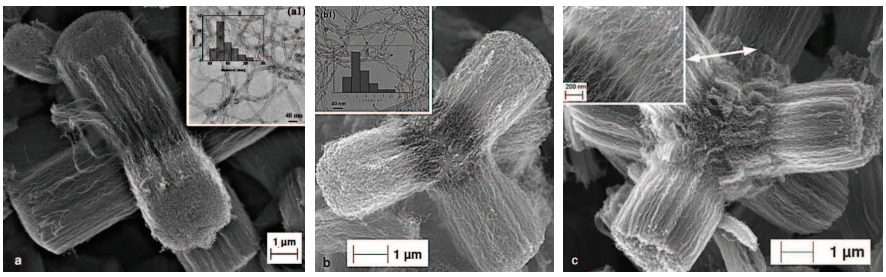

Figure 6.3.6: SEM images showing CNT grown on µ-Al_2O_3 (a) after a single 5 min injection of both C_2H_2 and xylene/ferrocene, (b) a 5 min injection of both C_2H_2 and xylene/ferrocene followed by a second one without ferrocene, and (c) under the same conditions as (b) but H_2 was turned off between the two injections.

mass spectra of C_2H_2 injected under similar conditions but without any trace of ferrocene in the reactor was used as reference (dotted line). The mass spectra corresponding to the second injection of sample (b) was very similar to that of C_2H_2 alone used as reference. Hence, it indicates that the C_2H_2 decomposition was not enhanced by the presence of catalysts deposited at the first injection of sample (b). In contrary, the C_2H_2 mass spectra intensity *in situ* detected during the second injection of sample (c) significantly dropped down. Compared to the reference spectra where C_2H_2 can only experience thermal dissociation, it means that the C_2H_2 during the second injection of sample (c) was decomposed further by the mean of the catalysts deposited at the first injection. Therefore, the catalyst NPs deposited at the first sequence under similar CVD conditions were still activated in the case of sample (c) but not for sample (b). These results perfectly matched with the electron microscopy observations.

The previous observations show that high amount of hydrogen can cause catalyst deactivation and thus growth termination. Hydrogen can induce changes in the catalyst structure. For instance, iron carbide

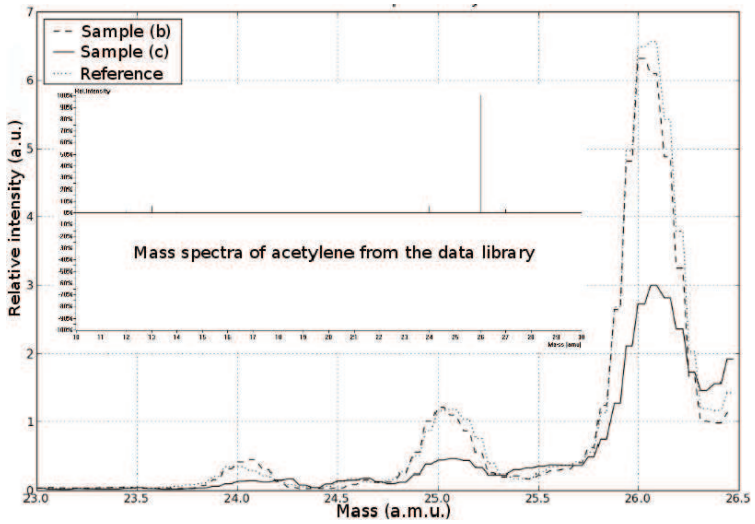

Figure 6.3.7: Mass spectra of the second injection of sample (b) (dashed line) and sample (c) (straight line). The mass spectra of C_2H_2 was used as reference (dotted line). The data library of C_2H_2 mass spectra is given in the inset.

(Fe_3C) catalyst could turn into pure metal iron (Fe) under reducing atmosphere and lead to catalyst deactivation [89]. Nevertheless, the catalyst phase during CVD growth remains an open question and both metal iron and iron carbide were found able to grow CNTs under similar conditions [6]. Moreover, this mechanism may not be likely, since the catalyst NPs are attached to the CNTs, which may prevent them from reacting further. Another possibility is ascribed to the hydrogenation of the unsaturated hydrocarbon intermediates to less reactive alkyl or alkanes intermediates. In the case of sample (b), the amount of H2 was significantly higher than that of Fe during the second injection. For instance, the H/Fe atomic ratio was estimated above 2000. Therefore hydrogen-induced reactions may react away the unsaturated carbon intermediates that are critical for CNT growth.

Catalyst encapsulation

Some carbon encapsulated catalyst NPs were observed in some samples, as illustrated in Fig. 6.3.8. The catalyst encapsulation consists of a thermodynamic mechanism. Since the CNTs are formed by dissolving, diffusing and precipitating the carbon atoms through the catalyst NPs, when the diffusing rate becomes higher than the precipitating rate, which occurs for small catalyst NPs or at high temperatures, the catalyst NP lose their catalytic activity. The carbon atoms accumulate on the particle surface as amorphous carbon and encapsulate the catalyst, preventing it from reacting with carbon feedstock, which terminates the CNT growth.

However, the temperatures previously reported for the CNT growth being quite low, the encapsulated catalyst NPs observed in Fig. 6.3.8 may not arise from the fast diffusion of carbon. As reported in Fig. 6.3.6c and 6.3.7, the catalyst NPs injected at the first sequence can still be activated during the next sequence if no H_2 is provided between the two injections. However, the second CNT layer in sample (c) grown during the second injection but from the catalyst NPs deposited at the first sequence is shorter than the other one. In this case, since the carbon feedstocks were still provided while the injection of catalyst precursors was stopped, the amount of carbon supplied becomes much more important than that incorporated by the catalyst NPs. Hence, carbon accumulates on the catalyst surface, subsequently increasing the formation of carbon islands on the catalyst NP, which eventually leads to the encapsulation of the catalyst.

Finally, another sample, (d), was prepared under the same conditions as sample (c), but ferrocene was injected back again during the second sequence. Figure 6.3.9 shows the growth a stack composed of

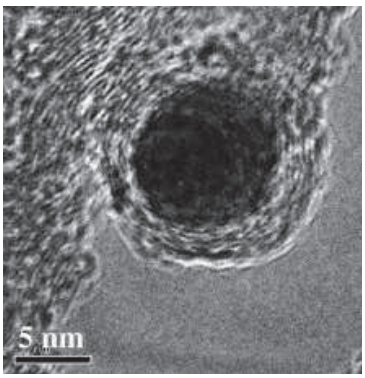

Figure 6.3.8: Carbon encaspulated catalyst particle observed by TEM.

three distinct CNT layers. According to the base growth mechanism, the growth of the middle layer can be attributed to the CNT synthesis during the second injection but from the catalyst NPs deposited at the first sequence. In the same way as for sample (c), the middle layer in sample (d) is shorter than the other ones due to the rapid encapsulation of the catalyst NPs deposited at the first injection. Furthermore, this indicates that a two injection CVD process can lead to a stack composed of either one, two or three CNT layers, revealing that the number of CNT layers does not necessary depend on the number of injections during the synthesis.

6.4 The lengthening and thickening method applied to the CNT growth by CVD

A simple and reliable method was proposed to prepare carbon nanotubes (CNTs) with uniform diameter and controlled wall numbers, from few layers up to several hundreds. Starting from CVD-grown CNT arrays with a given length and density, we show that the CNT wall numbers and inter-space can be precisely tailored, while the

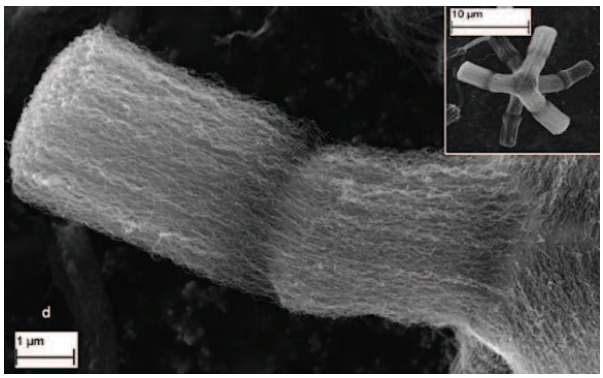

Figure 6.3.9: Sample (d): SEM images showing CNTs grown on µ-Al_2O_3 under the same conditions as sample (c) but ferrocene was injected back again during the second sequence.

vertical-alignment and length are preserved. The morphology of the thickened CNTs was investigated by electron microscopies, while the deposition of new concentric graphene structures was examined by thermo-gravimetric analysis, selected area electron diffraction, mass spectrometry and Raman spectroscopy. The involved mechanism of the CVD deposition of graphene on the CNT arrays was finally discussed.

The graphene deposition was conducted by a CVD method on vertically-aligned CNT arrays. A quartz plate supporting the CNT arrays was put in a quartz tube CVD reactor (45 mm in diameter and 1200 mm in length). Then, it was heated up by an electrical resistance furnace to 800 or 850 °C under argon/hydrogen (H_2, 30 vol.%) atmosphere. After 10 min for the system stabilization, the hydrocarbon, xylene $C_6H_4(CH_3)_2$ was injected at 0.2 mL/min in the form of spray, along with acetylene C_2H_2 at 0.05 L/min. Here, the injection of liquid xylene and the gases were controlled by a mechanical syringe system fitted with a liquid flow meter (Razel Science, R99-E), and by digital mass flow meters (Bronkhorst), respectively. The

total gas flow was kept to 1 L/min during the overall process. The deposition time was varied from 5 to 20 min. At the end, the reactor was cooled down to room temperature under argon atmosphere at 1 L/min.

The vertically-aligned CNT arrays used in this study were synthesized by catalytic CVD on 1 cm^2 quartz plates, as detailed above. The as-prepared CNTs exhibit homogeneous diameter about 14 nm. The length of these CNT arrays can be controlled by tuning the reaction time as reported earlier. The CNT arrays used in this research were about 350 µm in height.

6.4.1 Morphology of the thickened CNTs

Figure 6.4.1 presents SEM images of the pristine CNTs and the thickened ones. It clearly shows that the CNT diameter becomes significantly bigger after the thickening process, while the CNT length remains constant presumably due to catalyst deactivation by carbon encapsulation after CNT growth. In addition, a bottom up CNT growth mechanism was reported earlier under similar conditions [31]. Since there is no catalyst precursor provided during the thickening process, the CNTs can no longer grow from the catalyst particles. Moreover, most of the CNT ends were found to be closed and even if some were open, they would probably be terminated by -COOH and/or -OH functional groups, avoiding further CNT cloning through the catalyst-free open-end growth mechanism reported by Yao et al. [181]. The thickened CNTs also keep their vertical-alignment as depicted in the insets. Moreover, Fig. 6.4.1b indicates that the CNT inner diameter remains the same after thickening. It also reveals that the diameter enlargement is ascribed to the addition of a continuous

carbon layer all around the pristine CNTs, rather than the coalescence of several original tubes. This means that the CNT density is also preserved during the process. Hence, these additional layers can be assimilated as a carbon sheath around the original CNT cores, like reported by Hu et al. [67] with silicon dioxide.

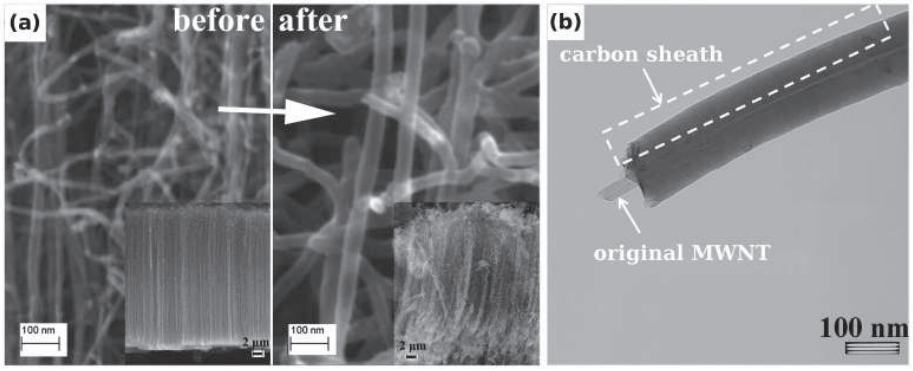

Figure 6.4.1: (a) SEM images of the CNT arrays before and after graphene deposition. The CNT diameter obviously increases, while the CNT height remains the same. (b) TEM micrograph of a MWNT after 20 min treatment. The original CNT is visible at the apex of the structure.

The electron microscopy observations show that the CNT diameter increases with the deposition time, while its distribution remains homogeneous (please see supporting informations). The CNT mean diameters were thickened from 14 to 35, 62, 80, and 114 nm after 0, 5, 10, 15 and 20 minutes, respectively. A linear correlation ($R^2 = 0.98$) between the CNT diameter and the deposition time was found, as plotted in Fig. 6.4.2. Therefore, the CNT outer diameter can be homogeneously and precisely monitored in a large scale by the addition of a carbon sheath on the CNT surface. Moreover, the CNT density being constant during the CVD process, it reveals that the CNT inter-space reduces with the increase of the CNT diameter.

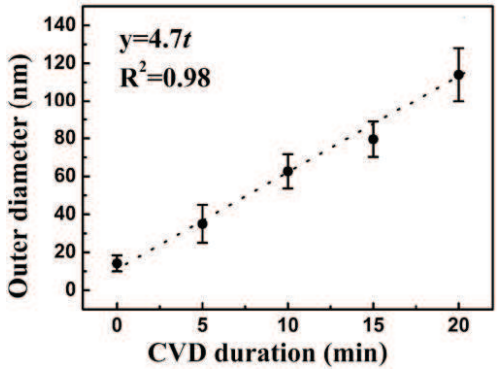

Figure 6.4.2: Variation of the CNT diameter with the deposition time. The error bars correspond to the diameter distribution.

6.4.2 Structure of the carbon sheath deposited on the CNT surface

Further investigations were performed to examine the structure of the deposited carbon sheath. Figure 6.4.3 shows the differentiated TG (DTG) curves of the pristine CNT arrays, the ones thickened after 10 min at 800°C and after 10 min at 850°C. The weight loss of the material is due to the combustion of carbon. Apart from the thickened CNTs at 800°C, no peak can be located in the temperature range between 200°C and 400 °C, indicating that both the pristine CNTs and the ones thickened at 850°C are nearly free of amorphous carbon [150]. The other peak near 600-700°C is attributed to the oxidation of CNTs. This oxidation peak was found at 610°C for both the pristine CNTs and the ones thickened at 800°C, while it is about 640°C for the those thickened at 850°C. Therefore, the thickened CNTs at 850°C being nearly free of amorphous carbon, this shift toward the higher temperatures indicates an increase in the number of CNT walls.

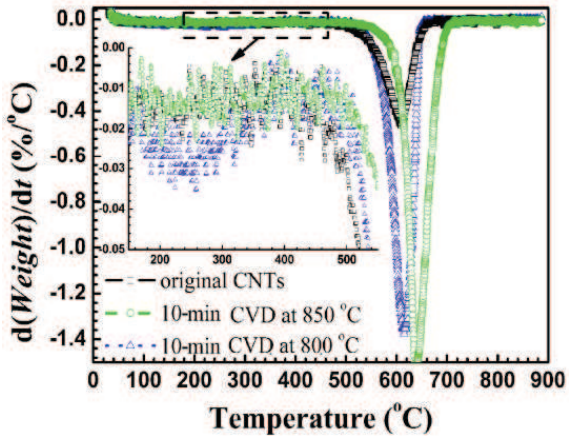

Figure 6.4.3: DTG curves of original CNT arrays (black), CNTs thickened during 10 min at 800 °C (blue) and during 10 min at 850°C (green). The samples weight were about 10 mg, heated up at 20 °C.min^{-1} in air from 30°C to 900°C.

Figure 6.4.4 shows the SAED patterns of the CNT arrays before and after thickening. The SAED pattern of the thickened CNTs (Fig. 6.4.4b) does not exhibit any diffraction rings of amorphous carbon [98], while it shows a high similarity with that of the original CNTs (Fig. 6.4.4a). Both SAED patterns present one pair of small but strong arcs of 002 reflections [149], revealing graphite-like concentric cylindrical structures.

Furthermore, high resolution images (Fig. 6.4.5) confirm the graphite-like structure of the thickened MWNTs, meaning that they can be considered as high quality ones. In addition, the insets in Fig. 6.4.5 show that a nearly monodispersed diameter distribution is maintained after the thickening process, while the average diameter was multiplied by 2 (Fig. 6.4.5b) and 4 (Fig. 6.4.5c) after the graphene deposition. The corresponding CNT diameter distributions can be seen

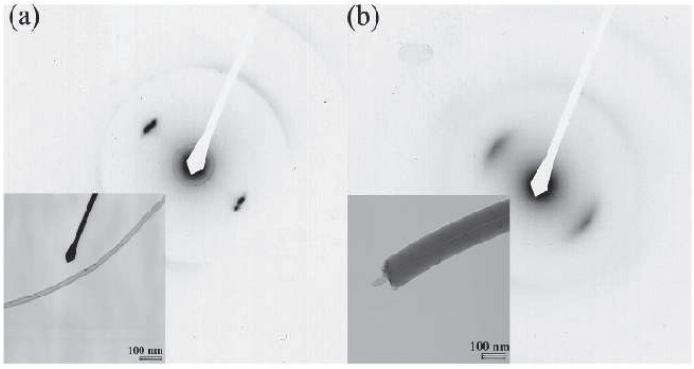

Figure 6.4.4: Selected area electron diffraction patterns of an individual pristine CNT (a) and a single thickened one (b). The corresponding TEM images are depicted in the insets.

in Fig. 6.4.5d.

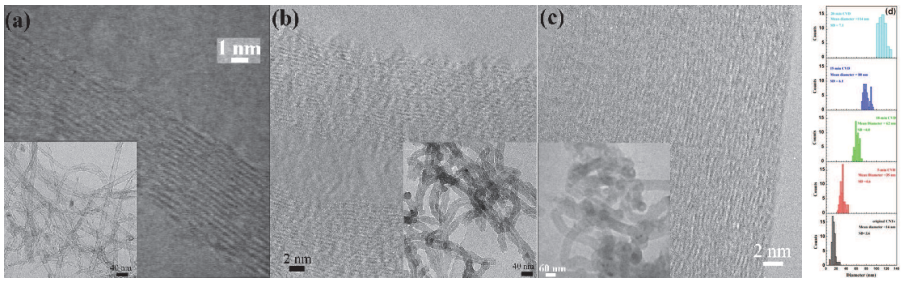

Figure 6.4.5: High resolution TEM micrographs of pristine CNTs (a), CNTs thickened after 5 min (b) and after 10 min (c) of CVD graphene deposition at 850 °C. The corresponding CNT diameter distributions are shown in (d).

The CVD condition of the graphene deposition significantly affects its structure. For instance, higher temperatures favour the formation of defect-free graphene layers, while low temperatures decrease their graphitization degree and induce the formation of amorphous carbon. When the graphene deposition is performed at temperatures below 850 °C, a peak corresponding to amorphous carbon is detected by TGA around 250°C, as shown in the inset

Fig. 6.4.3. The deposition time was also found to influence the graphene structure. Indeed, for deposition times longer than 10 min, the average interlayer spacing between the graphitic walls tends to slightly increase to 0.35 nm, compared to 0.34 nm for the pristine CNTs [24] and the thickened ones below 80 nm in diameter. In addition, such largely thickened CNTs exhibit curved segments of individual graphitic sheets and discontinuous graphitic cylinders, which is a form of disorder in graphene layers. Nevertheless, it is worthwhile to mention that this kind of defects is also usually present in large-diameter MWNTs directly prepared by typical CVD process and can be efficiently healed by annealing under inert atmosphere at elevated temperatures [24]. Such thermal treatments were found to increase the ordering state of the CNTs by reducing the layers' defects as well as regulating the interlayer spacing between the graphene shells.

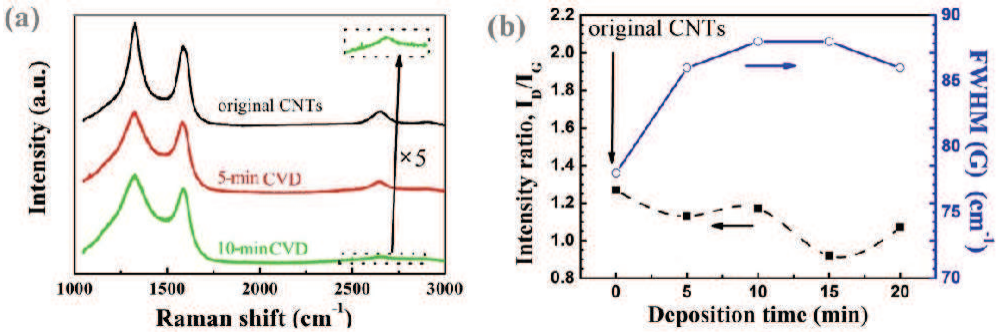

Figure 6.4.6: Evolution of the CNT Raman spectra (a), the intensity ratio of the D and G bands (I_D/I_G) and the full-width at half-maximum (FWHM) of G band (b) as a function of the deposition time.

Raman spectroscopy analysis was performed in the range of 1050-3000 cm$-^1$ in order to check the structure differences between the thickened CNTs and the pristine ones. The Raman spectra depicted in Fig. 6.4.6a were obtained using an excitation wavelength of 632.8

nm. Both specimens (pristine and thickened MWNTs) exhibit two first-order peaks centered around 1325 cm$-^1$ and 1585 cm$-^1$, corresponding to the typical D and G bands of MWNTs, respectively. The G band is commonly attributed to the sp2-bonded carbon, while the D band stands for the scattering of sp^3-bonded carbon plus a possible contribution of the disordered sp^2 phase [24]. In graphite-like carbon, the D band originates from the structural defects, and the intensity ratio of the D band over the G band (I_D/I_G) is commonly used to quantify the CNT structural quality [86]. A lower I_D/I_G ratio suggests fewer structural defects in CNTs as well as higher purity [86]. Here, the I_D/I_G ratios of the thickened MWNTs, plotted in Fig. 6.4.6b, are in the same range as the ones of pristine MWNTs [86]. In addition, the evolution of the I_D/I_G ratio with the graphene deposition time is in the same range as that between pristine MWNTs originating from different CVD batches under similar conditions. Furthermore, the full-width at half-maximum (FWHM) of the G band, plotted in Fig. 6.4.6b can be used to determine the CNT crystallinity degree [86]. The thickened MWNTs are a little less ordered than the pristine ones since the G band FWHM increases from 78 to 86 cm$-^1$ after the thickening no matter the deposition time. A similar conclusion can be drawn from the study of the second-order peak at 2700 cm$-^1$, depicted in Fig. 6.4.6a. This peak is usually assigned to 2D vibration and an increase of this 2D band can be interpreted as a better ordering of the graphitic structure [86] [24]. As shown in Fig. 6.4.6a, the 2D band tends to be weakened with the increase of the deposited graphene layers, suggesting a slight decrease in the graphitic perfection of the thickened MWNTs when the graphene deposition time increases. This can be also observed in Fig. 6.4.5c, where the thickened CNT exhibits a pitted graphitic surface.

6.4.3 Mechanism of the graphene deposition

The above analyses unambiguously demonstrate that the thickened CNTs can be considered as high quality CNTs. The CNT length was found to remain constant, while the CNT diameter linearly increased during the process. The deposited graphene layers present nearly the same concentric graphitic cylinder structure as the pristine MWNTs. Therefore, the CNT thickening is ascribed to the growth of graphene layers on the CNT outer wall. Hence, the slope deduced from the curve in Fig. 6.4.2 indicates that the CNT diameter increases at a rate of 4.7 nm per minute, corresponding to the formation of about 7 concentric graphene sheets per minute (each graphene cylinder contributes for 2 x 0.34 nm to the CNT diameter). Therefore, we can determine the number of carbon atoms per minute needed for this synthesis (Fig. 6.4.7), using the equation (1), where $N_C, M_C, N_A, N_{CNT}, \mu CNT, L_{CNT}$and r_{CNT} respectively refer to the number and the molar mass of carbon atoms, the Avogadro constant, the number, density, length and radius of CNTs.

$$N_C = \frac{N_A \cdot N_{CNT} \cdot \mu_{CNT} \cdot L_{CNT} \cdot r_{CNT}^2}{M_C} \tag{6.2}$$

Since a fixed amount of carbon precursors was continuously provided into the reactor, we can assume that the number of carbon atoms available in our system is constant under a stable condition. We consider the non-catalytic carbon precursor decomposition under our CVD conditions according to the model reported in Chapter 4. Under such conditions, methane CH_4 and benzene C_6H_6 were found to be the two main hydrocarbon species present in the gas phase after equilibrium, as detailed in Fig. 6.4.8a. This is in an excellent agreement with in situ mass spectrometry analysis (Fig. 6.4.8b), showing that the two main hydrocarbons detected in the gas phase under these

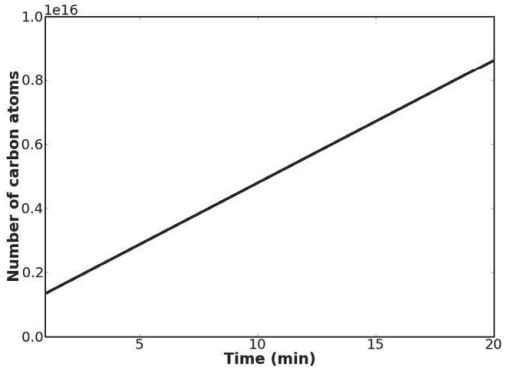

Figure 6.4.7: The calculated number of carbon atoms needed for this synthesis as a function of time. The CNT bulk density was estimated by counting the number of CNTs in 1 μm.

conditions correspond to CH_4 (peak at 16 a.m.u.) and C_6H_6 (peak at 76 a.m.u.). Hence, the number of carbon atoms per minute available into the reactor can be estimated about 1021, which is much larger than that needed for the graphene formation determined in Fig. 6.4.7. Nevertheless, no amorphous carbon was detected whereas the number of carbon atoms is much higher than that necessary for the graphene formation. This may be due to the high partial pressure of hydrogen in the CVD reactor which prevents the formation of higher aromatic carbon rings from agglomeration of lower hydrocarbon molecules at high temperatures. Therefore, the gas-phase reactions are not the limiting step of the CVD graphene deposition. Furthermore, relatively uniform graphene layers were observed (Fig. 6.4.5) indicating that the graphene growth rate along the tubes must be much quicker than its nucleation rate. In other words, the nucleation should be the rate determining step under our CVD conditions, as also reported by Negishi et al. [123] on flat silicon substrate.

However, the largely thickened MWNT surface in Fig. 6.4.5c is

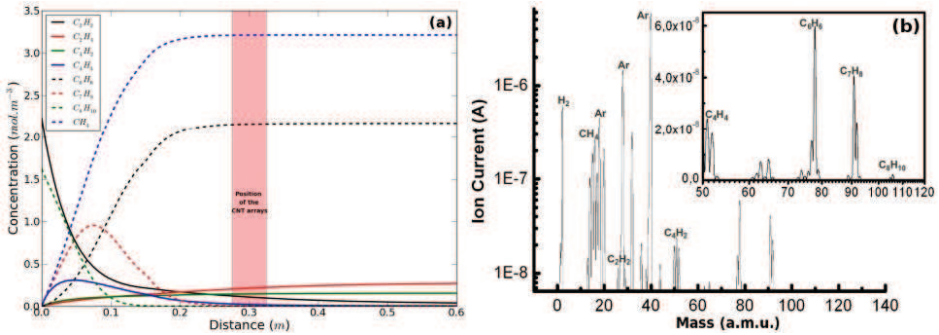

Figure 6.4.8: (a) Modelisation of the evolution of the different hydrocarbon species at 850 °C as a function of the position in the CVD reactor. (b) *In situ* mass spectrometry analysis of the gas phase at the center of the CVD reactor.

not perfect, showing a pitted graphitic surface, which may induce the decrease of the 2D band observed by Raman spectroscopy in Fig. 6.4.6a. This might be due to the inhibiting effect of hydrogen. Hydrogen was found to drive the reverse reaction due to the gasification of the deposited carbon, as reported elsewhere [180]. Actually, the relatively high concentration of CH_4 detected in the gas phase by MS may partially result from this phenomenon. Therefore, the deposition of high quality graphene layers might be resulting from a competition between the dehydrogenation of hydrocarbons like C_6H_6, and the hydrogen-induced gasification of the deposited carbon on the CNT surface. Finally, the overall mechanism of the graphene deposition on CNT arrays by CVD is summarized in Fig. 6.4.9.

6.5 Summary

In general, the amounts of CNTs synthesized on flat substrates are typically as small as a few tens of $g.m^2$, which remains the major obstacle for industrial nanotechnology applications based on CNTs. In

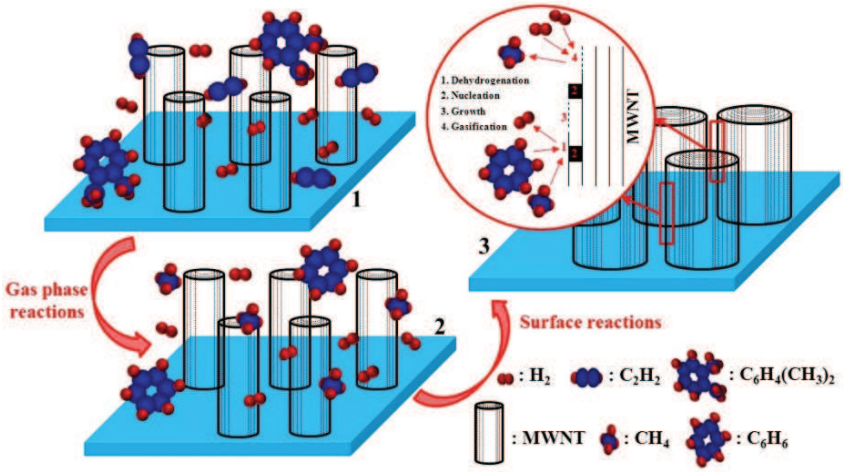

Figure 6.4.9: Schematic of the graphene deposition resulting to homogeneous variation of CNT diameter and inter-space.

this Chapter, the synthesis of high purity vertically-aligned MWNTs on non-flat µ-sized ceramic particles showed a promising approach for CNT mass production, due to higher substrate surface/volume ratio. The advantage of the CNT synthesis on such kind of materials is therefore twofold: it allows both to achieve large amounts of CNTs to reach industrial purposes and to improve the composite properties thanks to the hybridization of CNTs with µ-particles (e.g. see Chapter 1.4). Furthermore, the CNT stack formation method by sequential injection CVD up to eight layers in one batch was tailored to explore the effects of several CVD parameters on the CNT structures and growth kinetics. A base growth mechanism, similar to the one reported by the labelling method [134], was unambiguously identified. Six different growth termination mechanism were then proposed and thoroughly discussed.

Finally, the deposition by CVD of a controlled number of concentric graphene layers has been reported on CNTs. The high quality

graphene layer formation results in an effective thickening of the CNT diameter and thus decreasing the CNT inter-space in the carpet film. The graphene deposition is due to the decomposition of hydrocarbons followed by the nucleation and growth of graphene on the CNT surface and then on the new formed graphene layers in which the nucleation was found to be the rate determining step. Therefore, we demonstrated the opportunity of a simple and reproducible CVD method to precisely control the CNT structure. Indeed, in the linear lengthening growth stage, the CNT wall number remains constant and the catalysts preserve their activity, while in the thickening stage the CNTs thicken substantially through gas phase-induced graphene deposition. Various kinds of CNTs with different aspect ratios can be thus achieved to prepare a wide range of nano-devices for multiple applications. This approach can also be extended to the production of hybrid nanostructures, where a specific coating would be incorporated in between graphitic or amorphous carbon, opening up exciting opportunities for future fundamental studies and practical applications.

He who knows best knows how little he knows

Thomas Jefferson

7 Conclusions

7.1 Summary

The structure of this research has been organized to follow the chronology of the CNT formation by floating catalyst CVD. Six major steps were identified as summarized in the graphical abstract. The first one consists of the injection of catalyst and carbon precursors into the CVD reactor in the form of spray. The different injection factors such as the gas flow, the liquid flow or the type of injector were found to significantly influence the evolution of the precursors into the reactor. The aerosol was found to be composed by heterogeneous droplets inducing coalescence in the first part of the reactor. Depending on the conditions, the size of the precursors appears as a critical factor to monitor the resulting CNT diameter. Then, the

droplets evaporate in the high temperature furnace where NPs form and nucleate. NP agglomeration was suggested under certain CVD conditions. Meanwhile, pyrolysis and/or catalysis reactions occur leading to new species which are able to promote the CNT growth. The CNT formation can thus take place on the substrate surface. The substrate nature and morphology was found to strongly influence the CNT formation. However, the CNT nucleation and growth remains unclear and various mechanisms were proposed. The so called adsorption-diffusion-precipitation process followed by the screw dislocation-like model described the CNT nucleation and elongation respectively, while the particle wire-tube-mechanism seems to be more appropriate in the case of floating CVD. Finally, CNT growth termination can be attributed to the catalyst deactivation arising from different phenomena which can be divided into six categories: (i) the feedstock diffusion limit, (ii) the insertion of defects in the CNT structure, (iii) the catalyst reaction with its substrate, (iv) the catalyst NP coalescence, (v) hydrogenation of unsaturated hydrocarbon intermediates and (vi) the catalyst NP encapsulation by carbon.

In situ diagnostics have been extensively used in this research to better understand the NP formation and the CNT growth mechanism. Laser-based characterization methods, such as TRLII and LIBS, were applied for the first time to study the CNT growth by a typical floating catalyst CVD process. Moreover, floating catalyst CVD has been applied in this research to grow CNTs mainly on µ-scale platelets or beads. Such method exhibits multiple advantages: it provides both a promising approach for CNT mass production and high-performance, multi-functional, environmental friendly (this last point will be discussed further at the end of this Chapter) reinforcements for composite materials and their applications.

7.2 Discussion and future works

This research covers three main aspects that can be deepen further for future developments of CNT-based technology.

First, the use of real-time *in situ* diagnostics is, to my mind, the most appropriate way to understand the overall CNT growth mechanism and unravel some of the questions that still remain open issues. Nevertheless, due to the dimension range and the time scale involved in the CNT formation, more especially in the early stages of the synthesis, direct experimentations have to be coupled with theoretical calculations and numerical simulations.

Furthermore, the CNT hybridizations with other materials were found to form numerous promising multi-scale combinations that can benefit to a wide range of applications. However, a strong CNT adhesion on the substrate is mandatory to allow a good dispersion of the structures on the polymer matrix, while it will also provide a potential solution to CNT safety issue since the integrated hybrid structures exhibit larger dimensions and high bulk densities compared with stand alone CNTs which are potentially hazardous due to their nano-dimensions, as mentioned in the next section.

Finally the continuous CNT growth by floating CVD was shown to be a high yield, cost saving and easily scalable process. Nevertheless, further work has to be done to improve the control over the CNT structure and more especially the CNT chirality in the case of SWNTs. Therefore, based on these various aspects, the following points will be interesting for future research:

- **Laser-induced fluorescence (LIF)** coupled with TRLII can be

used to study the particle formation. The presence of iron atoms and carbon radicals in the gas phase can be detected by LIF which would confirm a nucleation mechanism by vaporization and condensation.

- **LIF can be also used** to validate a more detailed and complete model of the chemical reactions in the gas phase. Surface reactions could be added to this detailed model, but it would require informations about the reactions kinetics which are not yet avalaible in the litterature.

- **The NP sizes determined by TRLII** in this research correspond to an average over the volume of the laser beam. In Chapter 3 the agglomeration of suspended NPs in the gas phase was suggested. Hence, the suspended NPs size distribution is of paramount importance to validate the agglomeration process. It can be determined directly from the TRLII signals by a multi-exponential fit. Based on the method proposed by Brubach et al. [17], we ran some theoretical simulations to validate the possibility to determine the NP distribution from a typical TRLII signal. The results showed that if the difference between the NP size of each mode is in the range of few nm (e.g. about 3 nm), while the density of the bigger NPs is lower than that of the smaller ones, two different modes will be successfully distinguished using the multi-exponential fitting method. However, due to the presence of noise in the experimental signals, the method was not able to provide workable outcomes. Therefore, the experimental setup has to be improved with focusing lenses and different filters to maximize the signal/noise ratio in order to apply this multi-exponential fitting method.

- **A new theoretical model** based on laser-induced CNT heat transfers can be developed to allow the characterization of CNT arrays by TRLII. This model coupled with the multi-exponential fitting method would provide a fast and efficient way to scan the CNT diameter distribution over large surface areas.

- **As reported in Chapter 3**, the nature of the suspended particle cannot be identified by the *in situ* diagnostics proposed in this research. The NP nature, chemical composition and physical state are critical points in the CNT growth mechnanism and should be investigated in detail in a future work. An interrupted synthesis method can be established for further *ex situ* analysis by HRTEM and EELS, while Launois et al. [89] recently reported an *in situ* time resolved X-Ray diffraction system.

- **In Chapter 2,** the use of LIBS was found to interfere with the CNT growth due to the generation of new reactive species induced by the plasma. Therefore, LIBS cannot be used as an *in situ* non-intrusive diagnostic method to study the CNT growth under typical floating CVD conditions. However, it may provide a new way to synthesize CNTs at temperatures below 500°C, as suggested in Chapter 2. Besides lower reaction temperatures, another advantage of such laser-assisted floating CVD, arises from the precise control of the CNT self-assembly location, happening at the immediate vicinity of the laser-induced plasma [14]. Hence, the laser-assisted floating CVD technique might benefit to various applications related to CMOS technology, where low temperature and high space-resolution processes are

critical.

- **As mentioned in Chapter 6**, the growth kinetics is not constant during the CVD synthesis. Therefore it would be desirable to use a camera to take *in situ* videos of the growth of CNT arrays and record the CNT growth rate as a function of time under different conditions. This project is currently ongoing in our lab.

- **Whereas floating CVD is** considered as a continuous process, the genuine continuous production of CNTs or CNT-based materials without interruption has not been achived yet in this research. However, Chapter 6 revealed a promising approach for CNT mass production based on µ-sized substrate with a large surface/volume ratio. Therefore, a scaled-up fluidized bed reactor with continuous feed of both catalyst precursor(s), carbon source(s) and µ-sized substrates would bring our CVD process a step closer to potential industrial applications.

- **Finally, the nanotube technology** may present some risks making the precautionary principle a necessity when working with CNTs. Further investigations related the CNT-hybrid toxicity have to be conducted based on the results reported below.

7.3 Last but not least: health and environmental considerations

Apart from the technical and economical challenges related to the industrial production of CNTs [176] and the application of CNT-based devices mentioned in this thesis, there is another important issue dealing with the health and environmental aspects. Are the CNTs sufficiently safe for workers and consumers? Since the CNT production increases every year (about hundreds of tons per year), the risks due to the exposure of CNTs within occupational, environmental and consumer settings must be taken into account. It highlights the need of understanding the CNT behaviour with its environment. Informations on the CNT toxicity and biocompatibility has become gradually available within the past few years. However, any conclusive remarks were clearly drawn which is not surprising as the number of different types of CNTs is large (SWNTs, MWNTs, catalyst-free CNTs, vertically-aligned CNTs, entangled CNTs, ultra-long CNTs, functionalized CNTs...). Although further investigations are required, increasing studies suggest that CNTs are potentially hazardous to humans and are often assimilated to asbestos.

According to several researchs, two main ways of toxicity were identified. In one hand the pulmonary toxicity (volatile) which induces inflammation and difficulties to breath, and in the other hand the skin toxicity (contact) leading to irritations and apoptosis (cell death). In the first case, *in vivo* studies conducted using intratracheal instillation on various animals show that CNTs can lead to inflammation and fibrotic reaction [11]. In addition, if the CNTs reach the lungs in sufficient quantities after inhalation, they can induce a toxic response including the formation of granulomas and even premature death [136]. In the latter case, *in vitro* investigations clearly show that under

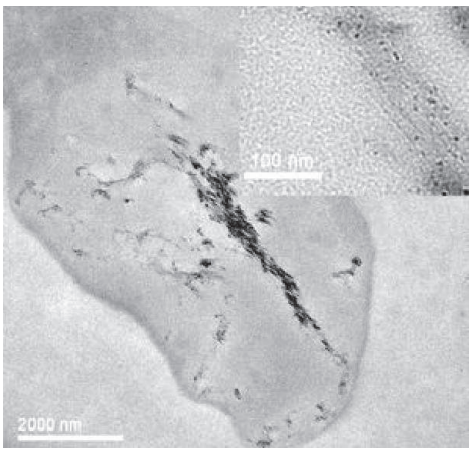

Figure 7.3.1: TEM image showing CNTs within a cell nucleus [137].

some conditions, CNTs can cross cytoplasm and nucleus of human immune cells, such as macrophages, as depicted in Fig. 7.3.1. Significant mortality of cells was observed for samples with high CNT density [137].

Magrez et al. [105] found different origins to explain the toxicity of CNTs. The first and the main one is due to the catalyst NPs enclosed in the tubes. These NPs are often made of heavy metals which can be a source of contamination and toxicity. The second important aspect to take into account for a better understanding of the CNT toxicity and more particularly cytotoxicity is the CNT morphology. It was shown that long nanotubes are more toxic than short ones. while the CNT toxicity tends to decrease with the increase of the CNT diameter. For instance, mice treated with long CNTs show a progressive accumulation of CNTs in the mesothelium of the chest wall, while the thickening of the pleural layer with short CNTs returns to normal after 7 days, as depicted in Fig. 7.3.2. In the first case, the CNTs are too long to be completely engulf, triggering an immune response that can cause repeated inflammation as illustrated

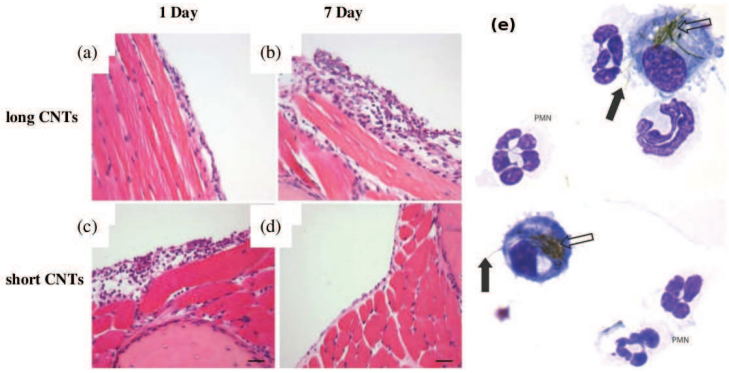

Figure 7.3.2: Images of histological sections through the chest wall of mice treated with long CNTs (a, b) and short CNTs (c, d) after 1 and 7 days (scale bars represent 20 µm). (e) Frustrated phagocytosis and the associated acute inflammatory reaction in bronchoalveolar lavage of mice whose lungs have been instilled with long CNTs [136].

in Fig. 7.3.2e. Moreover, the CNT agglomeration state is a very important factor as well. For instance, entangled CNTs seems to be more toxic than individual CNTs. Furthermore, the many variations of functionalized CNTs may be seen as new chemical strutuctures with their own potential risks. Hence, the rate of functionalization influences the CNT toxocity. Nevertheless, when the functionalization degree increases, the CNT toxicity was found to decrease. It seems that chemical functionalization tends to passivate the CNTs, as reported by Dumortier et al. [40].

As reported earlier, one solution to overcome the CNT hazard consists of the CNT hybridization with bigger particles allowing to reduce the CNT exposure by increasing the size of the final structure making it less volatile and unlikely to enter into cells. This requires a strong anchoring of the CNTs on their substrate. However, ultrasonication tests performed on CNT/µ-Al_2O_3 hybrids as reported in Chapter 6, showed that it is relatevely easy to detach the CNTs from their

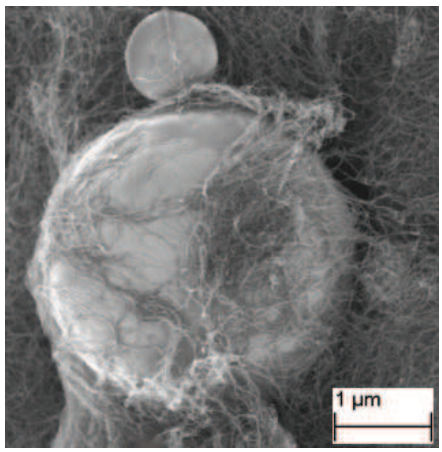

Figure 7.3.3: SEM image of CNT/µ-Al_2O_3 hybrids after 5 min ultrasonication at 20 W.

support, as depicted in Fig. 7.3.3. Hence, the CNTs separated from the substrate can no longer be considered as a µ-structure and become potentially hazardous as reported above.

Since the best solutions can be usually found in Nature, biomimetics concepts will be applied to overcome this issue. In this case, the model for anchoring vertically-aligned tubes on spherical particles is given by sea urchins. These animals are composed of three main parts: the internal organs, the hard exoskeleton and plenty of tube feet. The hard exoskeleton plays the role of fixing the tubes on the internal organs. Therefore, one element is missing on our CNT/µ-Al_2O_3 hybrid structure to copy the sea urchin. A shell is needed to anchor the free-standing CNTs with the rest of the structure. The graphene deposition process described in Chapter 6 can be thus used to better affix the CNTs on their support without deteriorating the hybrids' properties, such as the electrical and thermal conductivity. Hence, graphene layers were deposited under the conditions detailed in Chap-

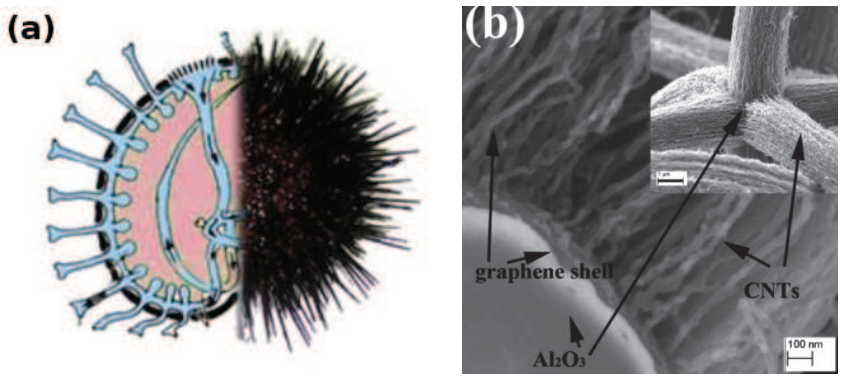

Figure 7.3.4: Schematic of the structure of a sea urchin (a). SEM image of CNT/μ-Al_2O_3 hybrids after the deposition of a graphitic shell by floating CVD (b).

ter 6 on CNT/μ-Al_2O_3 hybrids initially synthesized by floating CVD, as reported in Chapter 6 as well. Figure 7.3.4 shows the comparison between a see urchin and the as-prepared hybrid structure. Moreover, it was found that the carbon shell deposited on the μ-particle exhibits the same nature as that on CNTs. In addition, the thickness of the graphitic shell, both on the μ-particles and on the CNTs, linearly increases with the deposition time in a similar way as reported in Chapter 6.

The evolution of the CNT/μ-Al_2O_3 hybrids' morphology was investigated after ultrasonication at different powers. While most of CNTs were detached from the Al_2O_3 surface at the lowest power (see Fig. 7.3.3), the deposition of about 20 nm thick graphitic shell allows to maintain the hybrid structure free from damages even at the highest ultrasonic power as depicted in Fig. 7.3.5.

Therefore, similarly as the sea urchin hard exoskeleton, the graphitic shell successfully prevents the CNTs from being torn apart.

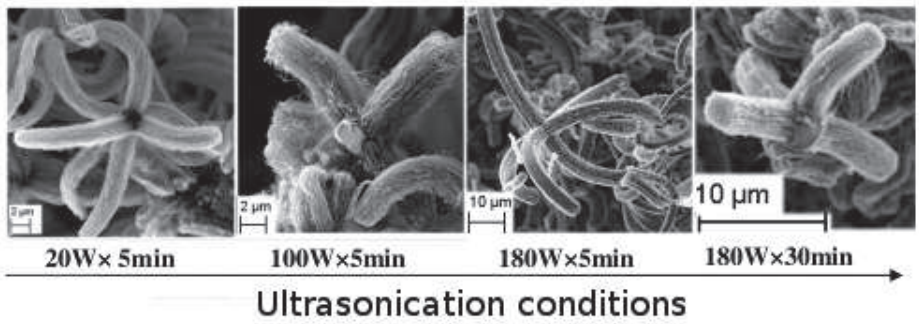

Figure 7.3.5: Evolution of the CNT-µ-Al_2O_3 structures after the deposition of a graphitic shell as a function of the ultrasonic power.

Furthermore, even if the hybrids are not totally free from damages after ultrasonication as depicted in the right image in Fig. 7.3.5, the CNTs separated from the main structure remain at the micro-scale thanks to the graphitic shell. Fig. 7.3.6 shows that the CNTs were still attached to the part of the graphitic shell which was seperated from the main structure. The detached CNTs arrays being affixed to the graphitic shell (see inset in Fig. 7.3.6), the separated part can still be considered as a µ-scale hybrid like small CNT/GN structures reported in Chapter 5. Nevertheless, even if this method seems quite efficient to avoid to spread individual CNTs in the atmosphere, the precautionary approach must still be applied to these structures.

Finally, while the environmental impact of CNTs and their related structures are increasingly examined, that of the different processes used in the CNT technology, including the steps of pre-treatment, synthesis, purification or post-treatment must be investigated further [155]. A recent study indicates that significant, measurable impacts were found to fossil fuels, airborne inorganics, and climate change

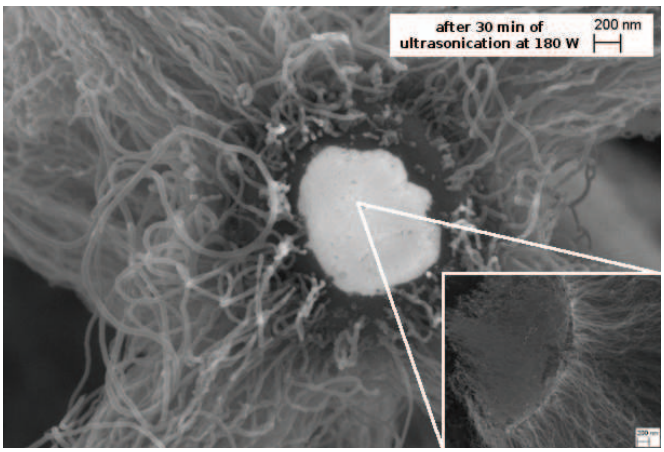

Figure 7.3.6: SEM image of CNT/μ-Al_2O_3 hybrids protected by a graphitic shell after 30 min ultrasonication at 180 W.

for the manufacture of a CNT-based electronic device [25]. Given these uncertain risks and unknown outcomes, it is prudent to assess the environmental attributes for nanomanufacturing products and processes while in the developmental phase. Results can inform the development and commercialization of safe, economically competitive, and environmentally responsible nanotechnologies.

References

[1] J.O. Aguilar, T.R. Bautista-Quirano, and F. Aviles. Influence of carbon nanotube clustering on the electrical conductivity of polymer composite films. *eXPRESS Polymer Letters*, 4:292–299, 2010.

[2] A. Aguilar-Esguezabal, W. Antunez, G. Alonso, F. Paraguay-Delgado, F. Espinosa, and M. Miki-Yoshida. Study of carbon nanotubes synthesis by spray pyrolysis and model of growth. *Diamond & Related Materials*, 15:1329–1335, 2006.

[3] P.B. Amama, C.L. Pint, L. McJilton, S.M. Kim, E.A. Stach, P. Terry Murray, R.H. Hauge, and B. Maruyama. Role of water in super growth of single-walled carbon nanotube carpets. *Nano Letters*, 9:44–49, 2009.

[4] H. Amara, C. Bichara, and F. Ducastelle. Understanding the nucleation mechanisms of ... in catalytic chemical vapor deposition. *Physical Review Letters*, 100:056105, 2008.

[5] R.T.K. Baker. Catalytic growth of carbon filaments. *Carbon*, 27: 315, 1989.

[6] M.J. Behr, E.A. Gaulding, K.A. Mkhoyan, and E.S. Aydil. Effect of hydrogen on catalyst nanoparticles in carbon nanotube growth. *Journal of Applied Physics*, 108:053301–3, 2010.

[7] M.J. Behr, E.A. Gaulding, K.A. Mkhoyan, and E.S. Aydil. Hydrogen etching and cutting of multiwall carbon nanotubes. *Journal of Vacuum Science and Technology B: Microelectronics and Nanometer Structures*, 28:1187–1194, 2010.

[8] M.J. Behr, K.A. Mkhoyan, and E.S. Aydil. Catalyst rotation, twisting, and bending during multiwall carbon nanotube growth. *Carbon*, 48:3840–3845, 2010.

[9] M.J. Behr, K.A. Mkhoyan, and E.S. Aydil. Orientation and morphological evolution of catalyst nanoparticles during carbon nanotube growth. *ACS Nano*, 4:5087–5094, 2010.

[10] S.W. Benson and R. Shaw. Kinetics and mechanism of hydrogenolyses. *Journal of Chemical Physics*, 47:4052–4055, 1967.

[11] E. Bergamaschi, O. Bussolati, A. Magrini, M. Bottoni, L. Migliore, S. Bellucci, I. Iavicoli, and A. Bergamaschi. Nanomaterials and lung toxicity: interactions with airways cells and relevance for occupational health risk assessment. *International Journal of Immunopathology and Pharmacology*, 19:3–10, 2006.

[12] D. S. Bethune, C. H. Kiang, M. S. De Vries, G. Gorman, and R. Savoy. Cobalt catalysed growth of carbon nanotubes with single-atomic-layer walls. *Nature*, 363:605–607, 1993.

[13] H. Bladh, J. Johnsson, J. Rissler, H. Abdulhamid, N.-E. Olofsson, M. Sanati, J. Pagels, and P.-E. Bengtsson. Influence of soot particle aggregation on time-resolved laser-induced incandescence signals. *Applied Physics B: Lasers and Optics*, 104:331–341, 2011.

[14] S.N. Bondi, W.J. Lackey, R.W. Johnson, X. Wang, and Z.L. Wang. Laser assisted chemical vapor deposition synthesis of carbon nanotubes and their characterization. *Carbon*, 44:1393–1403, 2006.

[15] A. Borjesson and K. Bolton. First principles studies of the effect of ostwald ripening on carbon nanotube chirality distributions. *ACS Nano*, 5:771–779, 2011.

[16] M. Bozlar, D. He, J. Bai, Y. Chalopin, N. Mingo, and S. Volz. Carbon nanotube microarchitectures for enhanced thermal conduction at ultralow mass fraction in polymer composites. *Advanced Materials*, 22:1654–1658, 2010.

[17] J. Brubach, J. Janicka, and A. Dreizler. An algorithm for the characterisation of multi-exponential decay curves. *Optics and Lasers in Engineering*, 47:75–79, 2009.

[18] D.W. Chae and B.C. Kim. Physical properties of isotactic poly(propylene)/silver nanocomposites: Dynamic crystallization behavior and resultant morphology. *Macromolecular Materials and Engineering*, 290:1149–1156, 2005.

[19] C.H. Cheung, A. Kurtz, H. Park, and C.M. Lieber. Diameter-controlled synthesis of carbon nanotubes. *Journal Physical Chemistry B*, 106(10):2429–2433, 2002.

[20] W.-H. Chiang and R.M. Sankaran. Microplasma synthesis of metal nanoparticles for gas-phase studies of catalyzed carbon nanotube growth. *Applied Physics Letters*, 91:1215031–3, 2007.

[21] W.-H. Chiang and R.M. Sankaran. Linking catalyst composition to chirality distributions of as-grown single-walled carbon nanotubes by tuning nixfe1-x nanoparticles. *Nature Materials*, 8: 882–886, 2009.

[22] W.-H. Chiang and R.M. Sankaran. Relating carbon nanotube growth parameters to the size and composition of nanocatalysts. *Diamond & Related Materials*, 18:946–952, 2009.

[23] L. Ci and J. Bai. Novel micro/nanoscale hybrid reinforcement: Multiwalled carbon nanotubes on sic particles. *Advanced Materials*, 16:2021–2024, 2004.

[24] L. Ci, B. Wei, C. Xu, J. Liang, D. Wu, S. Xie, NewAuthor7, W. Zhou, Y. Li, Z. Liu, and D. Tang. Crystallization behavior of the amorphous carbon nanotubes prepared by the cvd method. *Journal of Crystal Growth*, 233:823–828, 2001.

[25] L.J. Dahlben and J.A. Isaacs. Life cycle inventories for nanomanufactured carbon nanotube products. *IEEE*, 978:1–4, 2008.

[26] S. Dankers, S. Schraml, S. Will, and A. Leipertz. Application of laser- induced incandescence for the determination of primary particle sizes of nanoparticles demonstrated using carbon blacks. *Chemical Engineering & Technology*, 25:1160–1164, 2002.

[27] R. G. de Villoria, A. J. Hart, and B. L. Wardler. Continuous high-yield production of vertically aligned carbon nanotubes on 2d and 3d substrates. *ACS Nano*, 5(6):4850–4857, 2011.

[28] C.P. Deck and K. Vecchio. Growth mechanism of vapor phase cvd-grown multi-walled carbon nanotubes. *Carbon*, 43:2608–2617, 2005.

[29] I. Denysenko and K. Ostrikov. Ion-assisted precursor dissociation and surface diffusion: Enabling rapid, low-temperature growth of carbon nanofibers. *Applied Physics Letters*, 90:251501–3, 2007.

[30] S. Diamond and C. Wert. The diffusion of carbon in nickel above and below the curie temperature. *Transactions of the Metallurgical Society of AIME*, 239:705–710, 1967.

[31] A. Dichiara and J. Bai. The growth of carbon nanotube multilayers on ceramic -particles by catalytic chemical vapour deposition. *Diamond & Related Materials*, 29:52–58, 2012.

[32] A. Dichiara, J.-K. Yuan, S.-H. Yao, A. Sylvestre, and J. Bai. Chemical vapor deposition synthesis of carbon nanotube-graphene nanosheet hybrids and their application in polymer composites. *Journal of Nanoscience and Nanotechnology*, 8:6935–6940, 2012.

[33] F. Ding, K. Bolton, and A. Rosen. Structure and thermal properties of supported catalyst clusters for single-walled carbon nanotube growth. *Applied Surface Science*, 252:5254–5258, 2006.

[34] F. Ding, A.R. Harutyunyan, and B.I. Yakobson. Dislocation theory of chirality-controlled nanotube growth. *Proceedings of the National Academy of Sciences of the USA*, 108:2506, 2009.

[35] G.J.M. Dormans. Omcvd of transition metals and their silicides using metallocenes and (di)silane or silicon tetra-bromide. *Journal of Crystal Growth*, 108:806–816, 1991.

[36] G. Du, S. Feng, J. Zhao, C. Song, S. Bai, and Z. Zhu. Particle-wire-tube mechanism for carbon nanotube evolution. *Journal of American Chemical Society*, 128:15405–15414, 2006.

[37] C. Ducati, I. Alexandrou, M. Chhowalla, G.A.J. Amaratunga, and J. Robertson. Temperature selective growth of carbon nanotubes by chemical vapor deposition. *Journal of Applied Physics*, 92:1499746–5, 2002.

[38] Dudragne, Adam, and Amouroux. Time-resolved laser-induced breakdown spectroscopy: Application for qualitative and quantitative detection of f, cl, s, and c in air. *Applied Spectroscopy*, 52: 1321–1327, 1998.

[39] G. S. Duesberg, A. P. Graham, M. Liebau, R. Seidel, E. Unger, F. Kreupl, and W. Hoenlein. Growth of isolated carbon nanotubes with lithographically defined diameter and location. *Nano Letters*, 3(2):257–259, 2003.

[40] H. Dumortier, S. Lacotte, G. Pastorin, R. Marega, W. Wu, D. Bonifazi, J.P. Briand, M. Prato, S. Muller, and A. Bianco. Functionalized carbon nanotubes are non-cytotoxic and preserve the functionality of primary immune cells. *Nano Letters*, 6:1522–1528, 2006.

[41] A.C. Eckbreth. Effects of laser-modulated particulate incandescence on raman scattering diagnostics. *Journal of Applied Physics*, 48:4473–4479, 1977.

[42] K. Elihn and K. Larsson. A theoretical study of the thermal fragmentation of ferrocene. *Thin Solid Films*, 458:325–329, 2004.

[43] Z. Fan, J. Yan, T. Wei, L. Zhi, G. Ning, T. Li, and F. Wei. Asymmetric supercapacitors based on graphene/mno2 and activated carbon nanofiber electrodes with high power and energy density. *Advanced Functional Materials*, 21:2366, 2011.

[44] H. Feng, J. Ma, and Z. Hu. Six-membered-ring-based radical mechanism for catalytic growth of carbon nanotubes with benzene precursor. *Journal of Physical Chemistry C*, 113(37):16495–16502, 2009.

[45] Ferioli, Puzinauskas, and Buckley. Laser-induced breakdown spectroscopy for on- line engine equivalence ratio measurements 1183. *Applied Spectroscopy*, 57:1183–1189, 2003.

[46] M.-F. C. Fiawoo, A.-M. Bonnot, H. Amara, C. Bichara, J. Thibault-Penisson, and A. Loiseau. Evidence of correlation between catalyst particles and the single-wall carbon nanotube diameter: A first step towards chirality control. *Physical Review Letters*, 108(195503), 2012.

[47] A.V. Filippov, M.W. Markus, and P. Roth. In-situ characterization of ultrafine particles by laser-induced incandescence: sizing and particle structure determination. *Journal Aerosol Science*, 30(1):71–87, 1999.

[48] E. O. Fischer. On the way to carbene and carbyne complexes. *Advances in Organometallic Chemistry*, 14:1–32, 1976.

[49] L. Gao, E.T. Thostenson, Z. Zhang, and T.W. Chou. Sensing of damage mechanisms in fiber-reinforced composites under cyclic loading using carbon nanotubes. *Advanced Functional Materials*, 19:123–130, 2009.

[50] Y. Gefen, A. Aharony, and S. Alexander. Anomalous diffusion on percolation clusters. *Physical Review Letters*, 50:77, 1983.

[51] D.B. Geohegan, A.A. Puretzky, I.N. Ivanov, S. Jesse, G. Eres, and J.Y. Howe. In situ growth rate measurements and length control during chemical vapor deposition of vertically aligned multiwall carbon nanotubes. *Applied Physics Letters*, 83:1851–1853, 2003.

[52] D.A. Gomez-Gualdron and P.B. Balbuena. Growth of chiral single-walled carbon nanotube caps in the presence of a cobalt cluster. *Nanotechnology*, 20:215601, 2009.

[53] D.A. Gomez-Gualdron, G.D. McKenzie, J.F. Alvarado, and P.B. Balbuena. Dynamic evolution of supported metal nanocatalyst/carbon structure during single-walled carbon nanotube growth. *ACS Nano*, 24:720–735, 2012.

[54] T. Guo, P. Nikolaev, A.G. Rinzler, D. Tomanek, D.T. Colbert, and R. E. Smalley. Self-assembly of tubular fullerenes. *Journal Physical Chemistry*, 99:10694–10697, 1995.

[55] J.H. Hafner, M.J. Bronikowski, B.R. Azamian, P. Nikolaev, A.G. Rinzler, D.T. Colbert, K.A. Smith, and R. E. Smalley. Catalytic growth of single-wall carbon nanotubes from metal particles. *Chemical Physic Letters*, 296:195–202, 1998.

[56] S. Han, X. Liu, and C. Zhou. Template-free directional growth of single-walled carbon nanotubes. *Journal of American Chemical Society*, 127:5294–5295, 2005.

[57] K. Hasegawa and S. Noda. Diameter increase in millimeter-tall vertically aligned single-walled carbon nanotubes during growth. *Applied Physics Express*, 3:045103–1–3, 2010.

[58] K. Hasegawa and S. Noda. Millimeter-tall single-walled carbon nanotubes rapidly grown with and without water. *ACS Nano*, 5: 975–984, 2011.

[59] K. Hata, D. N. Futuba, K. Mizuno, T. Namai, M. Yumura, and S. Iijima. Water-assisted highly efficient synthesis of impurity-free single-walled carbon nanotubes. *Science*, 305:1273–1276, 2004.

[60] D. He and J. Bai. Acetylene-enhanced growth of carbon nanotubes on ceramic microparticles for multi-scale hybrid structures. *Chemical Vapor Deposition*, 17:98–106, 2011.

[61] D. He, M. Bozlar, M. Genestoux, and J. Bai. Diameter- and length-dependent self-organizations of multi-walled carbon nanotubes on spherical alumina microparticles. *Carbon*, 48:1159–1170, 2010.

[62] D. He, H. Li, and J. Bai. Experimental and numerical investigation of the position-dependent growth of carbon nanotube–alumina microparticle hybrid structures in a horizontal cvd reactor. *Carbon*, 49:5359–5372, 2011.

[63] D. He, H. Li, W Li, P. Haghi-Ashtiani, P. Lejay, and J. Bai. Growth of carbon nanotubes in six orthogonal directions on spherical alumina microparticles. *Carbon*, 49:2273–2286, 2011.

[64] S. Helveg, C. Lopez-Cartes, J. Sehested, P.L. Hansen, B.S. Clausen, J.R. Rostrup-Nielsen, F. Abild-Pedersen, and J.K.

Norskov. Atomic-scale imaging of carbon nanofibre growth. *Nature*, 427:426–429, 2004.

[65] S. Hofmann, R. Sharma, G. Du, C. Mattevi, C. Cepek, M. Cantoro, C. Ducati, S. Pisana, A. Parvez, A.C. Ferrari, D. Borkowski, E. Rafael, S. Lizzi, L. Petaccia, A. Goldini, and J. Robertson. In-situ observations of catalyst dynamics during surface-bound carbon nanotube nucleation. *Nano Letters*, 7:602–608, 2007.

[66] W.K. Hsu, M. Terrones, J.P. Hare, H. Terrones, H. W. Kroto, and D.R.M. Walton. Electrolytic formation of carbon nanostructures. *Chemical Physic Letters*, 262:161–166, 1996.

[67] J. Hu, Z. Wang, W. Zhang, Z. Xu, Y. Hu, Z. Zhu, and X. Duan. Nanowires with a carbon nanotube core and silicon oxide sheath. *Carbon*, 44:1581–1583, 2006.

[68] S. Iijima. Helical microtubules of graphite carbon. *Nature*, 354: 56–58, 1991.

[69] S. Iijima and T. Ichihashi. Single-shell carbon nanotubes of 1-nm diameter. *Nature*, 363:603–605, 1993.

[70] K. Imasaka, Y. Kanatake, Y. Ohshiro, J. Suehiro, and M. Hara. Production of carbon nanoonions and nanotubes using an intermittent arc discharge in water. *Thin Solid Films*, 506:250–254, 2006.

[71] M. I. Ionescu, Y. Zhang, R. Li, X. Sun, H. Abou-Rachid, and L.-S. Lussier. Hydrogen-free spray pyrolysis chemical vapor deposition method for the carbon nanotube growth: Parametric studies. *Applied Surface Science*, 257(15):6843–6849, 2011.

[72] S. Irle, Y. Ohta, Y. Okamoto, A.J. Page, Y. Wang, and K. Morokuma. Milestone molecular dynamics simulations of single-walled carbon nanotube formation: A brief critical review. *Nano Research*, 2:755–767, 2009.

[73] J.-H. Jeong, A. Yamazaki, S. Suzuki, Y. Koboyashi, and Y. Homma. Behavior of catalytic nanoparticles during chemical vapor deposition for carbon nanotube growth. *Chemical Physic Letters*, 422:83–88, 2006.

[74] J.-H. Jeong, S. Suzuki, Y. Koboyashi, A. Yamazaki, H. Yoshimura, and Y. Homma. Size control of catalytic nanoparticles by thermal treatment and its application to diameter control of single-walled carbon nanotubes. *Applied Physics Letters*, 90(043108):3, 2007.

[75] C. Jin, K. Suenaga, and S. Iijima. How does a carbon nanotube grow? an in situ investigation on the cap evolution. *ACS Nano*, 2:1275–1279, 2008.

[76] Y. Kajikawa, T. Tsuchiya, S. Noda, and H. Komiyama. Incubation time during the cvd of si onto sio2 from silane. *Chemical Vapor Deposition*, 10:128–133, 2004.

[77] M. Kerker. *The Scattering of Light and Other Electromagnetic Radiation*. Academic Press, New York, USA, 1996.

[78] V.O. Khavrus, E.M.M. Ibrahim, A. Leonhardt, S. Hample, S. Oswald, C. Taschner, and B. Buchner. Conditions of simultaneous growth and separation of single- and multiwalled carbon nanotubes. *Journal of Physical Chemistry C*, 114:843–848, 2010.

[79] D.Y. Kim, H. Sugime, K. Hasegawa, T. Osawa, and S. Noda. Sub-millimeter-long carbon nanotubes repeatedly grown on and separated from ceramic beads in a single fluidized bed reactor. *Carbon*, 49(6):1972–1979, 2011.

[80] H. Kim and W. Sigmund. Iron particles in carbon nanotubes. *Carbon*, 43:1743–1748, 2005.

[81] K.J. Kim, W.R. Yu, J.S. Lee, L. Gao, E.T. Thostenson, and T.W. Chou. Damage characterization of 3d braided composites using carbon nanotube-based in situ sensing. *Composite Part A: Applied Science and Manufacturing*, 41:1531–1537, 2010.

[82] S.H. Kim and M.R. Zachariah. In-flight size classification of carbon nanotubes by gas phase electrophoresis. *Nanotechnology*, 16: 2149–2155, 2005.

[83] Boris F. Kock, Can Kayan, Jorg Knipping, Hans R. Orthner, and Paul Roth. Comparison of lii and tem sizing during synthesis of

iron particle chains. *Proceedings of the Combustion Institute*, 30: 1689–1697, 2005.

[84] H. W. Kroto, J. R. Heath, S. C. O'Brien, R. F. Curl, and R. E. Smalley. C60: Buckminsterfullerene. *Nature*, 318:162–163, 1985.

[85] M. Kumar and Y. Ando. Chemical vapor deposition of carbon nanotubes: A review on growth mechanism and mass production. *Journal of Nanoscience and Nanotechnology*, 10(6):3739–3758, 2010.

[86] D.-H. Kuo and M.-Y. Su. The effects of hydrogen and temperature on the growth and microstructure of carbon nanotubes obtained by the fe(co)5 gas-phase-catalytic chemical vapor deposition. *Surface Coating Technology*, 201:9172–9178, 2007.

[87] K. Kuwana and K. Saito. Modeling cvd synthesis of carbon nanotubes: Nanoparticle formation from ferrocene. *Carbon*, 43:2088–2095, 2005.

[88] K. Kuwana and K. Saito. Modeling ferrocene reactions and iron nanoparticle formation: Application to cvd synthesis of carbon nanotubes. *Proceedings of the Combustion Institute*, 31:2965–2972, 2007.

[89] P. Landois, S. Rouziere, M. Pinault, D. Porterat, C. Mocuta, E. Elkaim, M. Mayne L'Hermite, and P. Launois. Growth of aligned multi-walled carbon nanotubes: First in situ and time-resolved x-ray diffraction analysis. *Physical Status Solidi B*, 248: 2449–2453, 2011.

[90] D. Laplaze, L. Alvarez, T. Guillard, J.M. Badie, and G. Flamant. Carbon nanotubes: dynamics of synthesis processes. *Carbon*, 40: 1621–1634, 2002.

[91] G.-D. Lee, S. Han, J. Yu, and J. Ihm. Catalytic decomposition of acetylene on fe(001): A first-principles study. *Physical Review B*, 66:081403, 2002.

[92] S.J. Lee, H.K. Baik, J. Yoo, and J.H. Han. Large scale synthesis of carbon nanotubes by plasma rotating arc discharge technique. *Diamond & Related Materials*, 11:914–917, 2002.

[93] Y.H. Lee, S.G. Kim, and D. Tomanek. Catalytic growth of single-wall carbon nanotubes: an ab initio study. *Physical Review Letters*, 78:2393–2396, 1997.

[94] K. Levenberg. A method for the solution of certain nonlinear problems in least squares. *Quart. Appl. Math.*, 2:164–168, 1944.

[95] C. Li, E.T. Thostenson, and T.W. Chou. Sensors and actuators based on carbon nanotubes and their composites: a review. *Composite Science Technology*, 68:1227–1249, 2008.

[96] W. Li, J.-K. Yuan, A. Dichiara, Y. Lin, and J. Bai. The use of vertically aligned carbon nanotubes grown on sic for in situ sensing of elastic and plastic deformation in electrically percolative epoxy composites. *Carbon*, 50:4298–4301, 2012.

[97] X. Li, W. Cai, L. Colombo, and R.S. Ruoff. Evolution of graphene growth on ni and cu by carbon isotope labeling. *Nano Letters*, 9: 4268–4272, 2009.

[98] Y.S. Lim, H.S. Kim, M.S. Kim, N.H. Cho, and S. Nahm. Chemical and micro-structural changes in glass-like carbon during high temperature heat treatment. *Macromolecular Research*, 11:122–127, 2003.

[99] M. Lin, J. Tan, C. Boothroyd, K.P. Loh, E.S. Tok, and Y.L. Foo. Direct observation of single-walled carbon nanotube growth at the atomistic scale. *Nano Letters*, 6:449–452, 2006.

[100] H. Liu, D. Takagi, Y. Ohno, S. Chiashi, T. Chokan, and Y. Homma. Growth of single-walled carbon nanotubes from ceramic particles by alcohol chemical vapor deposition. *Applied Physics Express*, 1:014001–3, 2008.

[101] K. Liu, K. Jiang, C. Feng, Z. Chen, and S. Fan. A growth mark method for studying growth mechanism of carbon nanotube arrays. *Carbon*, 43:2850–2856, 2005.

[102] Q. Liu, Z. G. Chen, B. Liu, W. Ren, F. Li, H. Cong, and H. M. Cheng. Synthesis of different magnetic carbon nanostructures by the pyrolysis of ferrocene at different sublimation temperatures. *Carbon*, 46(14):1892–1902, 2008.

[103] Q. Liu, W. Ren, Z. G. Chen, D. W. Wang, B. Liu, B. Yu, F. Li, H. Cong, and H. M. Cheng. Diameter-selective growth of single-walled carbon nanotubes with high quality by floating catalyst method. *ACS Nano*, 2(8):1722–1728, 2008.

[104] O.A. Louchev, Y. Sato, and H. Kanda. Growth mechanism of carbon nanotube forests by chemical vapor deposition. *Applied Physics Letters*, 80:2752–2754, 2002.

[105] A. Magrez, S. Kasas, V. Salicio, N. Pasquier, J.W. Seo, M. Celio, S. Catsicas, B. Schwaller, and L. Forro. Cellular toxicity of carbon-based nanomaterials. *Nano Letters*, 6:1121–1125, 2006.

[106] M. Marchand, C. Journet, D. Guillot, J.-M. Benoit, B.I. Yakobson, and S.T. Purcell. Growing a carbon nanotube atom by atom: And yet it does turn. *Nano Letters*, 9:2961–2966, 2009.

[107] M. Maret, K. Hostache, M.C. Schouler, B. Marcus, F. Rousset-Dherbey, NewAuthor6, M. Albrecht, and P. Gadelle. Oriented growth of single-walled carbon nanotubes on a mgo(0 0 1) surface. *Carbon*, 45:180–187, 2007.

[108] D. W. Marquardt. An algorithm for least squares estimation of nonlinear parameters. *SIAM J. Appl. Math.*, 11:431–441, 1963.

[109] Martin, Wullshleger, Garten, and Palombo. Laser-induced breakdown spectroscopy for the environmental determination of total carbon and nitrogen in soils. *Applied Optics*, 42:2072–2077, 2003.

[110] C. Mattevi, C. T. Wirth, S. Hofmann, R. Blume, M. Cantoro, C. Ducati, C. Cepek, A. Knop-Gericke, S. Milne, C. Castellarin-Cudia, S. Dolafi, A. Goldoni, R. Schloegl, and J. Robertson. In-situ x-ray photoelectron spectroscopy study of catalystsupport interactions and growth of carbon nanotube forests. *Journal of Physical Chemistry C*, 112(32):12207–12213, 2008.

[111] L.A. Melton. Soot diagnostics based on laser-heating. *Applied Optics*, 23:2201–2208, 1984.

[112] W. Merchan-Merchan, A.V. Saveiliev, L. Kennedy, and W.C. Jimenez. Combustion synthesis of carbon nanotubes and related

nanostructures. *Progress in Energy and Combustion Science*, 36: 696–727, 2010.

[113] E. R. Meshot, D. L. Plata, S. Tawfick, Y. Zhang, E. A. Verploegen, and A. J. Hart. Engineering vertically aligned carbon nanotube growth by decoupled thermal treatment of precursor and catalyst. *ACS Nano*, 3(9):2477–2486, 2009.

[114] H. Michelsen, P. O. Witze, D. Kayes, and S. Hochgreb. Time-resolved laser-induced incandescence of soot: The influence of experimental factors and microphysical mechanisms. *Applied Optics*, 42:5577–5590, 2003.

[115] H. Michelsen, F. Liu, B. F. Kock, H. Bladh, A. Boiarciuc, M. Charwath, T. Dreier, R. Hadef, M. Hofmann, J. Reimann, S. Will, P.-E. Bengtsson, H. Bockhorn, F. Foucher, K. P. Geigle, C. Mounam-Rousselle, C. Schulz, R. Stirn, B. Tribalet, and R. Suntz. Modeling laser-induced incandescence of soot: A summary and comparison of lii models. *Applied Physics B: Lasers and Optics*, 87:503–521, 2007.

[116] H. Michelsen, M. A. Linne, B. F. Kock, M. Hofmann, B. Tribalet, and C. Schulz. Modeling laser-induced incandescence of soot: Enthalpy changes during sublimation, conduction, and oxidation. *Applied Physics B: Lasers and Optics*, 93:645–656, 2008.

[117] A. Moisala, A. G. Nasibulin, and E. I. Kaupinnen. The role of metal nanoparticles in the catalytic production of single-walled carbon nanotubesa review. *J. Phys. Condens. Matter.*, 15:S3011, 2003.

[118] J.F. Mojica and L.L. Levenson. Bulk-to-surface precipitation and surface diffusion of carbon on polycrystalline nickel. *Surface Science*, 59:447–460, 1976.

[119] M. Monthioux and V. L. Kuznetsov. Who should be given the credit for the discovery of carbon nanotubes? *Carbon*, 44:1621–1625, 2006.

[120] M. Moors, H. Amara, T. Visart De Bocarme, C. Bichara, F. Ducastelle, N. Kruse, and J.-C. Charlier. Early stages in the

nucleation process of carbon nanotubes. *ACS Nano*, 3:511–516, 2009.

[121] L.E. Murr and K.F. Soto. A tem study of soot, carbon nanotubes, and related fullerene nanopolyhedra in common fuel-gas combustion sources. *Materials Characterization*, 55:50–65, 2005.

[122] K. Nakaso, B. Han, K.H. Ahn, M. Choi, and K. Okuyama. Synthesis of non-agglomerated nanoparticles by an electrospray assisted chemical vapor deposition (es-cvd) method. *Journal of Aerosol Science*, 34:869–881, 2003.

[123] R. Negishi, H. Hirano, Y. Ohno, K. Maehashi, K. Matsumoto, and Y. Koboyashi. Layer-by-layer growth of graphene layers on graphene substrates by chemical vapor deposition. *Thin Solid Films*, 519:6447–6452, 2011.

[124] G. D. Nessim, A. J. Hart, J. S. Kim, D. Acquaviva, J. Oh, C. D. Morgan, M. Seita, J. S. Leib, and C. V. Thompson. Tuning of vertically-aligned carbon nanotube diameter and areal density through catalyst pre-treatment. *Nano Letters*, 8(11):3587–3593, 2008.

[125] P.E. Nolan, M.J. Schabel, and D.C. Lynch. Hydrogen control of carbon deposit morphology. *Carbon*, 33:79–85, 1995.

[126] K. Norinaga and O. Deutschmann. Detailed kinetic modelling of gas phase reactions in the chemical vapor deposition of carbon from light hydrocarbons. *Industrial and Engineering Chemistry Research*, 46:3547–3557, 2007.

[127] A. Oberlin, M. Endo, and T. Koyama. Filamentous growth of carbon through benzene decomposition. *Journal of Crystal Growth*, 32:335–349, 1976.

[128] Y. Ohta, Y. Okamoto, S. Irle, and K. Morokuma. Density-functional tight-binding molecular dynamics simulations of swcnt growth by surface carbon diffusion on an iron cluster. *Carbon*, 47:1270–1275, 2009.

[129] K. Okuyama and I.W. Lenggoro. Preparation of nanoparticles via spray route. *Chemical Engineering Science*, 58:537–547, 2003.

[130] A.J. Page, Y. Ohta, Y. Okamoto, S. Irle, and K. Morokuma. Mechanisms of single-walled carbon nanotube nucleation, growth and healing determined using qm/md methods. *Accounts of Chemical Research*, 43:1375–1385, 2010.

[131] H.B. Palmer and F.L. Dormish. The kinetics of decomposition of acetylene in the 1500 k region. *Journal Physical Chemistry*, 68: 1553–1560, 1964.

[132] M. Park, H. Kim, and J.P. Youngblood. Strain-dependent electric resistance of multi-walled carbon nanotubes/polymer composite films. *Nanotechnology*, 19:055705, 2008.

[133] K. Pastorkova, K. Jesenak, M. Kadlecikova, J. Breza, M. Kolmacka, M. Caplovicova, F. Lazistan, and M. Michalka. The growth of multi-walled carbon nanotubes on natural clay minerals. *Applied Surface Science*, 258:2661–2666, 2012.

[134] M. Pinault, V. Pichot, H. Khodja, P. Launois, C. Reynaud, and M. Mayne L'Hermite. Evidence for sequential lift in growth of aligned multiwalled carbon nanotubes multilayers. *Nano Letters*, 5:2394–2398, 2005.

[135] S. Pisana, A. Jungen, C. Zhang, A.M. Blackburn, R. Sharma, F. Cervantes-Sodi, C. Stampfer, C. Ducati, A.C. Ferrari, C. Hierold, J. Robertson, and S. Hofmann. Flying and crawling modes during surface-bound single wall carbon nanotube growth. *Journal of Physical Chemistry C*, 111:17249–17253, 2007.

[136] C.A. Poland, R. Duffin, I.A. Kinloch, A. Maynard, W.A.H. Wallace, A. Seaton, V. Stone, S. Brown, W. MacNee, and K. Donaldson. Carbon nanotubes introduced into the abdominal cavity of mice show asbestos-like pathogenicity in a pilot study. *Nature Nanotechnology*, 3:423–428, 2008.

[137] A.E. Porter, M. Gass, K. Muller, J.N. Skepper, P.A. Midgley, and M. Welland. Direct imaging of single-walled carbon nanotubes in human cells. *Nature Nanotechnology*, 2:713–717, 2007.

[138] L. V. Radushkevich and V. M. Lukyanovich. O strukture ugleroda, obrazujucegosja pri termiceskom razlozenii okisi ugleroda na zeleznom kontakte. *Zurn Fisic Chim*, 26:88–95, 1952.

[139] G.E. Ramirez-Caballero, J.C. Burgos, and P.B. Balbuena. Growth of carbon structures on stepped (211) cobalt surfaces. *Journal of Physical Chemistry C*, 113:15658–15666, 2009.

[140] R. Rao, D. Liptak, T. Cherukuri, B.I. Yakobson, and B. Maruyama. In situ evidence for chirality-dependent growth rates of individual carbon nanotubes. *Nature Materials*, 29:213–216, 2012.

[141] S. Reich, L. Li, and J. Robertson. Control the chirality of carbon nanotubes by epitaxial growth. *Chemical Physic Letters*, 421: 469–472, 2006.

[142] J.A. Rodriguez-Manzo, M. Terrones, H. Terrones, H. W. Kroto, L. Sun, and F. Banhart. In situ nucleation of carbon nanotubes by the injection of carbon atoms into metal particles. *Nature Nanotechnology*, 2:307–311, 2007.

[143] J.A. Rodriguez-Manzo, I. Janowska, C. Pham-Huu, A. Tolvanen, A.V. Krasheninnikov, K. Nordlund, and F. Banhart. Growth of single-walled carbon nanotubes from sharp metal tips. *Small*, 5: 2710–2715, 2009.

[144] R. Ryser, T. Gerber, and T. Dreier. Soot particle sizing during high-pressure diesel spray combustion via time-resolved laser-induced incandescence. *Combustion and Flame*, 156(1):120–129, 2009.

[145] S. Sakurai, H. Nishino, D. N. Futuba, S. Yasuda, T. Yamada, A. Maigne, Y. Matsuo, E. Nakamura, M. Yumura, and K. Hata. Role of subsurface diffusion and ostwald ripening in catalyst formation for single-walled carbon nanotube forest growth. *Journal of the American Chemical Society*, 134(4):2148–2153, 2012.

[146] R.J. Santoro, H.G. Semerjian, and R.A. Dobbins. Soot particle measurements in diffusion flames. *Combustion and Flame*, 51: 203–218, 1983.

[147] C. Schulz, B. F. Kock, M. Hofmann, H. Michelsen, S. Will, B. Bougie, R. Suntz, and G. Smallwood. Laser-induced incandescence: Recent trends and current questions. *Applied Physics B: Lasers and Optics*, 83(3):333–354, 2006.

[148] R. Seidel, G. S. Duesberg, E. Unger, A. P. Graham, M. Liebau, and F. Kreupl. Chemical vapor deposition growth of single-walled carbon nanotubes at 600 c and a simple growth model. *Journal Physical Chemistry B*, 108:1888–1893, 2004.

[149] S.P. Sharma and S.C. Lakkad. Morphology study of carbon nanospecies grown on carbon fibers by thermal cvd technique. *Surface Coating Technology*, 203:1329–1335, 2009.

[150] Z. Shi, Y. Lian, F. Liao, X. Zhou, Z. Gu, Y. Zhang, and S. Iijima. Purification of single-wall carbon nanotubes. *Solid State Communications*, 112:35–37, 1999.

[151] Y. Shibuta and S. Maruyama. Molecular dynamics simulation of formation process of single-walled carbon nanotubes by ccvd method. *Chemical Physic Letters*, 382:381–386, 2003.

[152] C.G. Silcocks. The kinetics of the thermal polymerization of acetylene. *Proceedings of the Royal Society A*, 242:411–429, 1957.

[153] C Singh, M.S.P. Shaffer, K.K.K. Koziol, I.A. Kinloch, and A.H. Windle. Towards the production of large-scale aligned carbon nanotubes. *Chemical Physic Letters*, 372:860–865, 2003.

[154] R.P. Smith. The diffusivity of carbon in gamma iron-cobalt alloys. *Transactions of the Metallurgical Society of AIME*, 230:476–481, 1964.

[155] C. Som, M. Berges, Q. Chaudhry, M. Dusinska, T.F. Fernandes, S.I. Olsen, and B. Nowack. The importance of life cycle concepts for the development of safe nanoproducts. *Toxicology*, 269:160–169, 2010.

[156] L.I. Stiel and G. Thodos. Thermal conductivity of nonpolar substances in dense gaseous and liquid regions. *Aiche Journal*, 10: 26–30, 1964.

[157] Sturm, Peter, and Noll. Steel analysis with laser-induced breakdowns spectrometry in the vacuum ultraviolet. *Applied Spectroscopy*, 54:1275–1278, 2000.

[158] M. Su, Y. Li, B. Maynor, A. Buldum, J.P. Lu, and J. Liu. Lattice-oriented growth of single-walled carbon nanotubes. *Journal Physical Chemistry B*, 104:6505–6508, 2000.

[159] K. Suenaga, H. Wakabayashi, M. Koshino, Y. Sato, K. Urita, and S. Iijima. Imaging active topological defects in carbon nanotubes. *Nature Nanotechnology*, 2:358–360, 2007.

[160] Y.C. Sui, B.Z. Cui, R. Guardian, D.R. Acosta, L. Martinez, and R. Perez. Growth of carbon nanotubes and nanofibres in porous anodic alumina film. *Carbon*, 40:1011–1016, 2002.

[161] G. Taguchi, Y. Yokoyama, and Y. Wu. *Taguchi Methods/Design of Experiments*. American Supplier Institute (ASI) Press, Tokyo, Japan, 1993.

[162] D. Takagi, H. Hibino, S. Suzuki, Y. Koboyashi, and Y. Homma. Carbon nanotube growth from semiconductor nanoparticles. *Nano Letters*, 7:2272–2275, 2007.

[163] E.T. Thostenson and T.W. Chou. Real-time in situ sensing of damage evolution in advanced fiber composites using carbon nanotube networks. *Nanotechnology*, 19:215713, 2008.

[164] S.C. Tjong and S.C. Bao. Preparation and nonisothermal crystallization behavior of polyamide 6/montmorillonite nanocomposites. *Journal of Polymer Science Part B*, 42:2878–2891, 2004.

[165] A.M. Valiente, P.N. Lopez, I.R. Ramos, A.G. Ruiz, C. Li, and Q. Xin. In situ study of carbon nanotube formation by c2h2 decomposition on an iron-based catalyst. *Carbon*, 38:2003–2006, 2000.

[166] R. L. Vander Wal, T. M. Ticich, and A. Brock Stephens. Can soot primary particle size be determined using laser-induced incandescence? *Combustion and Flame*, 116:291–296, 1999.

[167] R.L. Vander Wall and L.J. Hall. Flame synthesis of fe catalyzed single-walled carbon nanotubes and ni catalyzed nanobers: growth mechanisms and consequences. *Chemical Physic Letters*, 349:178–184, 2001.

[168] R.L. Vander Wall and T. M. Ticich. Comparative ¯ame and furnace synthesis of single-walled carbon nanotubes. *Chemical Physic Letters*, 336:24–32, 2001.

[169] R.L. Vander Wall and K.J. Weiland. Laser-induced incandescence - development and characterization towards a measurement of soot-volume fraction. *Applied Physics B: Lasers and Optics*, 59: 445–452, 1994.

[170] R.L. Vander Wall, M.B Gordon, M.T. Thomas, and D.P. Premal. Application of laser-induced incandescence to the detection of carbon nanotubes and carbon nanofibers. *Applied Optics*, 41: 5678–5690, 2002.

[171] Y. Wang, Z. Luo, B. Li, P. S. Ho, Z. Yao, L. Shi, E. N. Bryan, and R. J. Nemanich. Comparison study of catalyst nanoparticle formation and carbon nanotube growth: Support effect. *Journal of Applied Physics*, 101(12):1243101–8, 2007.

[172] R.W. Weeks and W.W. Duley. Aerosol-particle sizes from light emission during excitation by tea co. *Journal of Applied Physics*, 45:4661–4662, 1974.

[173] C.T. Wirth, S. Hofmann, and J. Robertson. State of the catalyst during carbon nanotube growth. *Diamond & Related Materials*, 18:940–945, 2009.

[174] R. Xiang, G. Luo, W. Qian, Q. Zhang, Y. Wang, F. Wei, Q. Li, and A. Cao. Encapsulation, compensation, and substitution of catalyst particles during continuous growth of carbon nanotubes. *Advanced Materials*, 19:2360–2363, 2007.

[175] R. Xiang, Z. Yang, Q. Zhang, G. Luo, W. Qian, F. Wei, M. Kadowaki, E. Einarsson, and S. Maruyama. Growth deceleration of vertically aligned carbon nanotube arrays: Catalyst deactivation or feedstock diffusion controlled? *Journal of Physical Chemistry C*, 112:4892–4896, 2008.

[176] R. Xiang, G. Luo, Z. Yang, Q. Zhang, W. Qian, and F. Wei. Large area growth of aligned cnt arrays on spheres: Cost performance and product control. *Materials Letters*, 63:84–87, 2009.

[177] X. Xu, S. Huang, Y. Hu, J. Lu, and Z. Yang. Continuous synthesis of carbon nanotubes using a metal-free catalyst by cvd. *Materials Chemistry & Physics*, 133:95–102, 2012.

[178] Y. Xu, G. Ray, and B. Abdel-Magid. Thermal behavior of single-walled carbon nanotube polymer–matrix composites. *Composite Part A: Applied Science and Manufacturing*, 37:114–121, 2006.

[179] T. Yamada, A. Maigne, M. Yudasaka, K. Mizuno, D. N. Futuba, M. Yumura, S. Iijima, and K. Hata. Revealing the secret of water-assisted carbon nanotube synthesis by microscopic observation of the interaction of water on the catalysts. *Nano Letters*, 8(12): 4288–4292, 2008.

[180] K.L. Yang and R.T. Yang. The accelerating and retarding effects of hydrogen on carbon deposition on metal surfaces. *Carbon*, 24: 687–693, 1986.

[181] Y. Yao, C. Feng, J. Zhang, and Z. Liu. Cloning of single-walled carbon nanotubes via open-end growth mechanism. *Nano Letters*, 9:1673–1677, 2009.

[182] O.V. Yazyev and A. Pasquarello. Effect of metal elements in catalytic growth of carbon nanotubes. *Physical Review Letters*, 100:156102–6, 2008.

[183] J.-K. Yuan, W. Li, S.-H. Yao, Y.-Q. Lin, A. Sylvestre, and J. Bai. High dielectric permittivity and low percolation threshold in polymer composites based on sic-carbon nanotubes micro/nano hybrid. *Applied Physics Letters*, 98:032901.1–3, 2011.

[184] J.-K. Yuan, S.-H. Yao, A. Sylvestre, and J. Bai. Biphasic polymer blends containing carbon nanotubes: Heterogeneous nanotube distribution and its influence on the dielectric properties. *Journal of Physical Chemistry C*, 116(2):2051, 2012.

[185] E.A. Zaragoza-Contreras, C.A. Hernandez-Escobar, A. Navarrete-Fontes, and S.G. Flores-Gallardo. Synthesis of carbonblack/polystyrene conductive nanocomposite. pickering emulsion effect characterized by tem. *Micron*, 42:263–270, 2011.

[186] X. Zhang, A. Cao, B. Wei, Y. Li, J. Wei, C. Xu, and D. Wu. Rapid growth of well-aligned carbon nanotube arrays. *Chemical Physic Letters*, 362:285–290, 2002.

[187] N. Zhao, C. He, Z. Jiang, J. Li, and Y. Li. Fabrication and growth mechanism of carbon nanotubes by catalytic chemical vapor deposition. *Materials Letters*, 60(2):159–163, 2006.

[188] H.-W. Zhu, K. Suenaga, A. Hashimoto, K. Urita, K. Hata, and S. Iijima. Atomic-resolution imaging of the nucleation points of single-walled carbon nanotubes. *Small*, 1:1180–1183, 2005.

[189] H.-W. Zhu, K. Suenaga, J. Wei, K. Wang, and D. Wu. A strategy to control the chirality of single-walled carbon nanotubes. *Journal of Crystal Growth*, 310:5473–5476, 2008.

[190] T. Zoberdier, T.W. Chamberlain, J. Biskupek, N. Kuganathan, S. Eyhusen, E. Bichoutskaia, U. Kaiser, and A.N. Khlobystov. Interactions and reactions of transition metal clusters with the interior of single-walled carbon nanotubes imaged at the atomic scale. *Journal of American Chemical Society*, 15:3073–3079, 2012.

The data of the present thesis have been partially published or are in preparation:

Peer-reviewed journals

- Wei-Kang Li, **Anthony Dichiara**, Jin-Kai Yuan, You-Qin Lin, Jinbo Bai. The use of vertically aligned carbon nanotubes grown on SiC for *in situ* sensing of elastic and plastic deformation in electrically percolative epoxy composites. *Carbon*, 50:4298-4301, 2012.

- **Anthony Dichiara**, Jin-Kai Yuan, Sheng-Hong Yao, Alain Sylvestre, Jinbo Bai. CVD synthesis of carbon nanotube graphene nanosheet hybrids and their application in polymer composites. *Journal of Nanoscience & Nanotechnology*, 12:6935-6940, 2012.

- **Anthony Dichiara**, Jinbo Bai. The growth of carbon nanotube multilayers on ceramic µ-particles by catalytic chemical vapour deposition. *Diamond & Related Materials*, 29:52-58, 2012.

- **Anthony Dichiara**, Youqin Lin, Delong He, Paul Haghi-Ashtiani, Jinbo Bai. Uniform diameter multi-walled carbon nanotubes with a controlled wall number obtained by a simple chemical vapor deposition method. *Chemical Physics Letters* (2012). Accepted.

- Wei-Kang Li, **Anthony Dichiara**, Jinbo Bai. Carbon nanotube-graphene nanoplatelet hybrids as high-performance multifunctional reinforcements in epoxy composites. *Composites Science & Technology* (2012). Accepted.

- **Anthony Dichiara**, Jin-Kai Yuan, Laurent Zimmer, Jinbo Bai. Evidence of a synergistic effect by mixing Al_2O_3 and SiC

micro-particles on the growth of carbon nanotube by chemical vapor deposition. *Nanoscale* (2012). Under review.

- **Anthony Dichiara**, Laurent Zimmer, Jinbo Bai. In situ monitoring of the suspended nanoparticle size by time-resolved laser-induced incandescence during floating CVD: influence on the CNT growth. *Journal of Nanoparticle Research* (2012). Under review.

Book chapter

- **Anthony Dichiara**, Jing Shen, Jinbo Bai. Growth mechanism of carbon nanotubes by CVD: a review of catalysts' features and roles. *in preparation.*

- **Anthony Dichiara**, Delong He, Jinbo Bai. Thermal decomposition of xylene: experimental and computational study. Xylenes: Synthesis, Characterization and Physicochemical Properties. NOVA (2012). Under process.

Patents

- Jinbo Bai, **Anthony Dichiara**, Jin-Kai Yuan. Carbon nanotube growth process on a mixture of particles or fibers containing at least one O atom with particles or fibers of a material which contains at least one Si atom. Ref. 212198FR00 (2011).

- Jinbo Bai, Youqin Lin, **Anthony Dichiara**. Improvements of the adhesion between carbon nanotubes and their support by the deposition of a carbon nanolayer. Ref. 212199FR00 (2012).

- Jinbo Bai, **Anthony Dichiara**, Youqin Lin. Monitoring of the CNT layer number by the deposition of graphene. Ref. 212199-1FR00 (2012).

- Jinbo Bai, Youssef Magga, Jing Zhang, **Anthony Dichiara**, Delong He. Improvements of the interface between the reinforcements and the matrix in a composite material. Ref. 214428FR00 (2012).

Awards

- Second prize winner of the 2012 Royal Microscopical Society Biennal International Micrograph Competition in Physical Sciences.